



**NTNU – Trondheim**  
Norwegian University of  
Science and Technology

# Numerical modelling of marine icing on offshore structures and vessels

**Eirik Schrøder Hansen**

Master of Science in Physics and Mathematics

Submission date: June 2012

Supervisor: Ingve Simonsen, IFY

Co-supervisor: Sigurd Henrik Teigen, Statoil

Norwegian University of Science and Technology  
Department of Physics



## **Abstract**

A numerical model for predicting icing on offshore structures and vessels has been developed and implemented. The model calculates the icing caused by freezing sea spray, and focuses on two distinct sources of spray - spray from droplets blowing off whitecaps on the sea surface, and spray from waves colliding with the vessel. The implementations of both wind-induced and wave-induced sea spray are based on existing theoretical models, and are combined with a thermodynamic model for the icing process. The model may be used to calculate icing on reference objects or structures on the vessel. In addition, algorithms have been developed so that the model can be applied to polygon-based vessel geometries, calculating the icing distribution over the entire vessel. The model has been applied to meteorological observations and hindcast data for locations in the Norwegian Sea and Barents Sea, in particular at the locations of the Norne field and the undeveloped Skrugard and Shtokman fields. The results indicate that the icing will be comparable at the locations of Skrugard and Shtokman, and that both the frequency and severity of icing events will be far greater for these two locations than for Norne. Although conditions at Shtokman are colder than at Skrugard, the higher winds and waves near Skrugard will increase the available sea spray in the model, thus making the number of severe icing events more similar for the two locations.



## Sammendrag

En numerisk modell for å forutse ising på offshore-installasjoner og fartøy har blitt utviklet og implementert. Modellen regner ut isingen forårsaket av sjøsprøyt som fryser, og fokuserer på to bestemte kilder for sprøyt - sprøyt fra dråper som blåser av skumskavler på havoverflaten, og sprøyt fra bølger som kolliderer med fartøyet. Implementeringene av både vindindusert og bølgeindusert sjøsprøyt er basert på eksisterende teoretiske modeller, og er kombinert med en termodynamisk modell for isingsprosessen. Modellen kan benyttes til å beregne isingen på referanseobjekter og -strukturer på fartøyet. I tillegg har det blitt utviklet algoritmer for å benytte modellen på polygon-baserte fartøysgeometrier, slik at isingsfordelingen på hele fartøyet kan regnes ut. Modellen har blitt benyttet på meteorologiske observasjoner og hindcast-data for lokasjoner i Norskehavet og i Barentshavet, særlig på lokasjonene til Norne-feltet og de uutviklede feltene ved Skrugard og Shtokman. Resultatene indikerer at isingen ved Skrugard og Shtokman vil være sammenlignbar, og at både frekvens og styrke av isingshendelser vil være langt større ved disse to stedene enn ved Norne. Selv om forholdene ved Shtokman er kaldere enn ved Skrugard, så vil de høyere vindhastighetene og bølgene ved Skrugard øke den tilgjengelige sjøsprøyten i modellen, og dermed gjøre antallet alvorlige isingshendelser mer likt for de to lokasjonene.



# Contents

<b>1</b>	<b>Introduction</b>	<b>1</b>
<b>2</b>	<b>Data and theory</b>	<b>3</b>
2.1	Practical information . . . . .	3
2.2	Sources of meteorological data . . . . .	3
2.3	Wind-induced spray . . . . .	6
2.3.1	Sea spray concentration at the sea surface . . . . .	6
2.3.2	Height dependency of the spray concentration . . . . .	7
2.3.3	Simple icing calculations . . . . .	7
2.3.4	Calculating friction velocity and wind profile . . . . .	8
2.4	Spray due to wave collisions . . . . .	12
2.5	Icing calculations . . . . .	14
2.5.1	Wet icing . . . . .	15
2.5.2	Dry icing . . . . .	17
<b>3</b>	<b>Numerical method</b>	<b>19</b>
3.1	Calculation of wind spray . . . . .	19
3.2	Calculation of wave spray . . . . .	20
3.3	Numerical solution of the thermodynamic icing equations . . . . .	20
3.3.1	Two-step Lax-Wendroff method . . . . .	21
3.3.2	Method of lines . . . . .	23
3.4	Total icing on a given vessel . . . . .	24
3.4.1	Geometry . . . . .	24
3.4.2	Total spray flux to a polygon . . . . .	25
3.4.3	Shielding . . . . .	26
3.4.4	Runoff . . . . .	29
3.4.5	Icing calculations . . . . .	31
<b>4</b>	<b>Results</b>	<b>35</b>
4.1	Comparison with Jones and Andreas (2012) . . . . .	35
4.1.1	Ocean Bounty . . . . .	35
4.1.2	Icing rate . . . . .	35
4.1.3	Further comparison with Jones and Andreas (2012) . . . . .	36
4.2	Estimated icing rates on Norne, Skrugard and Shtokman . . . . .	39
4.2.1	Icing purely from wind spray . . . . .	39

4.2.2	Icing from both wind and wave spray . . . . .	44
4.2.3	Estimated annual occurrences of icing events . . . . .	54
4.3	Icing rates and comparison to ice thicknesses reported on AMI . . . . .	56
4.4	Comparison of icing rates calculated from meteorological observations and hindcast data . . . . .	59
4.5	Total icing on a vessel . . . . .	63
<b>5</b>	<b>Discussion</b>	<b>65</b>
5.1	Icing at Norne, Skrugard and Shtokman . . . . .	65
5.1.1	Melting and accumulation of ice . . . . .	65
5.1.2	Icing purely from wind spray . . . . .	65
5.1.3	Icing from both wind and wave spray . . . . .	66
5.2	Icing on AMI . . . . .	67
5.3	Total icing on a vessel . . . . .	67
5.4	Wind spray . . . . .	68
5.4.1	Accuracy of wind spray generation function . . . . .	68
5.4.2	Height dependency of spray concentration function . . . . .	69
5.4.3	Motion and temperature assumptions for wind spray . . . . .	69
5.5	Wave spray . . . . .	70
5.6	Icing calculations . . . . .	70
5.7	Meteorological observations and hindcast data . . . . .	71
5.8	Complete model . . . . .	72
5.8.1	Inclined and horizontal geometries . . . . .	72
5.8.2	Application of the model on different platform shapes . . . . .	73
<b>6</b>	<b>Conclusion and further work</b>	<b>75</b>
<b>7</b>	<b>Acknowledgements</b>	<b>77</b>
	<b>Bibliography</b>	<b>79</b>

# List of Figures

2.1	Map of the locations of Norne, Skrugard, Shtokman and AMI . . . . .	6
2.2	Illustration of wave spray jet . . . . .	14
3.1	Illustration of the modified Lax-Wendroff method . . . . .	23
3.2	Illustration of the method of lines . . . . .	24
3.3	Illustration of the difference between nodes and polygons . . . . .	25
3.4	Vessel geometry for Geofjord . . . . .	25
3.5	Illustration of the shielding algorithm . . . . .	28
3.6	Example of wave spray shielding for Geofjord . . . . .	29
3.7	Example of wave spray shielding for AMI . . . . .	29
3.8	Illustration of the runoff algorithm . . . . .	31
4.1	Icing rate for Ocean Bounty, using measured $H_s$ . . . . .	36
4.2	Icing rate for Ocean Bounty, using estimated $H_s$ . . . . .	37
4.3	Icing rate for Ocean Bounty, compared to results from Jones and Andreas (2012)	37
4.4	Estimated concentration distribution, using wind speed dependency $30U_{10}^4$ , compared to results from Jones and Andreas (2012) . . . . .	38
4.5	Estimated concentration distribution, using wind speed dependency $U_{10}^5$ , com- pared to results from Jones and Andreas (2012) . . . . .	38
4.6	Estimated wind icing rate for Norne, Skrugard and Shtokman . . . . .	40
4.7	Estimated wind ice thickness for Norne, Skrugard and Shtokman, assuming high melting . . . . .	41
4.8	Estimated wind ice thickness for Norne, Skrugard and Shtokman, assuming no melting . . . . .	42
4.9	Estimated wind spray flux for Norne, Skrugard and Shtokman . . . . .	43
4.10	Illustration of exposed column on Norne . . . . .	45
4.11	Estimated icing rate for Norne, Skrugard and Shtokman . . . . .	46
4.12	Estimated ice thickness for Norne, Skrugard and Shtokman, assuming high melting . . . . .	47
4.13	Estimated ice thickness for Norne, Skrugard and Shtokman, assuming no melting	48
4.14	Estimated wave spray flux for Norne, Skrugard and Shtokman . . . . .	49
4.15	Estimated icing rate for Norne, Skrugard and Shtokman, assuming spray jet starts at significant wave height . . . . .	50
4.16	Estimated ice thickness for Norne, Skrugard and Shtokman, assuming high melting and that spray jet starts in significant wave height . . . . .	51

4.17	Estimated ice thickness for Norne, Skrugard and Shtokman, assuming no melting and that spray jet starts in significant wave height . . . . .	52
4.18	Estimated icing rate for Norne, Skrugard and Shtokman, using the Overland (1990) algorithm . . . . .	53
4.19	Estimated annual occurrences of wind icing rates for Norne, Skrugard and Shtokman . . . . .	54
4.20	Estimated annual occurrences of icing rates for Norne, Skrugard and Shtokman	55
4.21	Estimated annual occurrences icing rates for Norne, Skrugard and Shtokman, assuming that the spray jet starts in significant wave height . . . . .	55
4.22	Picture of the weather ship AMI . . . . .	56
4.23	Estimated icing rates for AMI at the mast and the bridge, and when using the Overland (1990) algorithm . . . . .	57
4.24	Estimated ice thickness for AMI, assuming high melting . . . . .	58
4.25	Comparison of icing rates for Norne when calculating from meteorological observations and hindcast data . . . . .	60
4.26	Comparison of icing rates for AMI when calculating from meteorological observations and hindcast data . . . . .	60
4.27	Histogram of sub-zero temperatures at Norne for meteorological observations and hindcast data . . . . .	61
4.28	Histogram of high wind speeds at Norne for meteorological observations and hindcast data . . . . .	61
4.29	Histogram of sub-zero temperatures at AMI for meteorological observations and hindcast data . . . . .	62
4.30	Histogram of high wind speeds at AMI for meteorological observations and hindcast data . . . . .	62
4.31	Example of calculated icing distribution for the Geofjord vessel . . . . .	63
4.32	Example of calculated icing distribution for AMI . . . . .	64
4.33	Calculated icing distribution on the Norne vessel for the most severe icing case at the location of Shtokman . . . . .	64

## List of Tables

2.1	Variables used in the model . . . . .	4
2.2	Parameters that are assumed constant in the model . . . . .	5
2.3	Empirical coefficients used for calculating collision efficiency. . . . .	8
2.4	Values of $a_1$ , $b_1$ , $a_2$ and $b_2$ for different ranges of Rr . . . . .	10

# Chapter 1

## Introduction

According to the U.S. Geological Survey (Gautier et al., 2009), areas north of the Arctic Circle account for 13 percent of undiscovered petroleum resources and 30 percent of undiscovered natural gas, most of this offshore. Even though oil exploration and production in the Arctic is considered technically difficult, a combination of advances in technology and high oil prices has led to a surge of interest in petroleum exploration in the Arctic. There are, however, numerous environmental challenges connected to drilling and operating in the Arctic that must be considered, among them marine icing.

Icing refers to the accumulation of ice on ships and offshore structures due to the freezing of impinging sea spray or precipitation. Icing can lead to reduced operability, since the ice may accumulate on operational equipment or communication antennas, rendering them temporarily unusable. Even more serious, there are numerous safety hazards connected to icing, such as slippery rails, ladders or decks, unusable lifeboats and fire equipment or blocking of air vents. In the worst case scenario, the weight of the ice may even threaten the stability or integrity of the vessel. For a more thorough review of the hazards of icing, see Ryerson (2011). The ability to predict the severity and distribution of icing for given weather parameters or in certain areas is essential for mitigation or avoidance of icing hazards. Reduced risk of icing will lead to improved safety and efficiency for Arctic marine operations.

There are several different sources of icing. Atmospheric icing refers to icing due to the freezing of precipitation, such as rain or snow. This is generally believed to be less of a threat to ships and offshore structures than sea spray icing (marine icing), see Ryerson (2011), and will not be considered in the present model. Instead, the model will focus on two distinct sources of sea spray. The first will be the sea spray caused by droplets blowing off whitecaps on the ocean surface, hereafter referred to as ‘wind spray’. The wind spray is the source of a small but constant water flux that will be present in the air for all windy conditions. The implementation of wind spray used in the present model is based on a description from Jones and Andreas (2012). The second source of water comes from spraying by waves that collide with the vessel, hereafter referred to as ‘wave spray’. The wave spray is typically the source of a large but brief and periodic water flux that originates near the bow of the vessel and will blow to other components of the vessel. The implementation of wave spray is based on the description from Lozowski et al. (2000), which again is based on other work concerning wave spray on medium sized vessels. The numerical model will combine these two sources

of sea spray, and calculate the icing rate using differential equations for mass, heat and salt described in Horjen (1990).

In order to calculate the distribution of ice on a vessel, the model will use a polygon-based geometry where the icing rate is calculated for each polygon. The model will be able to take into account unfrozen brine that will run down vertical or inclined parts of the vessel (hereafter called 'runoff'), as well as polygons being shielded from sea spray by other structural elements of the vessel (hereafter called 'shielding'). The model will be run with hind-cast and meteorological observations from locations in the Norwegian and Barents Sea, and the results will be compared with pre-existing icing models.

# Chapter 2

## Data and theory

### 2.1 Practical information

Throughout the thesis, the following coordinate system will be used:

- The  $z$  axis has origin at the water surface, and is positive in the upward direction.
- The  $x$  and  $y$  axes are only relevant when a vessel geometry is being considered (see section 3.4). The  $x$  axis is directed towards the front of the vessel, and the  $y$  axis is directed towards the port side of the vessel.
- The position of the origin of the  $x$  and  $y$  axes should not affect any of the algorithms in the thesis, but generally the origin is positioned approximately at the center of the vessel.

A list of the main variables used in the thesis is given in table 2.1. Also, a list of the parameters assumed constant in the model (and the values that have been used) is given in table 2.2. The constant values for specific heat capacities, latent heats, viscosity parameters and air density are taken from the Engineering Toolbox (2012), and the values at 0°C and standard atmospheric pressure have been used. The sea water in the Norwegian and Barents Sea will be assumed to have a salinity of 34 ppt and a density of 1027 kg/m<sup>3</sup>. In addition, the slip factor, Von Kármán constant and ice accretion density are given in Jones and Andreas (2012), the wave spray droplet diameter is given in Lozowski et al. (2000), the relative amount of brine in the accretion is given by Horjen (1990) and the height of the boundary layer is taken from Fairall et al. (1996).

### 2.2 Sources of meteorological data

In order to test the model, weather data from locations in the Norwegian Sea and the Barents Sea have been used. The weather observations that are used in the model are from the FPSO (Floating production, storage and offloading) ‘Norne’ in the Norwegian Sea for the period January 2000 - January 2012, as well as from the weather ship ‘AMI’ in the Barents Sea for the period September 1976 - December 1984. The measurements have been obtained

Symbol	Variable	Dimension
$c_b$	Specific heat capacity of brine	J/(kg K)
$E$	Collision efficiency	-
$H_{bow}$	Height (asl) of vessel bow	m
$H_s$	Significant wave height	m
$I$	Rate of ice accretion	kg/m <sup>2</sup> s
$\mathbf{n}$	Unit vector normal to surface	-
$Q$	Heat flux	J/m <sup>2</sup> s
$q_{rel}$	Relative humidity of air	-
$q_r$	Specific humidity of air at reference height $z_r$	-
$q_s$	Saturation specific humidity at sea surface	-
$r$	Wind spray droplet radius	10 <sup>-6</sup> m(= 1 $\mu$ m)
$R_w$	Total spray water flux	kg/m <sup>2</sup> s
$S_b$	Brine salinity	ppt
$T_a$	Air temperature	°C
$T_b$	Brine temperature	°C
$T_d$	Droplet temperature	°C
$T_s$	Surface temperature	°C
$T_w$	Temperature of spray water flux	°C
$U$	Wind speed	m/s
$U_{10}$	Wind speed at 10 m asl	m/s
$u_*$	Friction velocity	m/s
$v_b$	Brine velocity	m/s
$\mathbf{v}_d$	Droplet velocity	m/s
$v_s$	Vessel speed	m/s
$X$	Local brine amount per area	kg/m <sup>2</sup>
$z_r$	Height (asl) where meteorological observations are made	m
$\alpha$	Angle between vessel heading and wind/wave direction	°
$\zeta$	Shielding factor	-
$\mu_b$	Dynamic viscosity of brine	Ns/m <sup>2</sup>
$\rho_b$	Brine density	kg/m <sup>3</sup>
$\tau_s$	Length of spray event	s
$\tau_p$	Period between spray events	s
$\tau_w$	Significant wave period	s

Table 2.1: Variables used in the model

Symbol	Parameter	Value	Dimension
$c_a$	Specific heat capacity of air	1005	J/(kg K)
$c_w$	Specific heat capacity of sea water	$3.93 \cdot 10^3$	J/(kg K)
$D$	Wave spray droplet diameter	1.75	mm
$f_s$	Slip factor	1	-
$g$	Acceleration due to gravity	9.81	m/s <sup>2</sup>
$k$	Von Kármán constant	0.40	-
$l_v$	Latent heat of vaporization for water	$2.27 \cdot 10^6$	J/kg
$l_f$	Latent heat of freezing for water	$3.34 \cdot 10^5$	J/kg
$P$	Atmospheric pressure	101325	Pa
$S_w$	Sea water salinity	34	ppt
$z_i$	Height of atmospheric boundary layer	600	m
$\mu_a$	Dynamic viscosity of air	$1.72 \cdot 10^{-5}$	Ns/m <sup>2</sup>
$\mu_w$	Dynamic viscosity of sea water	$1.79 \cdot 10^{-3}$	Ns/m <sup>2</sup>
$\nu_a$	Kinematic viscosity of air	$1.33 \cdot 10^{-5}$	m <sup>2</sup> /s
$\rho_a$	Air density	1.293	kg/m <sup>3</sup>
$\rho_w$	Sea water density	1027	kg/m <sup>3</sup>
$\rho_i$	Density of ice accretion (including entrapped brine and air)	900	kg/m <sup>3</sup>
$\sigma$	Relative amount of entrapped brine in ice accretion	0.34	-

Table 2.2: Parameters that are assumed constant in the model. The values are taken at 0°C and standard atmospheric pressure.

from the database of the Norwegian Meteorological Institute (eKlima, 2012). For AMI, ice thicknesses for some reported icing cases between December 1977 - September 1980 are also available (Eide, 1983). In addition, the ‘Nora10’ (Norwegian Re-Analysis 10 km, Reistad et al. (2010)) hindcast data are used to estimate the weather conditions at the locations of the undeveloped Skrugard/Havis and Shtokman fields in the Barents Sea for the period September 1957 - December 2009. In order to compare the measurements with the re-analysed data, ‘Nora10’ hindcast data for the locations of AMI and Norne is also used. The locations of Norne and AMI, as well as the Skrugard/Havis and Shtokman fields, are shown in figure 2.1.

In order to test their formulation for wind spray, Jones and Andreas (2012) apply their model to the semi-submersible drilling rig Ocean Bounty. During the winter of 1979-1980, meteorological observations as well as approximate icing rates for several icing events were recorded on Ocean Bounty. The icing events on Ocean Bounty are explained in more detail in Nauman (1984), and the meteorological and icing data are listed in Jones and Andreas (2009). In section 4.1, the implementation of wind spray used in the present model has been applied to the Ocean Bounty data and compared to the results from Jones and Andreas (2012), in an attempt to verify that the wind spray calculations have been correctly implemented.

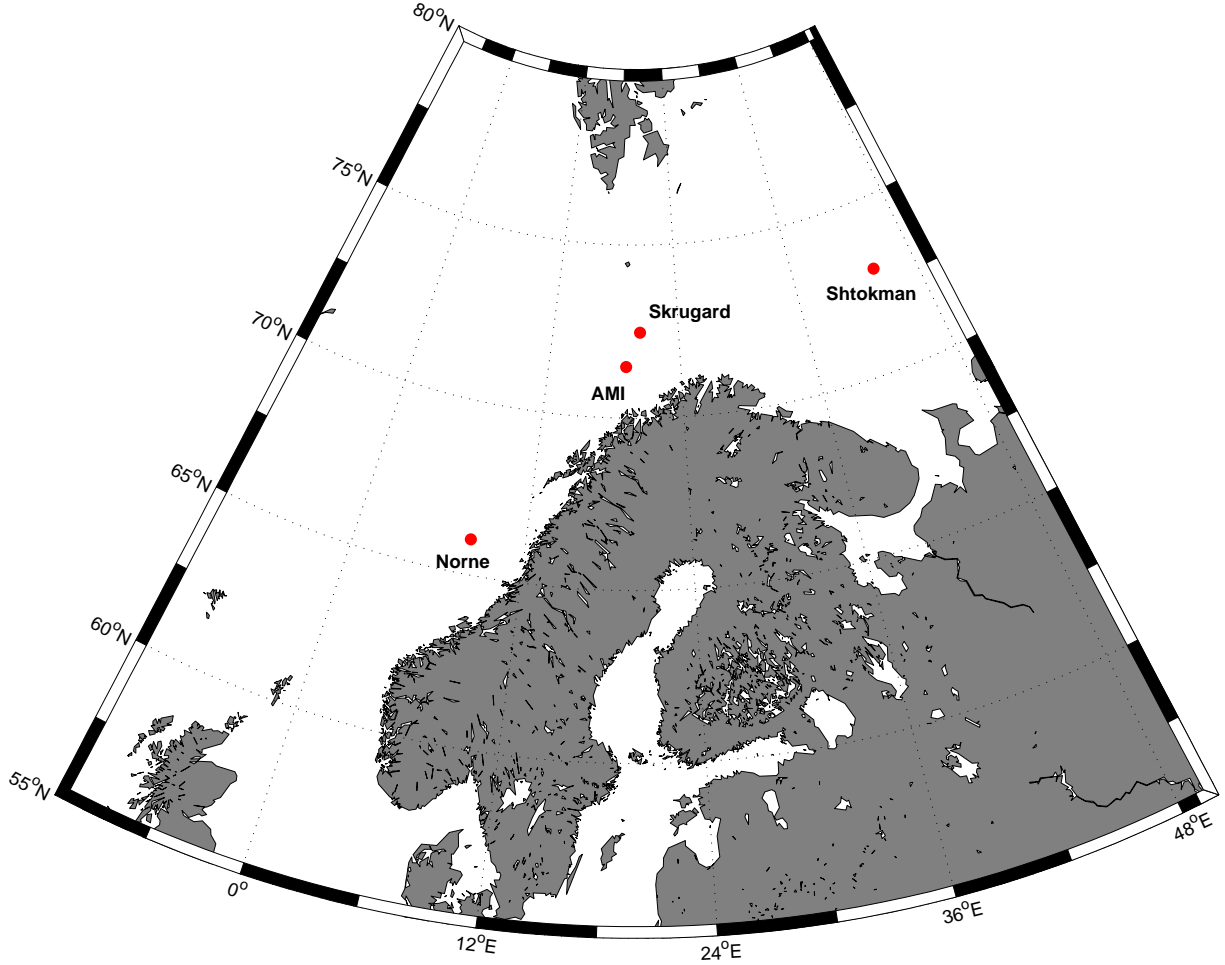


Figure 2.1: Map of the locations of the Norne, Skrugard and Shtokman fields, as well as the location of the weather ship AMI.

## 2.3 Wind-induced spray

The theory behind the model formulation for wind-induced spray is presented in the following sections. The presentation is largely based on the work by Jones and Andreas (2012), but an effort has been made to give a more complete description of elements in the model that are only vaguely described in the original paper.

### 2.3.1 Sea spray concentration at the sea surface

In order to calculate the concentration distribution generated at the water surface, Jones and Andreas (2012) use empirical relations between the sea spray concentration functions and  $U_{10}$ , which is the wind speed at a reference height of 10 meters. For low to moderate wind speeds ( $U_{10} < 19 \text{ m s}^{-1}$ ), they use a concentration function  $\frac{dC(r)}{dr}$  described by Lewis

and Schwartz (2004), which they rewrite as

$$\frac{dC(r)}{dr} [\text{m}^{-3} \mu\text{m}^{-1}] = \frac{7 \cdot 10^4 U_{10}^2}{r} \exp \left( -\frac{1}{2} \left[ \frac{\ln(r/0.3)}{\ln 2.8} \right]^2 \right), \quad (2.1)$$

where  $r$  is the droplet radius in micrometers. The concentration function is the number of droplets per cubic meter as a distribution over droplet radius  $r$ , i.e.  $dC(r)$  is the number of droplets per cubic meter with a radius between  $r$  and  $r + dr$ . For higher wind speeds ( $U_{10} > 19 \text{ m s}^{-1}$ ), Jones and Andreas (2012) modify this equation to

$$\frac{dC(r)}{dr} [\text{m}^{-3} \mu\text{m}^{-1}] = \frac{30U_{10}^4}{r} \exp \left( -\frac{1}{2} \left[ \frac{\ln(r/0.3)}{\ln 4} \right]^2 \right), \quad (2.2)$$

based on experimental data for the concentration function at higher wind speeds.

### 2.3.2 Height dependency of the spray concentration

In order to determine the vertical variation of the spray concentration, Jones and Andreas (2012) use the formulation provided by Fairall et al. (2009):

$$\frac{dC(r, z)}{dr} = \frac{dC(r, h)}{dr} \left( \frac{z}{h} \right)^{\frac{-v_g(r)}{ku^* f_s}} \quad (2.3)$$

where  $k = 0.40$  is the von Kármán constant,  $f_s \approx 1$  is the slip factor and  $u^*$  is the friction velocity, more thoroughly described in section 2.3.4. The height  $h$  is taken as the upper limit of the source region for the spray droplet generation. It is assumed that  $h = 1 \text{ m}$  for  $U_{10} < 19 \text{ m s}^{-1}$  and  $h = 0.5H_s$  for higher wind speeds, where  $H_s$  is the significant wave height. The function  $v_g(r)$  is the terminal fall velocity of the droplets. Notice the minus sign in the exponent of  $\frac{z}{h}$ , which is not in the original paper by Jones and Andreas (2012). In the present thesis,  $v_g$  is defined as positive, hence the minus sign is retained.

The fall velocity function is given by

$$v_g(r) = \frac{2r^2 g}{9\nu_a [1 + 0.158(2rv_g/\nu_a)^{2/3}]} \left( \frac{\rho_w}{\rho_a} - 1 \right), \quad (2.4)$$

as described in Andreas (1990), where  $g = 9.81 \text{ m s}^{-2}$  is the acceleration due to gravity,  $\nu_a$  is the kinematic viscosity of air,  $\rho_a$  is the density of air and  $\rho_w$  is the density of the droplet solution, assumed to be equal to the density of sea water. According to Andreas (1990), this equation is solved by Newton's method. However, since the equation is undefined for  $v_g < 0$  and its derivative is undefined for  $v_g \leq 0$ , using Newton's method may be problematic. In the present model, the bisection method is used instead.

### 2.3.3 Simple icing calculations

Once the concentration profile has been defined, the liquid water content of the spray is calculated from

$$\frac{dW(r, z)}{dr} = \rho_w \frac{4}{3} \pi r^3 \frac{dC(r, z)}{dr}, \quad (2.5)$$

Coefficient		Coefficient		Coefficient	
$C_1$	1.066	$C_5$	-0.028	$C_9$	-0.498
$C_2$	$-6.16 \cdot 10^{-3}$	$C_6$	$6.37 \cdot 10^{-3}$	$C_{10}$	-1.497
$C_3$	-1.103	$C_7$	0.381	$C_{11}$	-0.694
$C_4$	-0.688	$C_8$	3.641	$C_{12}$	-0.045

Table 2.3: Empirical coefficients used for calculating collision efficiency.

where  $\rho_w$  is the density of sea water. Jones and Andreas (2012) use a simplified model to calculate the icing on a reference cylinder, where they assume that for air temperatures below  $0^\circ\text{C}$ , all the water that hits the cylinder will freeze. Thus, the icing rate is

$$\frac{dI(z)}{dt} = \frac{U(z)}{\rho_i} \int_{r_{min}}^{r_{max}} E(U, r, D_c) \frac{dW(r, z)}{dr} dr, \quad (2.6)$$

where  $U(z)$  is the wind speed at height  $z$ ,  $\rho_i$  is the density of the accreted ice (Jones and Andreas, 2012) and  $E(U, r, D_c)$  is the collision efficiency, i.e. the probability that a droplet of radius  $r$  will adhere to a cylinder of diameter  $D_c$ . The collision efficiency is provided by Finstad et al. (1988):

$$E(K, \phi) = C_1 K^{C_2} \exp(C_3 K^{C_4}) + C_5 - C_6 (\phi - 100)^{C_7} [C_8 K^{C_9} \exp(C_{10} K^{C_{11}}) + C_{12}], \quad (2.7)$$

which they obtain by performing a nonlinear regression analysis on experimental data. Here,

$$K = \frac{4\rho_w r^2 U(z)}{9\mu_a D_c}$$

is the Stokes number and

$$\phi = \frac{(2U(z)r\rho_a/\mu_a)^2}{K}$$

is the Langmuir parameter. Also,  $\mu_a$  is the dynamic viscosity of air and  $r$  is the droplet radius in meters rather than micrometers. The empirical coefficients  $C_1$  to  $C_{12}$  are listed in table 2.3.

### 2.3.4 Calculating friction velocity and wind profile

Jones and Andreas (2012) mention in the paper that the friction velocity as well as the wind profile is calculated from an algorithm described by Andreas et al. (2008). Implementing this algorithm into the model presented some challenges, partly because the algorithm itself is complex, and partly because it is not described completely in any single article. This section will try to describe the implemented algorithm in full, by clearly stating all necessary equations and parameters and the references where they may be found.

As mentioned by Andreas et al. (2008), the algorithm is a modified version of the COARE 2.6 algorithm (Fairall et al., 1996). Using the Fairall notation, the turbulent fluxes of stress

$\tau$ , latent heat  $H_l$  and sensible heat  $H_s$  near the sea-air interface are given by

$$\tau = -\rho_a C_d S_r^2 \equiv -\rho_a u_*^2, \quad (2.8)$$

$$H_s = \rho_a c_a C_h S_r (T_s - T_a) \equiv -\rho_a c_a u_* T_*, \quad (2.9)$$

$$H_L = \rho_a l_v C_e S_r (q_s - q_r) \equiv -\rho_a l_v u_* q_*, \quad (2.10)$$

where  $S_r$ ,  $T_a$  and  $q_r$  are the effective wind speed, potential temperature and specific humidity at a reference height  $z_r$ , and  $T_s$  and  $q_s$  are the potential temperature and specific humidity at the surface, respectively. Here, the convention of positive fluxes pointing in positive z-direction (upward) is used. In addition,  $\rho_a$  is air density,  $c_a$  is the specific heat of air at constant pressure and  $l_v$  is the latent heat of vaporization. The transfer coefficients  $C_d$ ,  $C_h$  and  $C_e$  are described in equations (2.14) - (2.16).

The friction velocity  $u_*$  is defined by equation (2.8).  $T_*$  and  $q_*$  are similar parameters for temperature and humidity defined by equations (2.9) and (2.10) respectively. Notice that equation (2.8) uses  $S_r$  in place of the relative difference between wind speed and surface current that Fairall et al. (1996) uses - this is because the surface current is assumed to be negligible compared to the wind speed.

The fluxes themselves are not of interest to our model - only the friction velocity as well as the parameters  $T_*$  and  $q_*$  are used in calculating the wind profile. From equations (2.8) - (2.10), we have

$$u_* = C_d^{1/2} S_r, \quad (2.11)$$

$$T_* = C_h S_r (T_a - T_s) / u_* = \frac{C_h}{C_d^{1/2}} (T_a - T_s), \quad (2.12)$$

$$q_* = C_e S_r (q_r - q_s) / u_* = \frac{C_e}{C_d^{1/2}} (q_r - q_s). \quad (2.13)$$

The transfer coefficients are given by

$$C_d = \frac{k^2}{[\ln(z_r/z_0) - \psi_m(z_r/L)]^2}, \quad (2.14)$$

$$C_h = \frac{k^2}{[\ln(z_r/z_0) - \psi_m(z_r/L)] [\ln(z_r/z_T) - \psi_h(z_r/L)]}, \quad (2.15)$$

$$C_e = \frac{k^2}{[\ln(z_r/z_0) - \psi_m(z_r/L)] [\ln(z_r/z_q) - \psi_h(z_r/L)]}, \quad (2.16)$$

which, when inserted into equations (2.11) - (2.13), give

$$u_* = \frac{k}{[\ln(z_r/z_0) - \psi_m(z_r/L)]} S_r, \quad (2.17)$$

$$T_* = \frac{k}{[\ln(z_r/z_T) - \psi_h(z_r/L)]} (T_a - T_s), \quad (2.18)$$

$$q_* = \frac{k}{[\ln(z_r/z_q) - \psi_h(z_r/L)]} (q_r - q_s). \quad (2.19)$$

Here,  $z_r$  is the reference height where the measurements of wind speed, humidity and temperature are made. The parameters  $z_0$ ,  $z_T$  and  $z_q$  are roughness lengths for wind speed, temperature and humidity, respectively, and  $\psi_m$  and  $\psi_h$  are empirical stratification corrections that are functions of  $z_r/L$ . The Monin-Obukhov length  $L$  is given by Fairall et al. (1996) as

$$L = \frac{T_a u_*^2}{kg(T_* + 0.61T_a q_*)}. \quad (2.20)$$

The roughness length for wind speed,  $z_0$ , is given by Andreas et al. (2008) as

$$z_0 = 0.135 \frac{\nu_a}{u_*} + 0.0185 \frac{u_*^2}{g}. \quad (2.21)$$

The roughness lengths for temperature and humidity,  $z_T$  and  $z_q$ , are provided by Liu et al. (1979) as

$$z_T = \frac{\nu_a}{u_*} a_1 \text{Rr}^{b_1}, \quad (2.22)$$

$$z_q = \frac{\nu_a}{u_*} a_2 \text{Rr}^{b_2}. \quad (2.23)$$

where  $\text{Rr} = z_0 u_* / \nu_a$  is the roughness Reynolds number and the coefficients  $a_1$ ,  $b_1$ ,  $a_2$  and  $b_2$  are listed in table 2.4. The values for  $100 < \text{Rr} < 1000$  are taken from the source code for the Coupled Ocean-Atmosphere Response Experiment flux algorithm, version 2.5b (COARE, 2012), where it is accredited to ‘Moana wave data’. Both the effective wind speed and the

	Rr		$a_1$	$b_1$	$a_2$	$b_2$
	0	-	0.11	0.177	0	0.292
	0.11	-	0.825	1.376	0.929	1.828
	0.825	-	3.0	1.026	-0.599	1.393
	3.0	-	10.0	1.625	-1.018	1.956
	10.0	-	30.0	4.661	-1.475	4.994
	30.0	-	100.0	34.904	-2.067	30.790
	100.0	-	300.0	1667.19	-2.907	1448.68
	300.0	-	1000.0	$5.88 \cdot 10^5$	-3.935	$2.98 \cdot 10^5$

Table 2.4: Values of  $a_1$ ,  $b_1$ ,  $a_2$  and  $b_2$  for different ranges of Reynolds roughness number Rr.

stratification corrections depend on the stratification stability. The sign of the parameter  $z_r/L$  is used as indication of this stability, and it is assumed that conditions are stable for  $z_r/L \geq 0$  and unstable for  $z_r/L < 0$ . For stable conditions, the effective wind speed is given by

$$S_r = U + 0.5 \operatorname{sech}(U), \quad (2.24)$$

where  $U$  is the measured wind speed at the reference height  $z_r$ , and the correction functions are provided by Holtslag and de Bruin (1988):

$$\psi_m = -a \frac{z_r}{L} - b \left( \frac{z_r}{L} - \frac{c}{d} \right) \exp \left( -d \frac{z_r}{L} \right) - \frac{bc}{d}, \quad (2.25)$$

$$\psi_h = \psi_m. \quad (2.26)$$

Here, the parameters are  $a = 0.7$ ,  $b = 0.75$ ,  $c = 5$  and  $d = 0.35$ . It should be mentioned that a more recent paper by Beljaars and Holtslag (1991) uses parameters  $a = 1$ ,  $b = 0.667$ ,  $c = 5$  and  $d = 0.35$  and changes  $\psi_h$  to

$$\psi_h = - \left( 1 + \frac{2}{3} \frac{az_r}{L} \right)^{3/2} - b \left( \frac{z_r}{L} - \frac{c}{d} \right) \exp \left( -d \frac{z_r}{L} \right) - \frac{bc}{d} + 1.$$

However, in the present model equations (2.25) and (2.26) are still used, in order to correspond with Andreas et al. (2008). For unstable conditions, the effective wind speed is

$$S_r = (U^2 + \beta_g^2 w_*^2)^{1/2}, \quad (2.27)$$

where  $\beta_g = 1.25$  (Andreas et al., 2008) and  $w_*$  is provided by Godfrey and Beljaars (1991):

$$w_* = (-u_* b_* z_i)^{1/3},$$

where  $z_i$  is the boundary layer height (assumed to be  $z_i = 600$  m in the model, see Fairall et al. (1996)) and the buoyancy flux  $b_*$  comes from  $L = u_*^2 / (k b_*)$ , which together with equation (2.20) gives

$$b_* = \frac{g}{T_a} (T_* + 0.61 T_a q_*).$$

The correction functions for unstable conditions are taken from Paulson (1970):

$$\psi_m = 2 \ln [(1+x)/2] + \ln [(1+x^2)/2] - 2 \tan^{-1} x + \pi/2, \quad (2.28)$$

$$\psi_h = 2 \ln [(1+x^2)/2], \quad (2.29)$$

where

$$x \equiv (1 - \gamma z_r / L)^{1/4},$$

and  $\gamma = 16$ . It should be mentioned that Höögström (1996) recommends using  $\gamma = 19$ , but  $\gamma = 16$  is used in order to correspond with Andreas et al. (2008).

Since  $z_0$ ,  $z_T$ ,  $z_q$ ,  $L$  and  $S_r$  all depend on  $u_*$ ,  $T_*$  and  $q_*$ , it is obvious that (2.17) - (2.19) cannot be solved directly and that the algorithm must be iterative. The details of the iterative solutions are described in section 3.1. Once the algorithm converges, the resulting values for  $u_*$ ,  $T_*$ ,  $q_*$  and  $z_0$  are used to calculate the logarithmic wind profile:

$$U(z) = \frac{u_*}{k} \left[ \ln \left( \frac{z}{z_0} \right) - \psi_m \left( \frac{z}{L} \right) \right]. \quad (2.30)$$

Here,  $L$  is calculated from equation (2.20) and  $\psi_m$  is a height-dependent function that is calculated from equation (2.25) or (2.28), depending on stability. One may observe that, if equation (2.17) is solved for  $S_r$ , the expression for  $S_r$  will be identical to the expression for  $U(z)$  in equation (2.30). In other words, it appears the  $U(z)$  calculated in equation (2.30) is actually the effective wind speed  $S_r$ . From equations (2.24) and (2.27), one may observe that  $S_r$  will be larger than the measured wind speed  $U$  - this is because  $S_r$  accounts for gustiness in the air. One might therefore argue that expression for wind speed given by equation (2.30) should contain a similar but opposite transformation from  $S_r$  to  $U$  - this is done in

the COARE 2.5 code (COARE, 2012). However, Jones and Andreas (2012) do not appear to have used this correction, so neither does the present model. For high wind speeds, where the wind spray is most important, the gustiness will be insignificant compared to the wind and the effective wind speed  $S_r$  and the measured wind speed  $U$  will be approximately equal.

Finally, if measurements of specific humidity are unavailable (which they generally are), the model will calculate the specific humidities based on the relative humidity of air. The air very close to the ocean surface is assumed to be saturated and at a temperature equal to the surface temperature. The saturation vapour pressure is calculated from Tetens's formula for saturation as stated in Buck (1981),

$$e_{sat}(T, P) = [1.0007 + 3.46 \cdot 10^{-6}P] \cdot 6.1121 \exp \left[ \frac{17.502T}{240.97 + T} \right], \quad (2.31)$$

where  $T$  is the temperature in °C,  $P$  is the pressure in mb and  $e_{sat}$  is the resulting saturation vapour pressure in mb. The resulting vapour pressures (Fairall et al., 1996) are

$$e_r = q_{rel} \cdot e_{sat}(T_a, P), \quad (2.32)$$

$$e_s = 0.98 \cdot e_{sat}(T_s, P), \quad (2.33)$$

where  $q_{rel}$  is the relative humidity of air and 0.98 is a factor that accounts for the effect of salinity. Finally, the humidities are converted from pressure to specific humidity by the equation

$$q_{r,s} = \frac{0.62197e_{r,s}}{P - 0.378e_{r,s}}. \quad (2.34)$$

## 2.4 Spray due to wave collisions

The theory behind the treatment of wave collision spray is based on a review paper by Lozowski et al. (2000), which mainly synthesizes the work by, among others, Blackmore et al. (1989) and Zakrzewski (1987).

Lozowski et al. (2000) make numerous assumptions about the spray generated by wave-vessel collisions that should be explained before listing the relevant equations:

- During a spray event, there will exist a spray jet (in the form of a thin liquid sheet) that follows the bow of the ship. The jet will start at the forward tip of the ship, and extend symmetrically along the bow. See figure 2.2 for a visual representation of the spray jet.
- The spray jet will initially be at rest in a coordinate system that follows the ship.
- The vertical distribution of water in the spray jet depends on the height above the bow, rather than the height above the water surface. In other words, the spray jet for large vessels (where the bow is positioned far above the surface) will be identical to the spray jet for smaller vessels.

The validity of these assumptions will be further discussed in section 5.5.

Lozowski et al. (2000) use the following vertical distribution of water in the spray jet,  $w(z)$  [ $\text{kg}/\text{m}^3$ ],

$$w(z) = 6.46 \cdot 10^{-5} H_s v_{sw}^2 e^{-(z-H_{bow})/1.82}, \quad (2.35)$$

where  $H_s$  is the significant wave height and  $H_{bow}$  is the height of the bow above surface level. Notice that this thesis uses a coordinate system where  $z = 0$  at the water surface, rather than  $z = 0$  at the bow, which Lozowski et al. (2000) use. The parameter  $v_{sw}$  is the vessel speed relative to the waves, which is given as

$$v_{sw} = 1.56\tau_w + v_s \cos(\pi - \alpha),$$

where  $\tau_w$  is the significant wave period,  $v_s$  is the vessel speed and  $\alpha$  is the angle between vessel heading and the wind/wave direction (the wind and wave direction are assumed to be equal in the present model). Here,  $\alpha = 0$  when the vessel heading is directly against the wind. The spray jet is assumed to start at the tip of the bow and extend symmetrically along both sides of the ship to a distance  $x_e$  given by

$$x_e = 2.0H_s + 0.04v_{sw}^2 - 10.0. \quad (2.36)$$

If  $x_e$  is negative, it is assumed that there is no spray jet. It is assumed the spray extends up to a maximum height of

$$H_m = H_s + \frac{v_{sw}^2}{2g}.$$

The duration of a spray event is given by Zakrzewski (1987) as

$$\tau_s = \frac{10.0v_{sw}H_s}{U_{10}^2} \quad (2.37)$$

where  $U$  is the wind speed. It is assumed that a spray jet is created once by every fourth wave encounter, which gives a total time period between spray events of

$$\tau_p = 4 \cdot \frac{1.56\tau_w^2}{v_{sw}}. \quad (2.38)$$

Lozowski et al. (2000) also provide equations for the droplet trajectory and droplet cooling. The droplet equation of motion is

$$\frac{d\mathbf{v}_d}{dt} = -\frac{3}{4} \frac{C_d}{D} \frac{\rho_a}{\rho_w} |\mathbf{v}_d - \mathbf{U}_{10}| (\mathbf{v}_d - \mathbf{U}_{10}) - \mathbf{g} \left( \frac{\rho_a}{\rho_w} - 1 \right). \quad (2.39)$$

where  $\mathbf{v}_d$  is the droplet velocity,  $D$  is the droplet diameter and  $\rho_a$  and  $\rho_w$  the density of air and sea water respectively. Lozowski et al. (2000) assume that all droplets in the spray jet have a diameter of  $D = 1.75$  mm. This significantly simplifies the spray flux calculations, since all droplets will have identical trajectories and velocities, but in reality the spray jet will consist of a range of droplet sizes. The drag coefficient  $C_d$  is given by Langmuir and Blodgett (1946) as

$$C_d = \frac{24.0}{Re} + \frac{4.73}{Re^{0.37}} + 6.24 \cdot 10^{-3} Re^{0.38},$$

where  $Re$  is the dimensionless Reynolds number, which is calculated from

$$Re = \frac{D}{\nu_a} |\mathbf{v}_d - \mathbf{U}_{10}|.$$

The droplet cooling equation is given as

$$mc_w \frac{dT_d}{dt} = \pi D^2 (C + E + R), \quad (2.40)$$

where  $m$  is the mass of the droplet,  $c_w$  the specific heat capacity of the sea water,  $T_d$  the droplet temperature and  $C$ ,  $E$  and  $R$  are the convective, evaporative and radiant heat fluxes to the droplet respectively. The straight forward expressions for  $C$ ,  $E$  and  $R$  can be found in Lozowski et al. (2000). Finally, the water flux  $R_w$  from the spray onto a surface located at position  $\mathbf{r}$  is calculated by

$$R_w(\mathbf{r}) = w(z_{int}) |\mathbf{v}_d \cdot \mathbf{n}| \quad (2.41)$$

where  $z_{int}$  is the height above the bow where the droplet trajectory from  $\mathbf{r}$  intersects the spray jet,  $\mathbf{v}_d$  is the droplet velocity at position  $\mathbf{r}$  and  $\mathbf{n}$  is the unit vector normal to the surface.

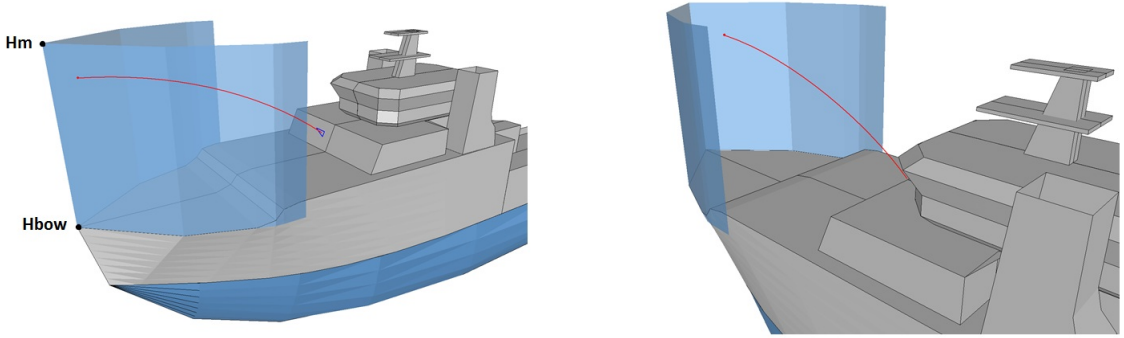


Figure 2.2: Illustration of a spray jet (transparent blue) on the offshore supply vessel Geofjord. The spray jet will encircle the bow of the vessel and extend from  $H_{bow}$  to  $H_m$  in the  $z$  direction. In order to calculate the flux to a polygon (a small polygon is framed in blue on the left figure), the droplet trajectory (red) from the polygon to the spray jet is calculated. The water content of the spray that hits the polygon equals the water content of the point where the droplet trajectory hits the spray jet.

## 2.5 Icing calculations

The thermodynamic icing calculations are based on the differential equations described in Horjen (1990). In general, the heat flux away from a surface exposed to water spray will be insufficient to freeze or entrap all the impinging water. In the special case where the heat flux *is* sufficient, the icing calculations are vastly simplified. This is referred to as ‘dry icing’, and the conditions for dry icing to occur are explained in section 2.5.2. However, as long

as these conditions are not met, Horjen (1990) assumes there will be a film of brine present on the surface where icing is being calculated. This will be referred to as ‘wet icing’, and is described in the section below.

### 2.5.1 Wet icing

Conservation of mass, heat and salt give the following approximate differential equations for the brine film,

$$\frac{\partial X}{\partial t} + \nabla_t \cdot (\mathbf{v}_b X) = R_w - I, \quad (2.42)$$

$$c_b X \left( \frac{\partial}{\partial t} + \mathbf{v}_b \cdot \nabla_t \right) T_b = Q + (1 - \sigma) l_f I, \quad (2.43)$$

$$\frac{X}{S_b} \left( \frac{\partial}{\partial t} + \mathbf{v}_b \cdot \nabla_t \right) S_b = I(1 - \sigma) - R_w \left( 1 - \frac{S_w}{S_b} \right). \quad (2.44)$$

Here,  $X$  is the local brine amount per unit area [ $\text{kg}/\text{m}^2$ ],  $T_b$  is the brine temperature and  $S_b$  is the brine salinity (in parts per thousand). The parameter  $v_b$  is the brine velocity, and  $\nabla_t$  is the differential operator in the tangential direction (i.e. along the direction that the brine will move in). Also,  $R_w$  [ $\text{kg}/\text{m}^2\text{s}$ ] is the impinging sea spray flux, and  $I$  [ $\text{kg}/\text{m}^2\text{s}$ ] is the rate of accretion formation which includes both the ice and the brine entrapped in the ice. In addition,  $c_b$  is the specific heat capacity of the brine (at constant pressure),  $\sigma$  is the fraction of entrapped brine in the accretion (estimated to be 0.34 in Horjen (1990)),  $l_f$  is the latent heat of freezing and  $S_w$  is the salinity of seawater. Notice that mass flux due to evaporation is neglected. The total heat flux to the brine,  $Q$ , is given by

$$Q = -(Q_c + Q_e + Q_r + Q_s), \quad (2.45)$$

where  $Q_c$ ,  $Q_e$ ,  $Q_r$ ,  $Q_s$  are the convective, evaporative, radiative and sensible heat flux *away* from the brine (heat flux through the ice layer is neglected). Equations for the heat fluxes are provided by both Horjen (1990) and Lozowski et al. (2000). The present model uses the heat flux equations from Lozowski et al. (2000).

One may now find the icing rate  $I$  by using a relationship between salinity and brine temperature. This model will use the relation given by Assur (1958):

$$T_b = -\frac{aS_b}{1 - 10^{-3}S_b} \quad , \quad S_b < 125$$

$$T_b = -\frac{bS_b}{1 - 10^{-3}S_b} + c \quad , \quad 125 \leq S_b < 230$$

where

$$a = 5.4113 \cdot 10^{-2} \text{ } ^\circ\text{C},$$

$$b = 9.7007 \cdot 10^{-2} \text{ } ^\circ\text{C},$$

$$c = 6.0533 \text{ } ^\circ\text{C}.$$

Horjen (1990) actually uses a slightly different relationship between salinity and brine temperature. The reference to Assur (1958) is used in an older report from Horjen and Vefsnmo (1987), and is also applied in the present model because it is better documented. One may observe that

$$\frac{dS_b}{dT_b} = -\frac{\kappa}{(1 - 10^{-3}S_b)^2},$$

where the constant  $\kappa$  is  $a$  or  $b$ , depending on salinity. This means that

$$\left(\frac{\partial}{\partial t} + \mathbf{v}_b \cdot \nabla_t\right) S_b = -\frac{k}{(1 - 10^{-3}S_b)^2} \left(\frac{\partial}{\partial t} + \mathbf{v}_b \cdot \nabla_t\right) T_b,$$

which can be used to combine equations (2.43) and (2.44), resulting in

$$I(1 - \sigma) - R_w \left(1 - \frac{S_w}{S_b}\right) = -F(S_b) \left(\frac{Q}{l_f} + I(1 - \sigma)\right),$$

where

$$F(S_b) = K_0 \frac{(1 - 10^{-3}S_b)^2}{S_b},$$

$$\begin{aligned} K_0 &= l_f/(ac_b) \approx 1.46 \cdot 10^3 & , & & S_b < 125, \\ K_0 &= l_f/(bc_b) \approx 8.16 \cdot 10^2 & , & & 125 < S_b < 230. \end{aligned}$$

Solving for  $I$ , this gives

$$I = \frac{(1 - S_w/S_b)R_w - \frac{F(S_b)}{l_f}Q}{(1 - \sigma)(1 + F(S_b))}. \quad (2.46)$$

By introducing a variable  $Y \equiv XS_b$ , and the assumption that the brine will travel only in the negative  $z$  direction, the following equations may be derived from equations (2.42) and (2.44):

$$\frac{\partial X}{\partial t} + \frac{\partial}{\partial z}(v_b X) = R_w - I, \quad (2.47)$$

$$\frac{\partial Y}{\partial t} + \frac{\partial}{\partial z}(v_b Y) = R_w S_w - \sigma I \frac{Y}{X}. \quad (2.48)$$

For flat and purely vertical geometries, Horjen (1990) gives the brine velocity  $v_b$  as

$$v_b = -0.264 \frac{g}{\rho_b \mu_b} X^2, \quad (2.49)$$

where  $\rho_b$  is the brine density and  $\mu_b$  is the dynamic viscosity of the brine.

## 2.5.2 Dry icing

If the spray flux is sufficiently low and the weather is sufficiently cold, it is possible for all the incoming spray to freeze on impact. As described by Horjen (1990), the requirement for this to happen (neglecting mass evaporation) is

$$R_w \leq \frac{Q_c + Q_e + Q_r}{-Q_s/R_w + l_f(1 - \sigma)}, \quad (2.50)$$

where  $R_w$  is the spray flux during the spray event. This is simply derived from the condition that the heat transport away from the brine must be greater than or equal to the latent heat produced if all the impinging spray freezes, i.e.

$$l_f(1 - \sigma)R_w \leq Q_c + Q_e + Q_r + Q_s.$$

The salinity  $S_b$  required for calculating the heat fluxes is estimated from

$$S_b = S_w/\sigma.$$

If the  $z$  dependency of  $R_w$  is known, the point  $z_t$  where the transition from dry to wet icing occurs can be found. For all points above  $z_t$ , the ice accretion rate equals the spray flux. It is of course possible that  $z_t$  lies above or below the object where the icing is being calculated, in which case we will have completely wet icing or completely dry icing. Also, even though the spray flux will be reduced after the spray event, the transition level should be the same for the entire spray cycle. This is because all points below the transition point will have  $X > 0$  directly after the spray event, which makes the icing calculations using differential equations necessary even after the spray event.



# Chapter 3

## Numerical method

### 3.1 Calculation of wind spray

In order to calculate the wind spray profile, the friction velocity  $u_*$  and roughness length  $z_0$ , along with the parameters  $T_*$  and  $q_*$ , must be calculated. These variables will be solved using the iteration method. Required inputs are the reference height where measurements are available, the measured wind speed  $U_r$ , air temperature  $T_a$  and surface temperature  $T_s$ . Relative humidity  $q_{rel}$  is an optional input - if no humidity measurements are available, the function assumes  $q_{rel} = 0.8$ . During the icing events of Ocean Bounty, Nauman (1984) reported relative humidities ranging from 0.5 to 0.95, with an average close to 0.8, so this seems to be a reasonable estimate. The relative humidity  $q_{rel}$  is converted to specific humidities  $q_r$  and  $q_s$  by using the equations (2.31), (2.32) and (2.34).

The equations used to calculate  $u_*$ ,  $T_*$  and  $q_*$  are thoroughly described in section 2.3.4. Before the iterations start, initial parameters  $u_* = 0.3$  m/s,  $T_* = 0.04(T_a - T_s)$  and  $q_* = 0.04(q_r - q_s)$  are chosen. The initial parameters are taken from the COARE source code (COARE, 2012), and the solution should not be affected if different initial parameters are chosen. For each iterative step, the function will first calculate the roughness lengths  $z_0$ ,  $z_T$  and  $z_q$  using equations (2.21) - (2.23). A lower limit of  $7 \cdot 10^{-8}$  m is enforced for both  $z_T$  and  $z_q$ , as described in Andreas et al. (2008). Next, the Obukhov length  $L$  is calculated from equation (2.20) and the stability of the stratification is found from the sign of  $z/L$ . If stable, the function will calculate effective wind speed  $S_r$  along with stability corrections  $\psi_m$  and  $\psi_h$  from equations (2.24) - (2.26). If unstable, equations (2.27) - (2.29) are used instead. Finally,  $u_*$ ,  $T_*$  and  $q_*$  are calculated from equations (2.17) - (2.19) and used as input for the next iteration. The iterations stop when the difference between the friction velocities resulting from subsequent iterations is smaller than the parameter  $\delta$ . Since  $u_*$  appears to converge rapidly, a limit as low as  $\delta = 10^{-5}$  is currently used in the model.

Once these parameters have been calculated, they are used to calculate  $U_{10}$ , the wind speed at 10 meters, and  $U_z$ , the wind speed at height  $z$ , using equation (2.30). If  $U_{10} < 19$  m/s, the maximum droplet radius assumed to contribute to icing is set to 100  $\mu\text{m}$ , for higher wind speeds it is set to 200  $\mu\text{m}$ , as described by Jones and Andreas (2012). The minimum droplet radius assumed to contribute to icing is always 5  $\mu\text{m}$ . Next, the droplet concentration at the ocean surface  $\frac{dC(r,h)}{dr}$  is calculated using equation (2.1) for  $U_{10} < 19$  m/s and equation

(2.2) for higher wind speeds. The height dependent concentration  $\frac{dC(r,z)}{dr}$  is calculated from equation (2.3), using  $h = 1$  for  $U_{10} < 19$  m/s and  $h = 0.5H_s$  for higher wind speeds. The water content of the spray  $\frac{dW(z,r)}{dr}$  is then calculated using equation (2.5). If the object is a cylinder, the collision efficiency  $E$  is calculated from equation (2.7). Otherwise, the collision efficiency is assumed to be 1. The total water content of the wind spray is finally calculated from

$$W(z) = \int_{r_{min}}^{r_{max}} E(U, r, D_c) \frac{dW(r, z)}{dr} dr. \quad (3.1)$$

In the present implementation, the native `trapz` function in Matlab is used to perform the numerical integration.

## 3.2 Calculation of wave spray

Note that before the wave spray flux can be calculated, we need to know the position and shape of the bow of the ship. In the model, these are represented by a height above the surface  $H_{bow}$ , together with a set of points in the  $xy$ -plane along the outline of the bow. These are found manually by examining a geometrical model of the vessel. Since the spray jet will only extend a distance towards the aft of the ship given by  $x_e$  (see equation (2.36)), the model will find the position of the spray jet by removing the part of the bow that extends further back than  $x_e$ .

First, the model will solve the differential equations (2.39) and (2.40) describing droplet trajectory and droplet cooling. Equation (2.39) is separated into two equations, one for horizontal and one for vertical movement, and each of the resulting second-order differential equations are transformed into two first-order differential equations. This means that the system, when including equation (2.40), will have a total of 5 first-order differential equations. These are solved using the native Matlab `ode45` solver. Then, the model finds the horizontal distance along the wind direction from the point where wave spray is being calculated to the spray jet. Using the horizontal distance between the point and the spray jet, the model can then use the calculated droplet trajectory to find the height of the intersection point  $z_{int}$ , and thus the water content  $W(z_{int})$  of the intersection point. The wave spray flux is finally calculated by equation (2.41).

## 3.3 Numerical solution of the thermodynamic icing equations

The system of differential equations described by equations (2.47) - (2.49), together with equation (2.46) and the relationship  $S_b = Y/X$ , must be solved numerically. Two different numerical solvers have been implemented in the model. The first solver is based on a two-step Lax-Wendroff method, as suggested by Horjen and Vefsnmo (1987) (Horjen (1990) does not suggest any specific solver). It should be mentioned that the central spatial difference in this method is changed to a backward spatial difference, so that the implementation is no longer identical to the ‘proper’ Lax-Wendroff method. The reason for changing the spatial

difference is explained in the following section. The other solver is based on discretizing the equations only in the spatial direction, and solve the problem as a series of ordinary differential equations, using the solution for one point as input for the point directly below. This is known as the method of lines. In the present implementation of the model, the method of lines is used due to its better stability behaviour than the Lax-Wendroff method. However, the code for using the Lax-Wendroff method has been implemented in the model, even though it is not currently used.

### 3.3.1 Two-step Lax-Wendroff method

Horjen and Vefsnmo (1987) suggest using a two-step Lax-Wendroff method for solving equations (2.47) - (2.48). In this method, the system is represented by a grid extended in space and time. Since we only concern ourselves with movement in the  $z$  direction, the grid will be two-dimensional. Thus,  $X_{i,j}$  and  $Y_{i,j}$  represent the brine and salt content at position  $z_i$  and time  $t_j$ , where  $z_i = z_0 + i\Delta z$  and  $t_j = t_0 + j\Delta t$ . Here,  $z_0$  is the lowest point on the vertical component where the icing is being calculated,  $t_0$  is the starting time of the spray cycle, and  $\Delta z$  and  $\Delta t$  are the numerical step sizes in space and time, respectively. It follows that  $i$  and  $j$  are integers, where

$$\begin{aligned} 0 \leq i \leq N & \quad N = \frac{z_t - z_0}{\Delta z}, \\ 0 \leq j \leq M & \quad M = \frac{t_{end} - t_0}{\Delta t}. \end{aligned}$$

Here,  $t_{end}$  is the end time of the calculations and  $z_t$  is the transition level between dry and wet icing, as described in section 2.5.2. If  $z_t$  lies above the object where icing is being calculated,  $z_t$  is set equal to the highest point of the object. If  $z_t$  lies below the lowest point of the object, dry icing will occur on the entire object and the icing rate can be set equal to the spray flux. The two-step Lax-Wendroff method first estimates  $X$  and  $Y$  at the midpoint between two succeeding time steps by a first order formula:

$$X_{i,j+\frac{1}{2}} = X_{i,j} + \frac{\Delta t}{2} (R_w^{i,j} - I^{i,j}) + \frac{C\Delta t}{4\Delta z} (X_{i+1,j}^3 - X_{i-1,j}^3), \quad (3.2)$$

$$Y_{i,j+\frac{1}{2}} = Y_{i,j} + \frac{\Delta t}{2} (S_w R_w^{i,j} - \sigma S_b^{i,j} I^{i,j}) + \frac{C\Delta t}{4\Delta z} (X_{i+1,j}^2 Y_{i+1,j} - X_{i-1,j}^2 Y_{i-1,j}), \quad (3.3)$$

where

$$\begin{aligned} S_b^{i,j} &= \frac{Y_{i,j}}{X_{i,j}}, \\ I^{i,j} &= I(S_b^{i,j}), \\ C &= 0.264 \frac{g}{\rho_b \mu_b}, \end{aligned}$$

and  $R_w^{i,j}$  is the spray flux at position  $z_i$  and time  $t_j$ . These are then used to calculate the final values:

$$X_{i,j+1} = X_{i,j} + \Delta t \left( R_w^{i,j} - I^{i,j+\frac{1}{2}} \right) - \frac{C\Delta t}{2\Delta z} \left( X_{i+1,j+\frac{1}{2}}^3 - X_{i-1,j+\frac{1}{2}}^3 \right), \quad (3.4)$$

$$Y_{i,j+1} = Y_{i,j} + \Delta t \left( S_w R_w^{i,j} - \sigma S_b^{i,j+\frac{1}{2}} I^{i,j+\frac{1}{2}} \right) - \frac{C\Delta t}{2\Delta z} \left( X_{i+1,j+\frac{1}{2}}^2 Y_{i+1,j+\frac{1}{2}} - X_{i-1,j+\frac{1}{2}}^2 Y_{i-1,j+\frac{1}{2}} \right). \quad (3.5)$$

The boundary conditions are  $X = Y = 0$  for  $i = 0$ ,  $i = N$  and  $j = 0$ . The salinity  $S_b = Y/X$  still has to be specified for  $j = 0$ . By inserting  $X = 0$  into equations (2.43) and (2.44), the following expression for  $S_b$  is derived:

$$S_b = \frac{S_w}{Q/(R_w l_f) + 1}.$$

where  $Q$  is the sum of heat fluxes to the brine, given by equation (2.45). Since  $Q$  depends on  $S_b$ , this expression must be solved numerically, for instance by using the bisection method. In the present implementation, the bisection method is performed with a lower limit of  $S_b^{min} = 0$  ppt, an upper limit of  $S_b^{max} = 300$  ppt, and an error tolerance of  $10^{-3}$  ppt.

Unfortunately, using the boundary condition  $X = 0$  for  $i = 0$  as suggested, implies that there will be no runoff from the lowest point of the vertical plate. This is an unrealistic assumption that causes a large build-up of water at the lowest point of the surface, which eventually will disturb the numerical solution of the rest of the surface as well. To remedy this, the central spatial difference in the Lax-Wendroff method is changed to a backward spatial difference in our model. This means that the solution at  $z = i$  only depends on the solution at  $z = i + 1$  and is independent of the solution at  $z = i - 1$ , making the boundary condition for  $i = 0$  unnecessary. This changes equations (3.2) and (3.3) to

$$X_{i,j+\frac{1}{2}} = X_{i,j} + \frac{\Delta t}{2} (R_w^{i,j} - I^{i,j}) + \frac{C\Delta t}{2\Delta z} (X_{i+1,j}^3 - X_{i,j}^3), \quad (3.6)$$

$$Y_{i,j+\frac{1}{2}} = Y_{i,j} + \frac{\Delta t}{2} (S_w R_w^{i,j} - \sigma S_b^{i,j} I^{i,j}) + \frac{C\Delta t}{2\Delta z} (X_{i+1,j}^2 Y_{i+1,j} - X_{i,j}^2 Y_{i,j}), \quad (3.7)$$

and changes equations (3.4) and (3.5) to

$$X_{i,j+1} = X_{i,j} + \Delta t \left( R_w^{i,j} - I^{i,j+\frac{1}{2}} \right) - \frac{C\Delta t}{\Delta z} \left( X_{i+1,j+\frac{1}{2}}^3 - X_{i,j+\frac{1}{2}}^3 \right), \quad (3.8)$$

$$Y_{i,j+1} = Y_{i,j} + \Delta t \left( S_w R_w^{i,j} - \sigma S_b^{i,j+\frac{1}{2}} I^{i,j+\frac{1}{2}} \right) - \frac{C\Delta t}{\Delta z} \left( X_{i+1,j+\frac{1}{2}}^2 Y_{i+1,j+\frac{1}{2}} - X_{i,j+\frac{1}{2}}^2 Y_{i,j+\frac{1}{2}} \right). \quad (3.9)$$

The change from central to backward spatial difference is at the cost of some accuracy. It also has to be assumed that the amount of runoff from a point on the vertical plate is completely independent of what lies below the point. The method (with backward spatial difference) is illustrated in figure 3.1.

This solution method is relatively fast, but often becomes unstable when the spray flux is low and weather conditions are too mild for dry icing to occur. Introducing a small but non-zero value of  $X$  for  $j = 0$  helps reduce this problem, but does not eliminate it completely. Stability can be achieved by sufficiently reducing the time steps, but this will also slow down the calculations. A different and far more stable solution method is therefore described in the following section.

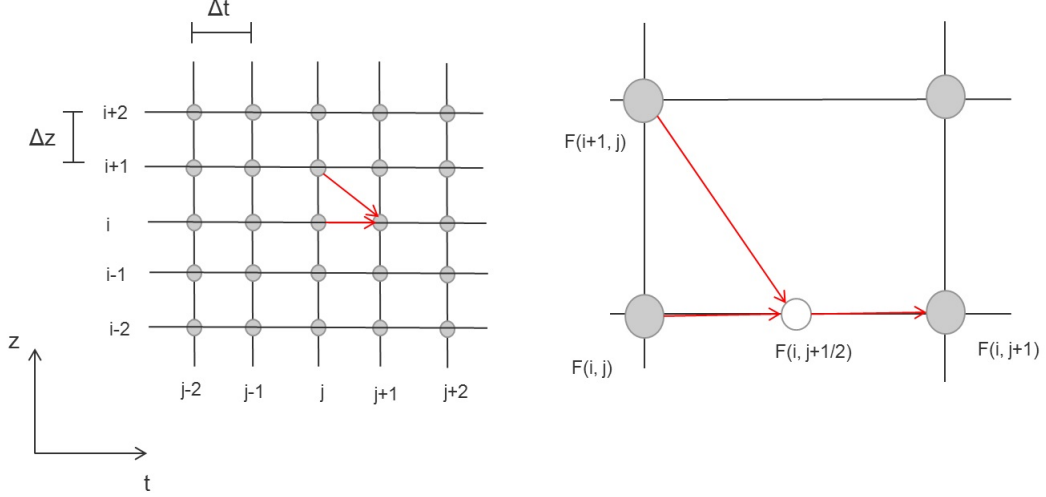


Figure 3.1: Illustration of the modified Lax-Wendroff method. To the left, the grid in the  $zt$ -plane used in the method is shown. In order to find the solution at  $i, j + 1$ , the solutions at  $i + 1, j$  and  $i, j$  are used. To the right, it is illustrated that the method will first make a half-step in the time direction and find the (first-order) solution at  $i, j + 1/2$ , and use this solution to find the final solution at  $i, j + 1$ .

### 3.3.2 Method of lines

By adopting a backward spatial difference rather than a central, one may observe that the time-dependent solution for each point only depends on the time-dependent runoff for the point directly above. In other words, if the time-dependent solution of a point is known, the time-dependent solution of the point directly below can be solved as an ordinary differential equation (ODE). This can be represented mathematically by rewriting equations (2.47) and (2.48):

$$\frac{\partial X_i}{\partial t} = R_w^i(t) - I \left( \frac{Y_i}{X_i}, t \right) + \frac{C}{\Delta z} (X_{i+1}(t)^3 - X_i^3), \quad (3.10)$$

$$\frac{\partial Y_i}{\partial t} = S_w R_w^i(t) - \sigma \frac{Y_i}{X_i} I \left( \frac{Y_i}{X_i}, t \right) + \frac{C}{\Delta z} (X_{i+1}(t)^2 Y_{i+1}(t) - X_i^2 Y_i), \quad (3.11)$$

where  $X_i$  and  $Y_i$  are the amounts of salt and brine at point  $z_i$ , and  $R_w^i(t)$  is the (time dependent) spray flux to  $z_i$ . Since all the time dependent functions are known, this means we can solve these ODEs for each  $z_i$ , starting at  $z = z_t$ . Since  $z_t$  does not receive any runoff, we will use the initial condition that  $X_{N+1} = Y_{N+1} = 0$ . Solving the system as a series of ODEs is advantageous because we can use solvers that automatically regulate the time step size to maintain accuracy and stability. In other words, the solution will almost always be stable while still performing at a reasonable speed. However, the method will generally be slower than the Lax-Wendroff method. The method is illustrated in figure 3.2. In the present model, the native Matlab `ode23s` solver is used to solve the ODEs.

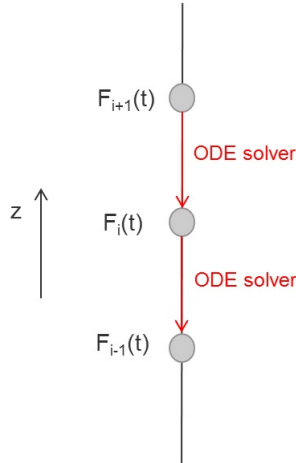


Figure 3.2: Illustration of the method of lines used in the model. In this method, the problem is only discretized in the  $z$  direction. When solving at point  $i$ , the time-dependent solution at  $i + 1$  is used as input, and the problem is solved as an ODE in time, using a regular ODE solver. This solution is then used as input for the ODE at point  $i - 1$ , and so on.

## 3.4 Total icing on a given vessel

The methods described so far in the thesis can be used to calculate the icing on individual points or objects on a vessel. However, in many cases it is useful to calculate the icing rate on the entire vessel, in order to determine the spatial distribution of ice and the total ice load. In theory, one could divide the vessel into many individual objects and calculate the icing on each one, but this would require large amounts of manual work, especially if using a highly detailed model of the vessel. Therefore, a largely automatized method of calculating icing rates on an entire vessel has been developed for this thesis, using a standard polygon-based vessel geometry. This geometry requires algorithms for dealing with brine runoff as well as polygons being shielded from spray by other polygons. These algorithms will be described in this section.

### 3.4.1 Geometry

In order to calculate the icing on all parts of a vessel, a representation of the vessel geometry is required. As is standard for computer representations of three-dimensional objects, the vessels are made up of a number of polygons in three-dimensional space. In the present thesis, all polygons that make up the geometries will be triangles, in order to ensure that each polygon has a well-defined orientation. Specifically, the geometry consists of a large number of nodes, and each polygon is defined by listing the three nodes that define the edges of the polygon. The difference between polygons and nodes is illustrated in figure 3.3. The polygons also define the grid resolution for the icing calculations, since the icing rate will be calculated individually on each polygon. The vessel geometries that are analysed in the thesis typically consist of tens of thousands or hundreds of thousands of polygons, see figure 3.4 for an example.

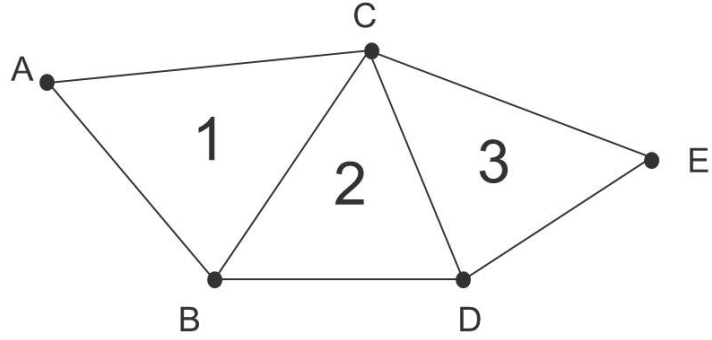


Figure 3.3: Illustration of nodes (letters) and polygons (numbers). Each node is defined by its coordinates in 3D-space (although the illustration is in 2D). Each polygon is defined by associating it with three nodes. For instance, polygon 2 is defined by being associated with node B, C and D.

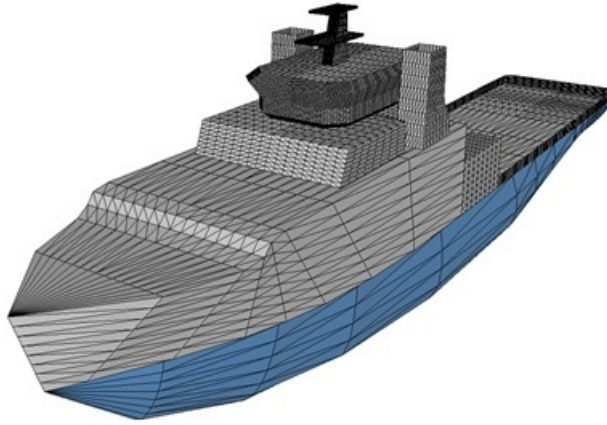


Figure 3.4: Vessel geometry for the offshore supply vessel Geofjord, consisting of approximately 17000 polygons. Some of the other vessel geometries consist of hundreds of thousands of polygons, although most of the polygons are spent on smaller objects like rails or equipment.

### 3.4.2 Total spray flux to a polygon

The spray flux to each polygon is calculated using the methods described in sections 3.1 - 3.2. Specifically, the centroid of the polygon is used as a basis for the calculations - the wind spray flux depends on the centroid's height above the surface, and the wave spray flux depends on the height where a droplet trajectory from the centroid hits the spray jet. The orientation of the polygon is also taken into consideration. In addition, the polygons may be shielded from spray by other polygons. This is represented by a shielding factor  $\zeta$ , which is a number between 0 (no shielding) and 1 (polygon is fully shielded, and will receive no spray). The shielding is calculated individually for wave and wind spray, and is described in detail in section 3.4.3. The expression for the total spray flux  $R_w$  [ $\frac{\text{kg}}{\text{m}^2\text{s}}$ ] to a polygon during

a spray event becomes

$$R_w = R_{wind} + R_{wave}, \quad t < \tau_s, \quad (3.12)$$

where  $\tau_s$  is the duration of the spray event, calculated from (2.37).  $R_{wind}$  is the flux from wind spray given by

$$R_{wind} = W(z_c) |\mathbf{U}(z_c) \cdot \mathbf{n}| (1 - \zeta_{wind}), \quad (3.13)$$

where  $W(z_c)$  is the water content of wind generated spray from equation (3.1) at the height  $z_c$  above surface level of the centroid,  $\mathbf{U}$  is the wind speed at the same height,  $\mathbf{n}$  is a vector of unit length normal to the polygon, and  $\zeta_{wind}$  is the shielding factor of wind spray to the polygon. Similarly, the wave spray  $R_{wave}$  is given by

$$R_{wave} = w(z_{int}) |\mathbf{v}_d \cdot \mathbf{n}| (1 - \zeta_{wave}), \quad (3.14)$$

where  $z_{int}$  is the height above the bow of the intersection point between the droplet path from the centroid of the polygon and the spray jet,  $w(z_{int})$  is the water content at this height given by equation (2.35),  $\mathbf{v}_d$  is the droplet velocity when the droplet hits the centroid and  $\zeta_{wave}$  is the wave shielding factor of the polygon.

The temperature of the spray flux is assumed to be the average temperature of incoming wind and wave spray. The temperature of the wave spray  $T_{wave}$  is calculated from solving equation (2.40), as described in section 3.2. As for the wind spray, it is assumed that the droplets are small enough to quickly be supercooled down to the air temperature  $T_a$ . This assumption will be discussed in section 5.4.3. Thus, the weighted spray temperature as the spray impinges on a boat during a spray event is

$$T_w = \frac{R_{wave} T_{wave} + R_{wind} T_a}{R_w}, \quad t < \tau_s \quad (3.15)$$

Inbetween spray events, only the wind spray remains, so that

$$R_w = R_{wind}, \quad \tau_s < t < \tau_p, \quad (3.16)$$

$$T_w = T_a, \quad \tau_s < t < \tau_p, \quad (3.17)$$

where  $\tau_p$  is the period between spray events given by equation (2.38).

### 3.4.3 Shielding

In short, the shielding algorithm will project each polygon along the droplet trajectory onto the plane where the spray is assumed to originate, and will find the intersection between the polygon and the union of all previously projected polygons. This is done slightly differently for wind spray and wave spray (thus the two separate shielding factors), but the basic principle is the same.

For wind spray, since the small droplets are assumed to travel approximately horizontally, the polygons are simply projected along a horizontal direction onto a plane normal to the wind direction. Specifically, it is actually the position of the nodes that are projected onto this plane. If the position of a node is given by  $x$ ,  $y$  and  $z$ , and the node position after being

projected onto the spray plane is given by  $x_s$  and  $z_s$  (the horizontal and vertical position on the plane, respectively), the projection can be done by

$$\begin{aligned}x_s &= y \cos \alpha - x \sin \alpha, \\z_s &= z.\end{aligned}$$

Another vital piece of information when calculating the shielding is the order of which the polygons are projected onto this plane, since the method finds the intersection between the polygon and all previously projected polygons. Essentially, the polygons that are first hit by spray must be the first polygons to be projected. As of yet, no method has been found that will determine the order of which the polygons will be projected (hereby called ‘shielding order’) correctly for all possible orientations of polygons relative to one another. Instead, a simple but largely correct method is used in the model. For wind spray, the shielding order is simply based on the horizontal position of the polygon centroid relative to the wind direction. In other word, the distance

$$L_{sort} = y_c \sin \alpha + x_c \cos \alpha,$$

where  $y_c$  and  $x_c$  are the  $x$  and  $y$  coordinates of the centroid of the polygon. The polygons with the highest  $L_{sort}$  are projected first.

For the larger droplets in wave spray, the simple assumption that droplets will travel horizontally is no longer valid, and the method of projecting nodes and finding the shielding order changes accordingly. The nodes are now projected along their respective droplet trajectories. Mathematically, this means the node coordinates in the shielding plane  $x_s$  and  $z_s$  are now given by

$$x_s = y \cos \alpha - x \sin \alpha, \tag{3.18}$$

$$z_s = z_{int}, \tag{3.19}$$

where  $z_{int}$  is the height of the intersection point between the droplet path and the spray jet. The  $x_s$  coordinate remains unchanged from the wind spray case, since the spray is still assumed to be travelling along the wind direction. One may notice that this is not literally the projection onto the actual wave spray jet (which follows the bow of the ship). In fact, equations (3.18) - (3.19) describe a situation where the nodes are first projected onto the wave spray jet, and then projected horizontally onto a plane normal to the wind direction with the same origin as the original  $x, y, z$  coordinate system. This will generally not cause any problems, but one instance where it *does* cause some strange results for the shielding is discussed in section 5.3. The shielding order also becomes more complicated for the wave spray shielding, since the vertical position of the polygons now will be relevant. Once again, we use a simple method that will give mostly correct results. It is assumed that the angle of the droplet velocity (i.e. the angle defined by  $\arctan(v_{dv}/v_{dh})$ , where  $v_{dv}$  and  $v_{dh}$  are the vertical and horizontal component of the droplet velocity) will quickly reach a constant value. This value can be called  $\beta$ , and can be easily found from the solution of equation (2.39). The shielding order will now depend on the position of the polygon centroid along the direction described by  $\alpha$  and  $\beta$ . Mathematically, we may define a length

$$L_{sort} = \cos \beta (x_c \cos \alpha + y_c \sin \alpha) + z_c \sin \beta,$$

and the shielding order is defined by this length, where the polygons with the highest  $L_{sort}$  are projected first.

Once the projected nodes and the shielding order are found, the method of finding the shielding factors is identical for both wind and wave spray. It is an iterative process, where each polygon  $p_i$  is compared with the union of all previously projected polygons, which will be called  $\Psi_i$ . The shielding factor  $\zeta_i$  for polygon  $p_i$  is given by the area of the intersection between  $p_i$  and  $\Psi_i$ , divided by the area of the polygon. Mathematically, this can be described as

$$\zeta_i = A(p_i \cap \Psi_i) / A(p_i),$$

$$\Psi_{i+1} = p_i \cup \Psi_i,$$

where  $A(p)$  is the area of polygon  $p$ . The process is illustrated in figure 3.5. Notice that  $\Psi_i$  may contain holes, or consist of several disjoint polygons. Thus, the function that finds the union and intersection must be able to deal with such polygons. The model currently uses the ‘Polygon Clipper’ function for this purpose (Hölz, 2006). As an example of how the results from the shielding algorithm looks, figure 3.6 shows the wave spray shielding fraction for the Geofjord vessel for wind speed  $U_{10} = 20$  m/s and angle between vessel heading and wind speed  $\alpha = 20^\circ$  (vessel is stationary). Figure 3.7 shows the wave spray shielding fraction for AMI for the same case ( $U_{10} = 20$  m/s,  $\alpha = 20^\circ$ ).

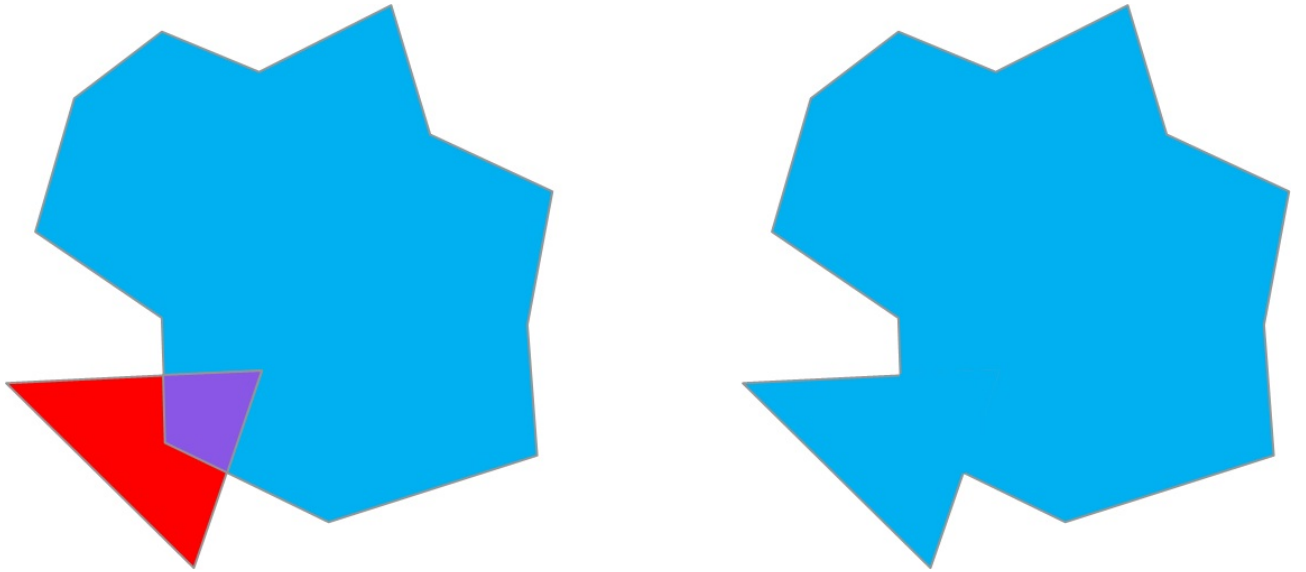


Figure 3.5: Illustration of shielding algorithm. To the left, a polygon (red) is projected upon the shielding plane and compared with the union of all previously projected polygons (blue). The intersection between the two is marked in purple. The shielding fraction for the polygon equals the area of the intersection divided by the area of the projected polygon. After the shielding fraction is calculated, the algorithm finds the union between the polygon and the previously projected polygons (blue, to the right), which is what the next polygon will be compared with.

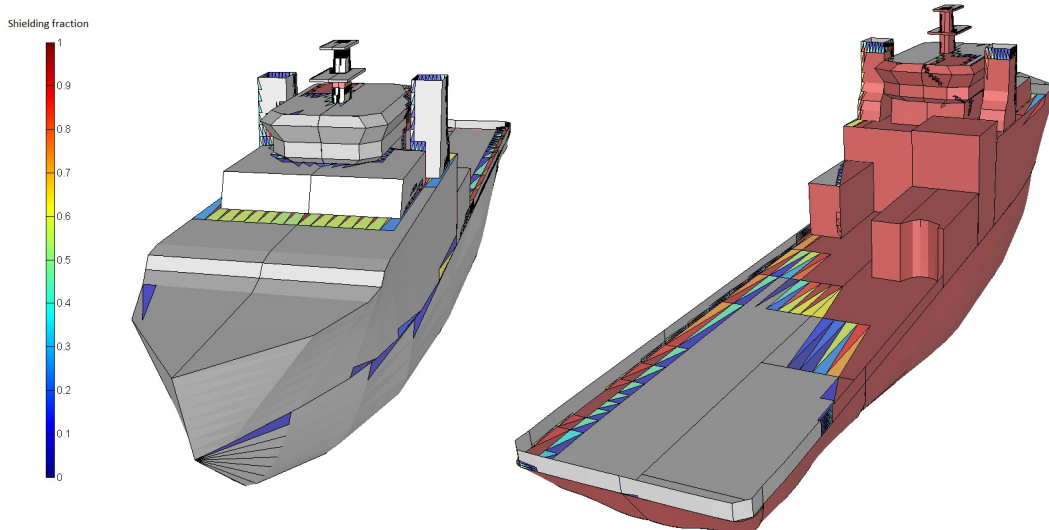


Figure 3.6: Wave spray shielding factor for Geofjord for the case  $U_{10} = 20$  m/s,  $\alpha = 20^\circ$ . Grey polygons are completely unshielded.

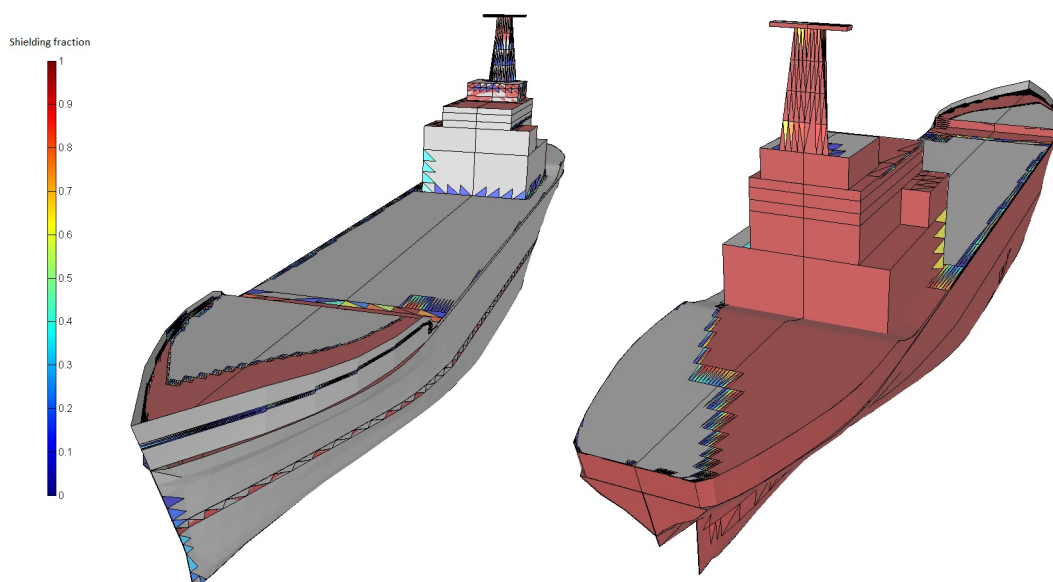


Figure 3.7: Wave spray shielding factor for the weather ship AMI (the geometric representation is to scale, but not completely accurate) for the case  $U_{10} = 20$  m/s,  $\alpha = 20^\circ$ . Grey polygons are completely unshielded.

### 3.4.4 Runoff

Since equations (2.47) - (2.48) take into account that unfrozen brine will flow downwards, an algorithm for finding which polygons each polygon will give runoff to is required. The algorithm will first cycle through each polygon and check the orientation. If the polygon is horizontal or very close to horizontal, no runoff calculations are performed. If not, all

coordinates of the polygon are transformed to a plane with the same orientation as the polygon. If the three nodes of the polygon are positioned at points  $\mathbf{r}_1$ ,  $\mathbf{r}_2$ ,  $\mathbf{r}_3$  (it does not matter which node is 1, 2 or 3) in the standard  $x$ ,  $y$ ,  $z$  coordinate system (defined in section 2.1), and the new coordinate system is notated by  $x_p$  and  $z_p$ , the transformation is done as follows: We define the following vectors

$$\mathbf{r}_{12} = \mathbf{r}_2 - \mathbf{r}_1, \quad (3.20)$$

$$\mathbf{r}_{13} = \mathbf{r}_3 - \mathbf{r}_1, \quad (3.21)$$

$$\mathbf{r}_{23} = \mathbf{r}_3 - \mathbf{r}_2, \quad (3.22)$$

along with a unit vector in the new  $x_p$  direction

$$\hat{x}_p = \frac{\hat{z} \times \mathbf{n}}{|\hat{z} \times \mathbf{n}|}, \quad (3.23)$$

and a unit vector in the new  $z_p$  direction

$$\hat{z}_p = \frac{\hat{x}_p \times \mathbf{n}}{|\hat{x}_p \times \mathbf{n}|}, \quad (3.24)$$

where  $\mathbf{n}$  is the normal vector to the polygon and  $\hat{z}$  is the unit vector of  $z$  in the ordinary coordinate system. The vectors  $\mathbf{r}_{12}$  and  $\mathbf{r}_{13}$  are transformed into

$$\mathbf{r}_{p12} = [\mathbf{r}_{12} \cdot \hat{x}_p, \mathbf{r}_{12} \cdot \hat{z}_p],$$

$$\mathbf{r}_{p13} = [\mathbf{r}_{13} \cdot \hat{x}_p, \mathbf{r}_{13} \cdot \hat{z}_p],$$

and finally, the position of the three nodes in the new coordinate system are

$$\mathbf{r}_{p1} = [0, 0],$$

$$\mathbf{r}_{p2} = \mathbf{r}_{p12},$$

$$\mathbf{r}_{p3} = \mathbf{r}_{p13}.$$

After the transformation, the algorithm for determining which polygons that receive the runoff is as such:

- First, find the node with the lowest  $z_p$ . We may call this node  $A$ .
- Second, find the node that  $A$  has the lowest inclination to. This node may be called  $B$ .
- If neither  $A$  or  $B$  is the central node (the node that neither has the highest nor the lowest  $x_p$  value), the polygon will give all its runoff over the  $AB$  side of the polygon.
- If  $A$  is the central node, the polygon will give runoff over the  $AB$  and  $AC$  sides. It is assumed the relative amount of runoff over each side equals the relative area of the polygon on each side of  $A$ .

- If  $B$  is the central node, the polygon will give runoff over the  $AB$  and  $BC$  sides. It is assumed the relative amount of runoff over each side equals the relative area of the polygon on each side of  $B$ .

This process is illustrated in figure 3.8. Once we have found which side or sides the polygon will give runoff over, it is merely a matter of finding which polygon or polygons that share the nodes that the sides consist of. For instance, if a polygon gives runoff over the  $AB$  and  $AC$  sides, and the relative area on each side of  $A$  is 0.4 and 0.6 respectively, it is assumed that the polygon that shares the  $A$  and  $B$  nodes will receive 40% of the runoff, while the polygon that shares the  $A$  and  $C$  nodes will receive 60%.

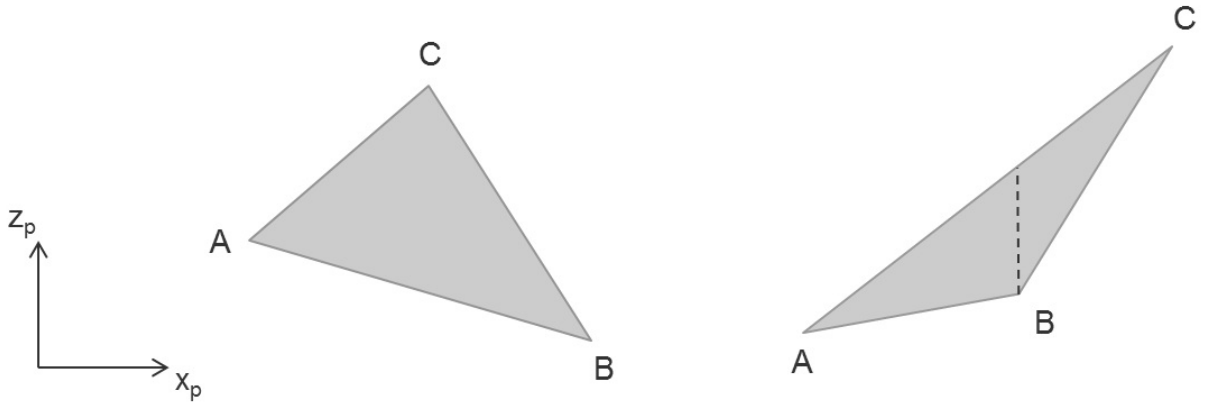


Figure 3.8: Illustration of the algorithm for finding which polygons each polygon will give runoff to. For the polygon to the left, the algorithm will first find the lowest node ( $B$ ). Then, it will find the node that  $B$  has the lowest inclination to ( $A$ ). Since neither  $B$  nor  $A$  is the central node (i.e. central in the  $x_p$  direction), the polygon will give all runoff over the  $AB$  side. For the polygon to the right, the algorithm first finds the lowest polygon ( $A$ ) and the polygon that it has the lowest inclination to ( $B$ ). Since  $B$  is the central node, the polygon will give runoff over both the  $AB$  and  $BC$  side. The relative runoff over each side equals the relative area on each side of  $B$ , i.e. the area on each side of the stippled line divided by the total area of the polygon.

### 3.4.5 Icing calculations

The icing rate will be calculated by solving the set of differential equations described by equations (3.10) - (3.11) for each polygon. However, since the theoretical background as described in section 2.5 is only valid for vertical geometries, additional assumptions must be made for polygons that have an inclined or horizontal orientation. In the current model, it is assumed that the orientation of polygons only affects the brine velocity, and that the brine velocity will be adjusted by simply decomposing the gravitational force. This assumption will be further discussed in section 5.8. This means equation (2.49) is adjusted to

$$v_b = -0.264 \frac{g}{\rho_b \mu_b} X^2 |\sin \theta|,$$

where  $\theta$  is the angle between vertical direction and the normal vector of the polygon, i.e.

$$\theta = \arccos(\hat{z} \cdot \mathbf{n}).$$

One may use the trigonometric relationship of  $\sin^2 \theta + \cos^2 \theta = 1$  to write

$$v_b = -0.264 \frac{g}{\rho_b \mu_b} X^2 \sqrt{1 - (\hat{z} \cdot \mathbf{n})^2}. \quad (3.25)$$

This equation goes to zero for horizontally oriented polygons, implying that no water runs off horizontal polygons, which is not a realistic implication. The waves will cause constant rolling and pitching of the vessel, and even on horizontal parts of the ship the water will move around, eventually moving off the ship. There are no good methods of accounting for this in the present model. But in order to prevent the unrealistic case that the water will remain on the polygon for the entire spray duration, a minimum value of  $v_b$  is enforced in the model. Currently, the expression for  $v_b$  in the model is

$$v_b = -0.264 \frac{g}{\rho_b \mu_b} X^2 \min[\sin \theta, 0.2], \quad (3.26)$$

essentially setting 0.2 as a lower limit for  $\sin \theta$ . This, and alternative methods of treating geometries, are further discussed in section 5.8.

Also, because a polygon can receive runoff from a polygon with a different orientation (and therefore a different brine velocity), equations (3.10) - (3.11) must be modified. If not, it would be possible for a polygon to receive more or less runoff than the polygon above actually gives off. Therefore, instead of using the water and salt content of the above polygon ( $X_{i+1}$  and  $Y_{i+1}$ ) as inputs, the actual water flux and salt flux from that polygon will be used instead. These will be called  $R_{ro}$  and  $S_{ro}$  respectively, and are defined as the water content or salt content of a polygon multiplied by the brine velocity on the same polygon.

$$R_{ro} = -0.264 \frac{g}{\rho_b \mu_b} X^2 |\sin \theta| \cdot X,$$

$$S_{ro} = -0.264 \frac{g}{\rho_b \mu_b} X^2 |\sin \theta| \cdot Y.$$

These are not actually fluxes, since they have dimension  $\text{kg}/(\text{ms})$  rather than  $\text{kg}/(\text{m}^2\text{s})$ . Notice that the minimum value of 0.2 for  $\sin \theta$  is not enforced in these equations. This means that, for horizontal or nearly horizontal polygons (where  $\sin \theta < 0.2$ ), there will be a certain amount of brine that will run off the polygon but not run to any other polygon - i.e. it will disappear from the system. This is discussed in more detail in section 5.8. Equations (3.10) - (3.11) are then modified to

$$\frac{\partial X}{\partial t} = R_w(t) - I \left( \frac{Y}{X}, T_w(t) \right) + \frac{1}{\Delta z} (R_{ro}^{over}(t) - CX^3), \quad (3.27)$$

$$\frac{\partial Y}{\partial t} = S_w R_w(t) - \sigma \frac{Y}{X} I \left( \frac{Y}{X}, T_w(t) \right) + \frac{1}{\Delta z} (S_{ro}^{over}(t) - CX^2Y), \quad (3.28)$$

where  $C$  here equals

$$C = 0.264 \frac{g}{\rho_b \mu_b} \sin \theta,$$

and  $R_{ro}^{over}(t)$  and  $S_{ro}^{over}(t)$  are the sums of runoff water and salt flux to the polygon. It is not obvious what  $\Delta z$  is in this case, since our system consists of triangles rather than evenly spaced points. It will be assumed that  $\Delta z$  is the average length of the polygon in the  $z_p$  direction in a coordinate system in the polygon plane. This length can be calculated from

$$\Delta z = \frac{A(p)}{\max[|\mathbf{r}_{12} \cdot \hat{x}_p|, |\mathbf{r}_{13} \cdot \hat{x}_p|, |\mathbf{r}_{23} \cdot \hat{x}_p|]},$$

where  $A(p)$  is the area of the polygon,  $\hat{x}_p$  is given by equation (3.23) and  $\mathbf{r}_{12}$ ,  $\mathbf{r}_{13}$ ,  $\mathbf{r}_{23}$  are given by equations (3.20) - (3.22).

All the tools required to calculate the icing on a complete vessel have now been described. Since runoff water and salt flux are required inputs, the polygons that have the highest elevation (i.e. the highest  $z$  value of the centroid) will be solved first. It is assumed polygons below sea surface level will have no icing. The equations will be solved on each polygon for a single spray cycle, and it will be assumed that all remaining surface brine after a spray cycle will disappear before the next cycle starts. Still, the initial conditions of the differential equations will assume a small water layer (currently  $10^{-4}$  kg/m<sup>2</sup> with salinity  $S_w$ ) is present before the calculations of the spray cycle starts - this is done simply to improve the stability of the calculations. The icing calculation process may be summarized as follows:

1. Find which polygons each polygon receives runoff from, and the relative amounts, using the process described in section 3.4.4. This depends only on the vessel geometry, and needs only be done once for each vessel.
2. Find  $R_w(t)$  and  $T_w(t)$  for each polygon, using equations (3.12) - (3.17).
3. Starting with the polygons furthest from the sea surface, find  $X(t)$  and  $Y(t)$  using equations (3.27) - (3.28). Using these results, find and store the results for  $I(t)$ ,  $R_{ro}(t)$  and  $S_{ro}(t)$ . The results for  $R_{ro}(t)$  and  $S_{ro}(t)$  are needed for calculations on polygons further below.
4. Find the average  $I(t)$  over the entire spray cycle, for each polygon. This is assumed to be the average icing rate for the given set of weather conditions.

For a more intuitive representation of the icing rate, one may transform  $I \left[ \frac{\text{kg}}{\text{m}^2\text{s}} \right]$  to  $I \left[ \frac{\text{mm}}{\text{h}} \right]$  by the formula

$$I \left[ \frac{\text{mm}}{\text{h}} \right] = \frac{3600 \cdot 1000 \cdot I \left[ \frac{\text{kg}}{\text{m}^2\text{s}} \right]}{\rho_i}, \quad (3.29)$$

where  $\rho_i$  is the accretion density. Also, as a simplification, the brine density  $\rho_b$ , brine dynamic viscosity  $\mu_b$  and brine heat capacity  $c_b$  are in the current implementation of the model assumed to be equal to the density, dynamic viscosity and heat capacity of sea water ( $\rho_w, \mu_w, c_w$ ).



# Chapter 4

## Results

### 4.1 Comparison with Jones and Andreas (2012)

In order to test if the wind spray model described in Jones and Andreas (2012) has been implemented correctly, the present model has been applied to the cases described in that paper in order to reproduce some of the results.

#### 4.1.1 Ocean Bounty

In order to test the model, Jones and Andreas (2012) calculate the icing on the semi-submersible drilling rig Ocean Bounty, which was exposed to strong icing conditions in Cook Inlet, Alaska, during the winter of 1979-1980. More information on the icing events of Ocean Bounty can be found in Nauman (1984). The crew registered weather and temperature data 9 times a day, in addition to a rough estimate of the icing rate. It is unknown where and how the icing rate was measured. The wind measurements were done at 84 meters above the sea surface. The data from Ocean Bounty is available in Jones and Andreas (2009).

Jones and Andreas (2012) compare the observed icing rate with the calculated icing rate from their model. The icing is calculated on a reference cylinder with a diameter of 5 cm at 20 meters above the ocean surface.

#### 4.1.2 Icing rate

Figure 4.1 shows the icing rate of Ocean Bounty during the winter of 1979-1980, as calculated by the present model. One can observe that, even though the shape of the curve agrees fairly well with that of the corresponding graph in Jones and Andreas (2012) (figure 10(d) in that paper), the level does not. The calculated icing rate from our model is consistently slightly above half of the icing rate in the paper.

Jones and Andreas (2012) mention that, when calculating icing rates for Ocean Bounty, whenever observed values for  $H_s$  were unavailable they would use an algorithm described by Andreas and Wang (2007) to estimate  $H_s$  instead. However, because this algorithm would significantly overestimate  $H_s$  for Ocean Bounty, Jones and Andreas (2012) would adjust  $H_s$  down by multiplying with a factor 0.32. It was noticed that if the value of  $H_s$  resulting from

the Andreas and Wang (2007) algorithm was used as input to the calculations, even when observed values of  $H_s$  were available, and *without* multiplying the estimated  $H_s$  with the factor 0.32, the resulting estimated icing rates (figure 4.2) were almost identical to the icing rates for Ocean Bounty in Jones and Andreas (2012). Figure 4.3 shows the estimated icing rate from our implementation when using  $H_s$  from the Andreas and Wang (2007) algorithm (red), plotted on top of the results from Jones and Andreas (2012) (black). Kathleen F. Jones (personal communication) confirmed that the  $H_s$  from the Andreas and Wang (2007) algorithm (without multiplying with the factor 0.32) had indeed been used when making the graph of estimated icing rates for Ocean Bounty.

### 4.1.3 Further comparison with Jones and Andreas (2012)

In order to test the implementation of the wind spray model described in Jones and Andreas (2012), a number of graphs in the paper were successfully reproduced by the Matlab implementation. However, the graph for droplet concentration functions for high wind speeds (figure 4(b) in Jones and Andreas (2012)) shows results that are different from our implementation of the model. In figure 4.4, the resulting concentration functions from our implementation (red) are plotted on top of the figure from the paper (black). It was discovered that, if one used a wind speed dependency of  $U_{10}^5$  rather than  $30U_{10}^4$  in the expression for the concentration function (equation (2.2)), the graph from the paper was reproduced accurately. This is shown in figure 4.5, where the concentration function from the implementation when using the  $U_{10}^5$  rather than  $30U_{10}^4$  (red) is plotted on top of the graph from the paper (black). Kathleen F. Jones (personal communication) confirmed that figure 4(b) in Jones and Andreas (2012) had been plotted using a wind speed dependency of  $U_{10}^5$  rather than  $30U_{10}^4$ .

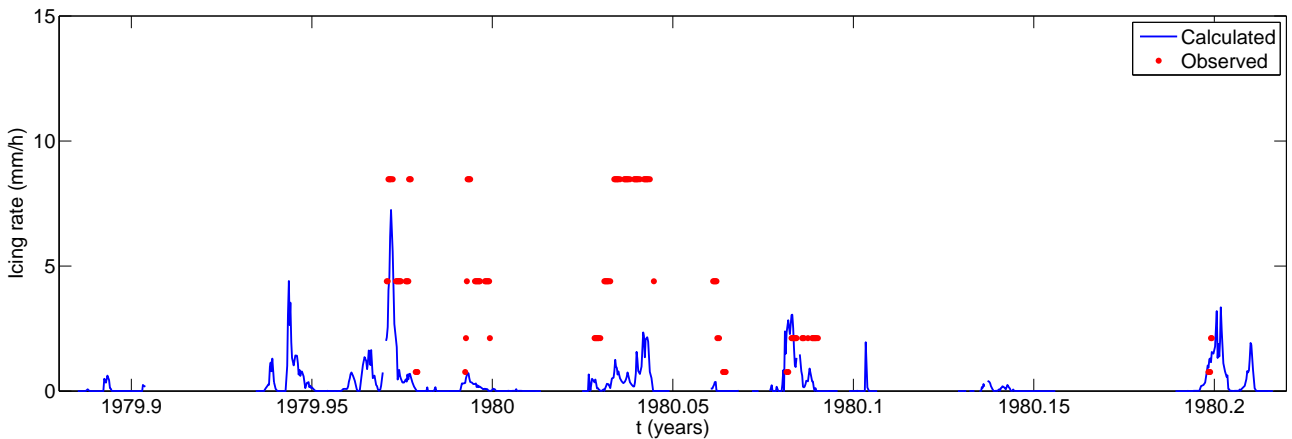


Figure 4.1: Icing rate for Ocean Bounty, using the measured  $H_s$ . The red dots are observations of approximate icing rates.

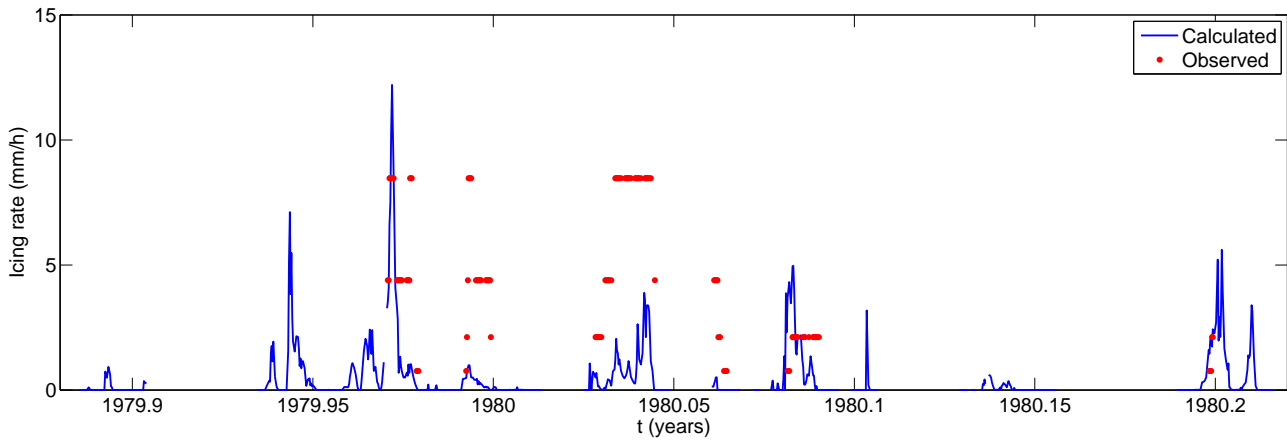


Figure 4.2: Icing rate for Ocean Bounty, using the  $H_s$  calculated from the Andreas and Wang (2007) algorithm without the factor of 0.32. The red dots are observations of approximate icing rates.

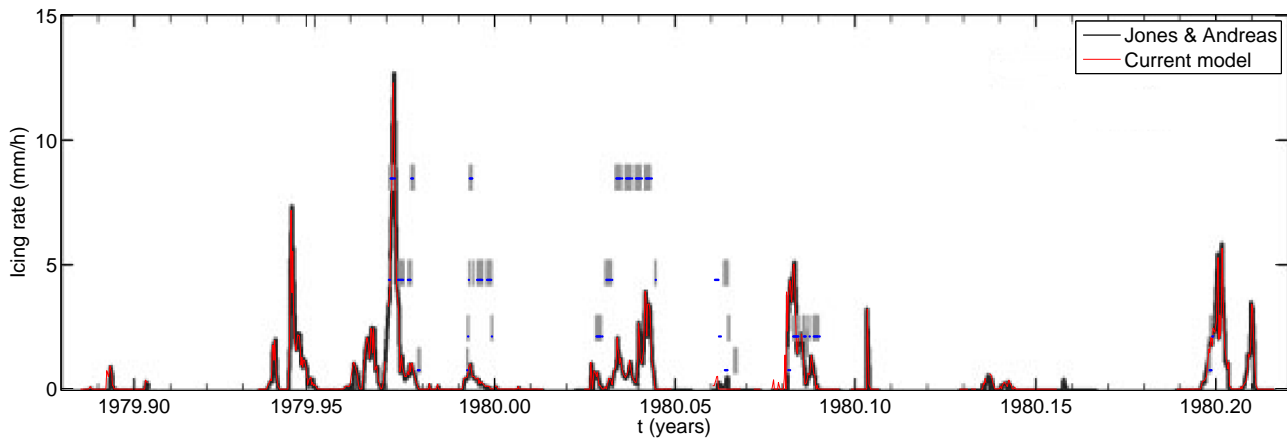


Figure 4.3: Icing rate for Ocean Bounty from the present model (red), using the  $H_s$  calculated from the Andreas and Wang (2007) algorithm without the factor of 0.32, plotted over the icing rate from figure 10(b) in Jones and Andreas (2012) (black).

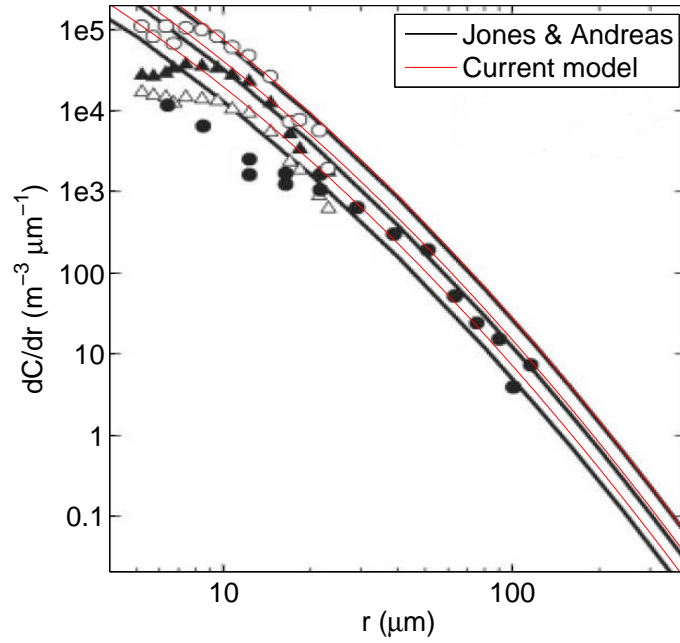


Figure 4.4: Estimated concentration distribution, using wind speed dependency  $30U_{10}^4$ , for  $U_{10} = 20$  m/s (lower line),  $U_{10} = 24$  m/s (middle line) and  $U_{10} = 28$  m/s (upper line), plotted over figure 4(b) from Jones and Andreas (2012).

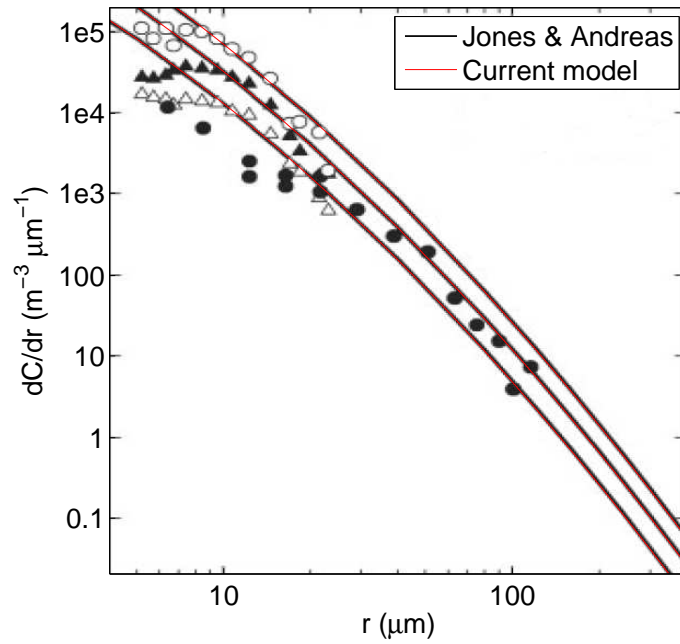


Figure 4.5: Estimated concentration distribution, using wind speed dependency  $U_{10}^5$ , for  $U_{10} = 20$  m/s (lower line),  $U_{10} = 24$  m/s (middle line) and  $U_{10} = 28$  m/s (upper line), plotted over figure 4(b) from Jones and Andreas (2012).

## 4.2 Estimated icing rates on Norne, Skrugard and Shtokman

The present icing model has been applied to the hindcast data available at the undeveloped Skrugard and Shtokman fields. These results have been compared to the estimated icing rates at the Norne field, in order to determine whether icing will be a significantly greater problem in the Barents Sea than in the Norwegian Sea. Even though meteorological data are available for Norne, hindcast Nora10 data will still be used for this location in order to compare the estimated icing rates without the difference between estimated and measured meteorological data (which will be discussed in section 5.7) being a variable. The icing rates will be estimated for an exposed part on a FPSO. The Norne FPSO will be used as a reference for finding the shape of the bow as well as how high above the ocean surface the bow is positioned. From the available geometry for the Norne vessel, the bow is assumed to be positioned 15 m above the sea surface. Since sea surface temperatures are not listed in the Nora10 hindcast data, the monthly average surface temperatures at the three locations (Locarnini et al., 2010) have been used instead. Also, there are periods where some of the hindcast data for Shtokman is unavailable, making icing calculations impossible. These periods are marked by grey in the time series plots for Shtokman.

### 4.2.1 Icing purely from wind spray

Figure 4.6 shows the resulting estimated icing rates for pure wind icing - i.e. all spray flux due to wave spray is neglected. It has also been assumed that the water flux is low enough for all the impinging water to freeze, so that the icing rates are calculated from equation (2.6). The icing rates are calculated for a point on a vertical surface that lies at a height of 15.7 meters above sea level. The collision factor is assumed to be unity. The estimated wind icing rates for Shtokman and Norne reach levels of about 1 mm/h during the worst icing events over the 50 year period, while the icing rate on Norne never exceeds about 0.2 mm/h, and will only exceed 0.1 mm/h once. Figures 4.7 and 4.8 show estimated accumulated ice thicknesses, based on the icing rates in figure 4.6. For figure 4.7, all ice is assumed to melt away whenever the temperature goes above the freezing temperature of sea water. For figure 4.8, the ice is allowed to accumulate through the entire winter, but no icing will be present between 1st of April and 1st of November. Depending on how the melting is considered, ice thickness levels reach 15-30 mm on Shtokman and Skrugard, while no significant ice thicknesses are predicted for Norne. Figure 4.9 shows the wind spray flux to the point, estimating levels of up to 0.5 g/(m<sup>2</sup>s). The predicted wind flux levels are generally higher at Norne and Skrugard than at Shtokman.

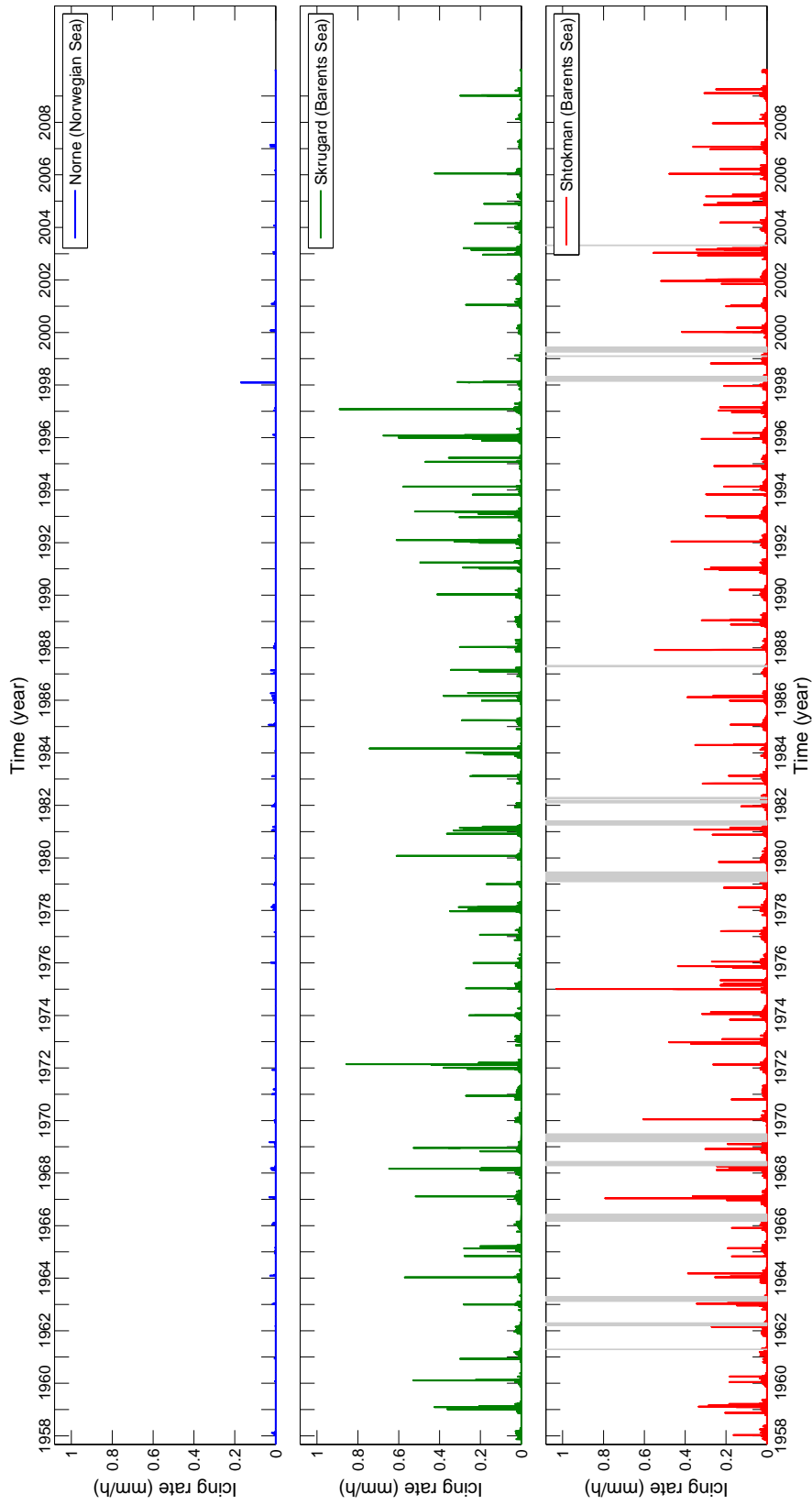


Figure 4.6: Estimated wind icing rate for the locations of Norne, Skrugard and Shtokman using hindcast Nora10 data for the period 1957-2009. Only wind generated spray is considered, and it is assumed all spray will freeze on impact. The icing rate is calculated for a vertical surface normal to the wind direction at a height of 15.7 m above surface level.

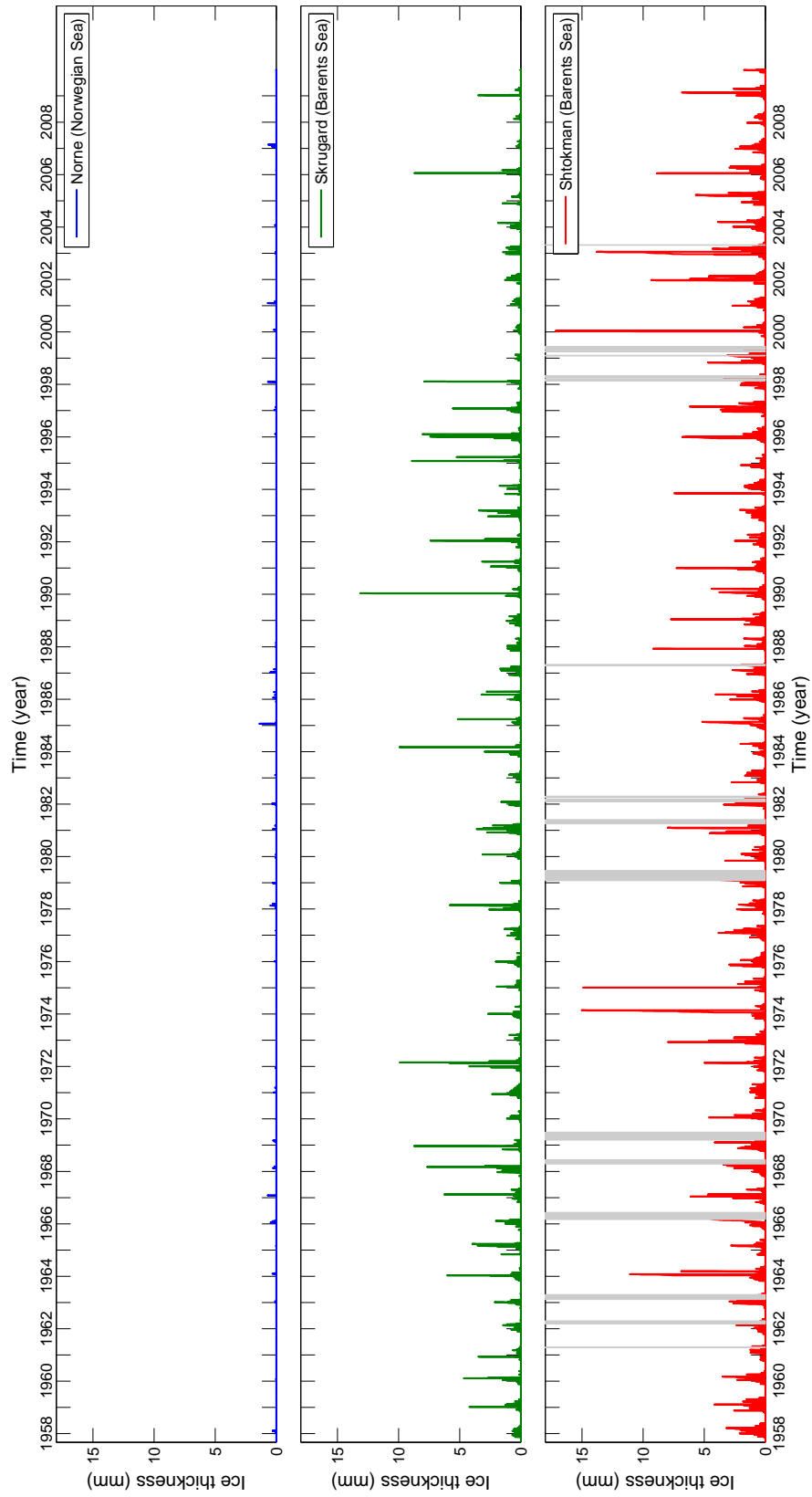


Figure 4.7: Estimated ice thickness on the locations of Norne, Skrugard and Shtokman when only wind icing is considered, for an exposed point on a vertical surface 15.7 m above surface level. The ice is assumed to completely disappear whenever the air temperature exceeds the freezing point of sea water.

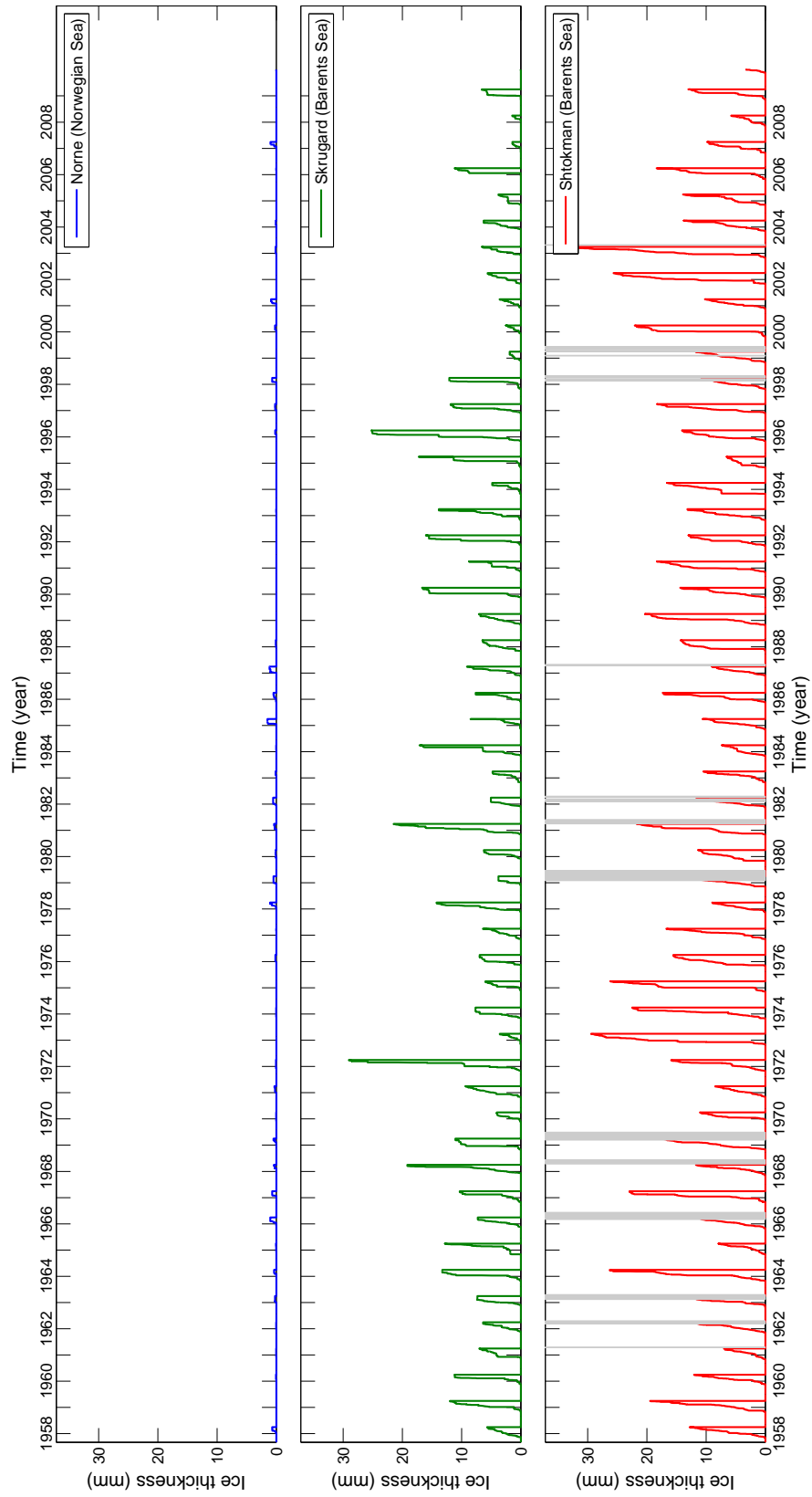


Figure 4.8: Estimated ice thickness on the locations of Norne, Skrugard and Shtokman when only wind icing is considered, for an exposed point on a vertical surface 15.7 m above surface level. The ice is allowed to accumulate over the entire winter, but no ice will be present between the 1st of April and the 1st of November.

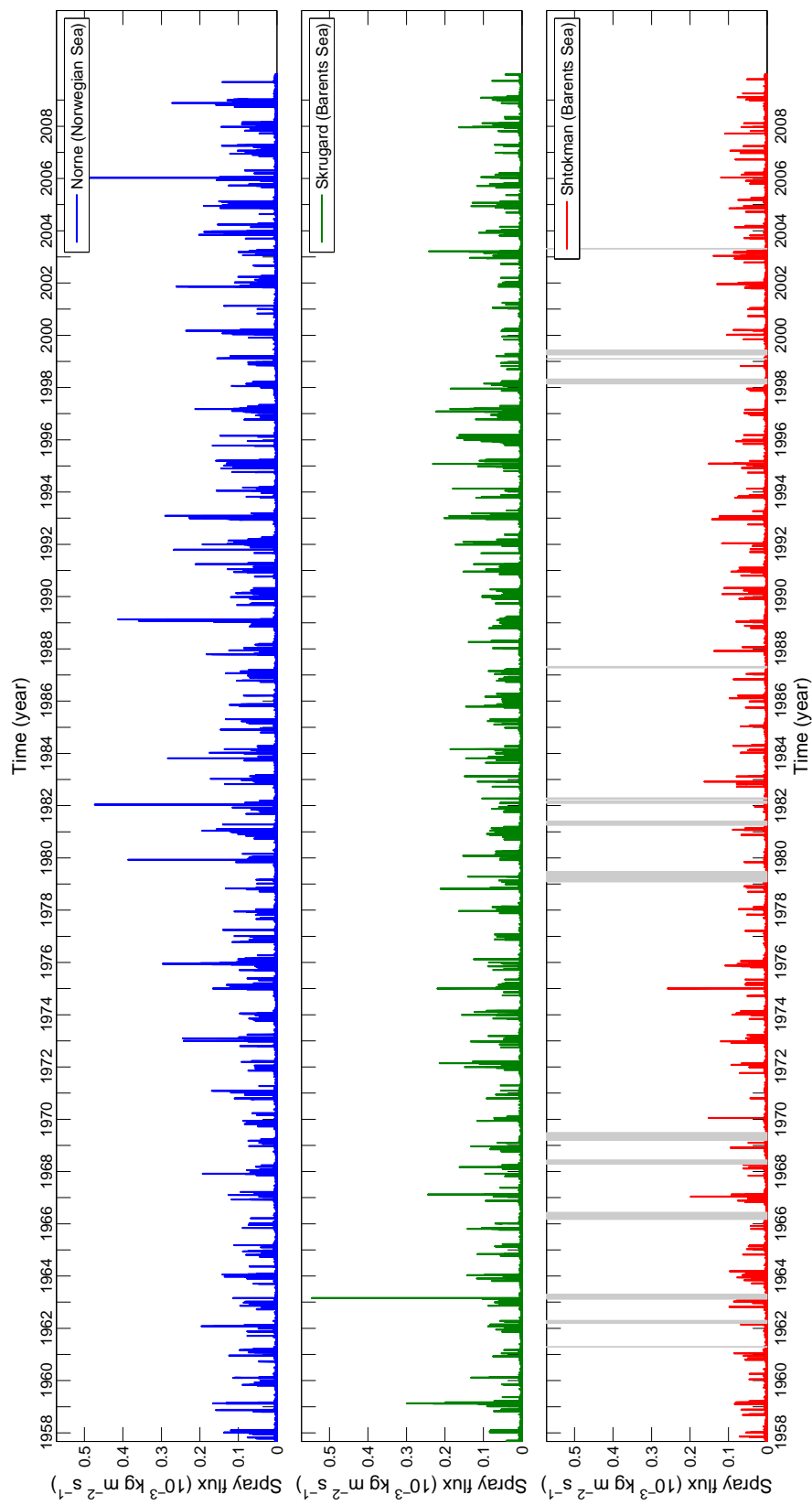


Figure 4.9: Estimated wind spray flux on the locations of Norne, Skrugard and Shtokman for an exposed point on a vertical surface 15.7 m above surface level.

## 4.2.2 Icing from both wind and wave spray

For estimating the icing rates when wave spray is included, the model has been applied to an exposed column on the Norne production vessel. This column is positioned at the front of the vessel, and lies between 13.7 and 23.7 meters above the sea surface, as shown in figure 4.10. The polygon-based geometry has not been used in this case - instead, the icing differential equations have been applied to evenly spaced points (with a  $\Delta z$  of 0.5 m) on the column. All the figures that show results for when the wave spray is included will show the result for a point 2 meters up on the column - i.e. at a height of 15.7 m above surface level. Figure 4.11 shows the estimated icing rates for this point on the column for the available hindcast data on both Norne, Skrugard and Shtokman. The most severe icing events reach icing rates of up to 15 mm/h. Once again, fewer and less severe icing events are predicted at Norne than at the two other locations. Figures 4.12 and 4.13 show the estimated ice thicknesses, similar to figures 4.7 and 4.8, reaching levels of 300 - 1000 mm at Skrugard and 700-1500 mm at Shtokman, depending on the melting rates. Figure 4.14 shows the estimated wave spray flux to the point during the spray event, reaching maxima of around 2 kg/(m<sup>2</sup>s), and once again generally showing higher spray fluxes at Norne and Skrugard than at Shtokman.

In section 5.5, the realism of the assumption that the spray jet starts at the bow level for larger vessels will be discussed. Figures 4.15 - 4.17 show the same as figures 4.11 - 4.13, except here the spray jet is assumed to start at the significant wave height  $H_s$ . If  $H_s$  is greater than the bow height  $H_{bow}$ , it is assumed the spray starts at the bow height instead. Icing rates at Skrugard and Shtokman now reach at most 4-6 mm/h, and ice thicknesses reach up 70-130 mm at Skrugard and 50-100 mm at Shtokman, depending on melting rate.

For comparison with existing algorithms for predicting icing rates, figure 4.18 shows the icing rate when calculated using the algorithm described by Overland (1990). Notice that the icing rate is well defined for the entire time period on Shtokman (i.e. no grey areas) - this is because the wave parameters that are unavailable for these periods are not used in the Overland algorithm. The algorithm estimates that icing rates at Shtokman will be drastically higher than at the other two locations, reaching values of over 150 mm/h.

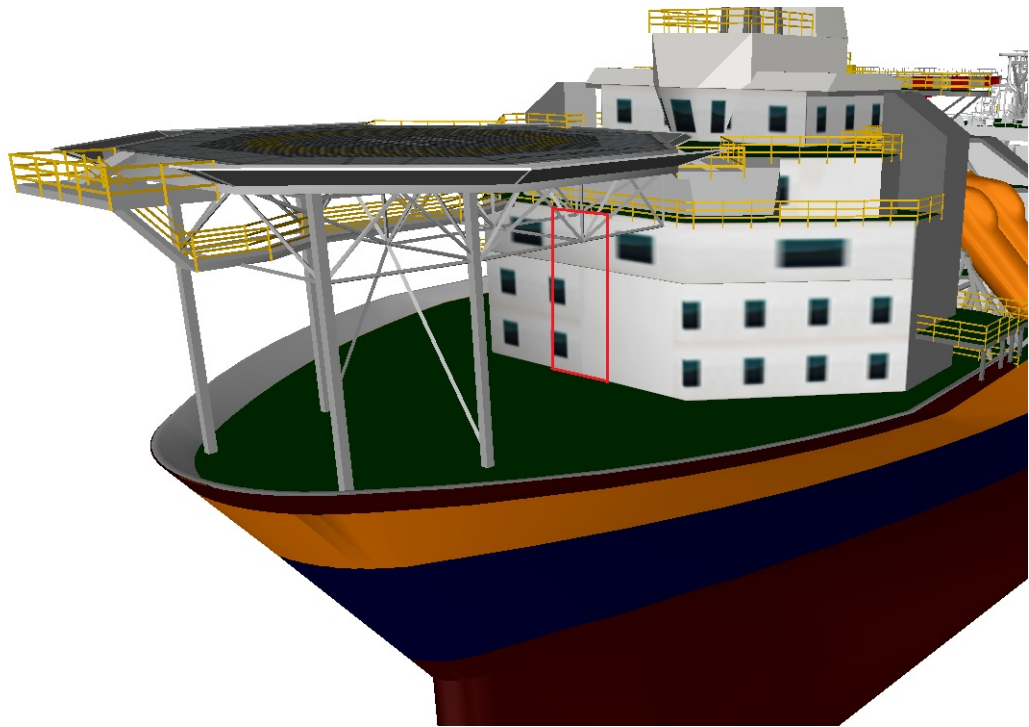


Figure 4.10: The bow area of the Norne FPSO, with the column used in the icing calculations framed in red. The column is assumed to be completely exposed in the calculations. Note that some objects on the deck have been hidden for this illustration, in order to improve visibility.

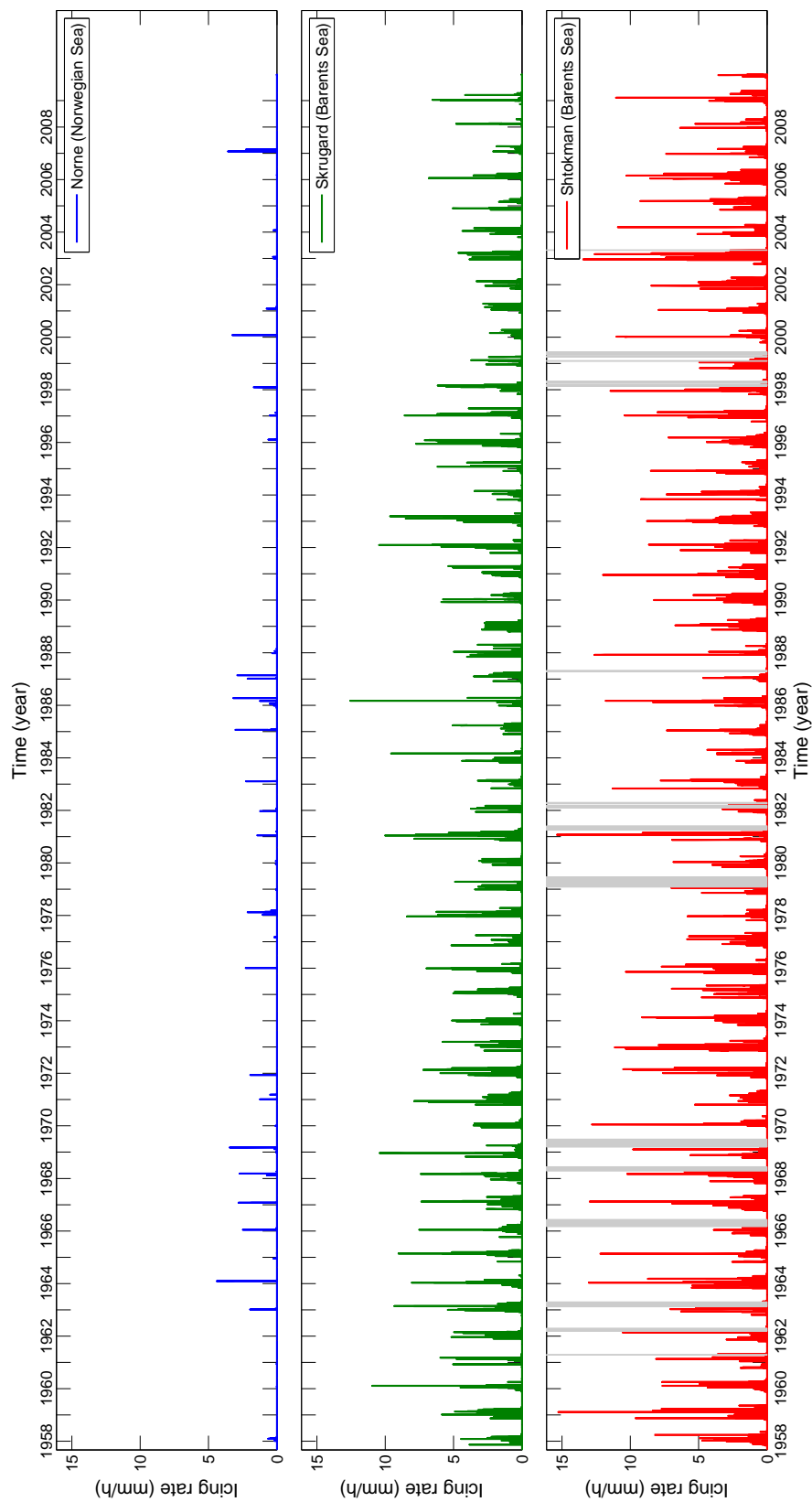


Figure 4.11: Estimated icing rate for the locations of Norne, Skrugard and Shtokman using hindcast Nora10 data for the period 1957-2009, for an exposed point at a vertical surface 15.7 meters above surface level. Both wave and wind spray is considered, and the icing is calculated from the thermodynamic icing model.

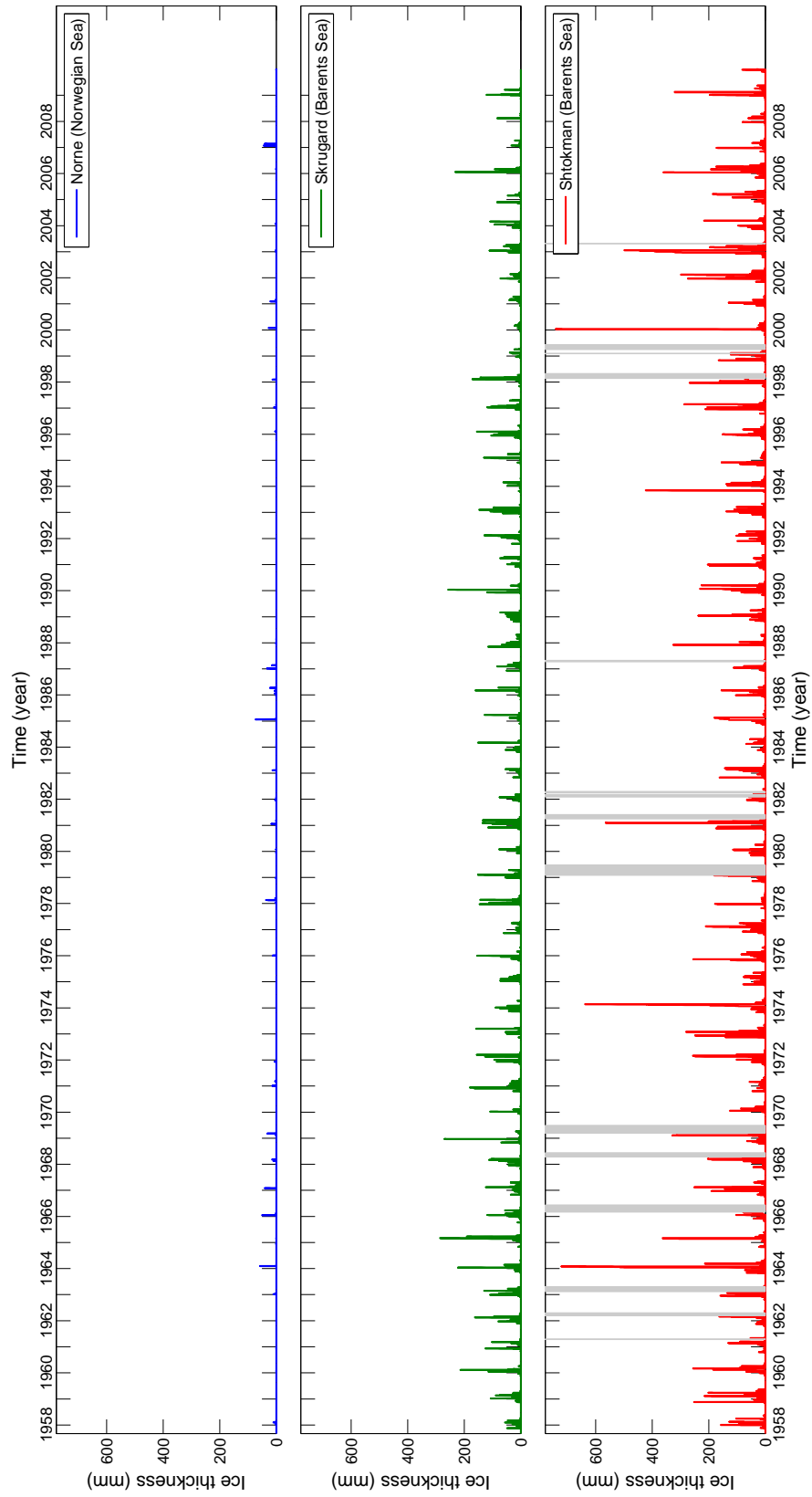


Figure 4.12: Estimated ice thickness on the locations of Norne, Skrugard and Shtokman when icing both due to wave and wind spray is considered, for an exposed point on a vertical surface 15.7 m above surface level. The ice is assumed to completely disappear whenever the air temperature exceeds the freezing point of sea water.

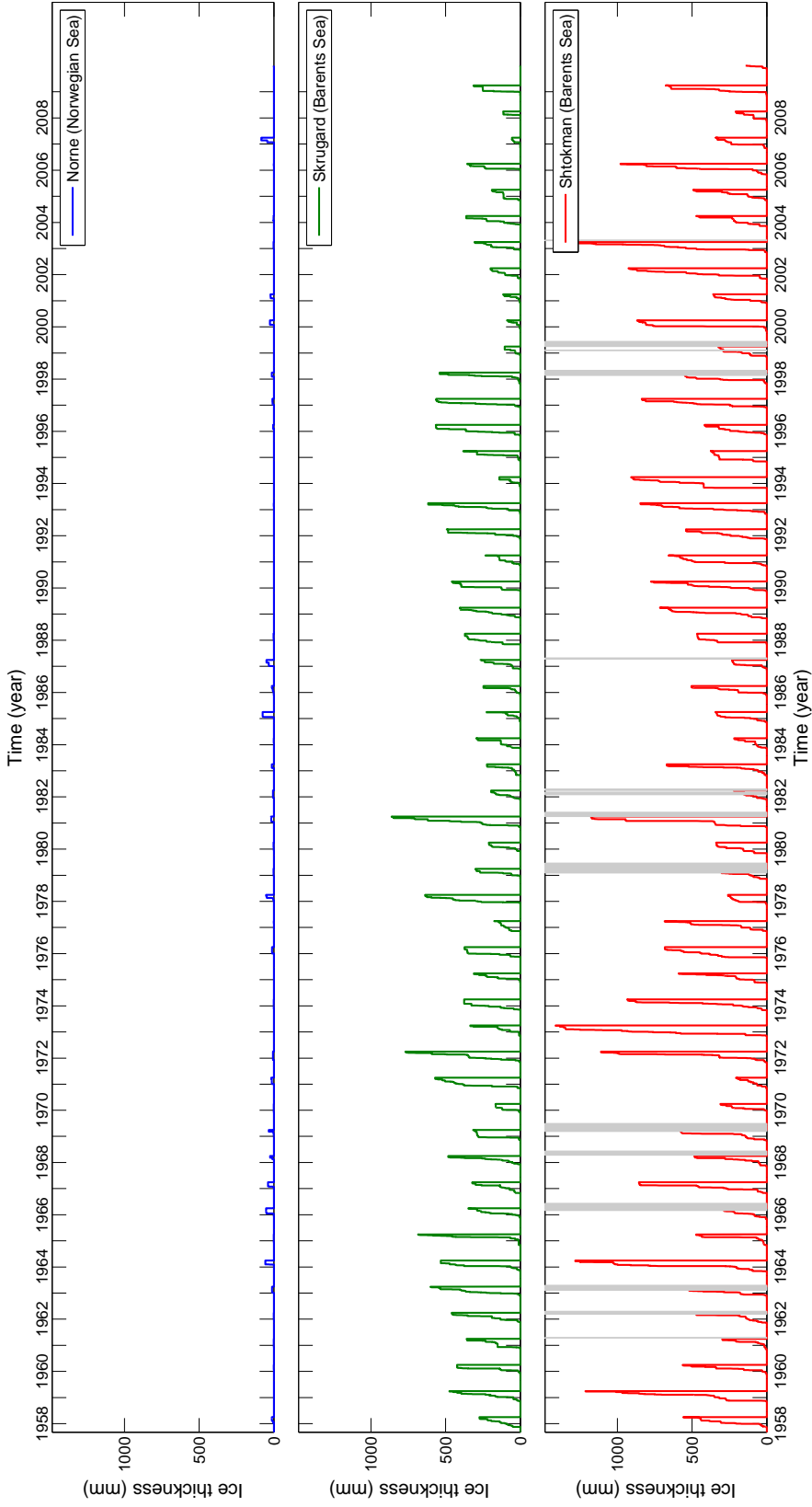


Figure 4.13: Estimated ice thickness on the locations of Norne, Skrugard and Shtokman when icing both due to wave and wind spray is considered, for an exposed point on a vertical surface 15.7 m above surface level. The ice is allowed to accumulate over the entire winter, but no ice will be present between the 1st of April and the 1st of November.

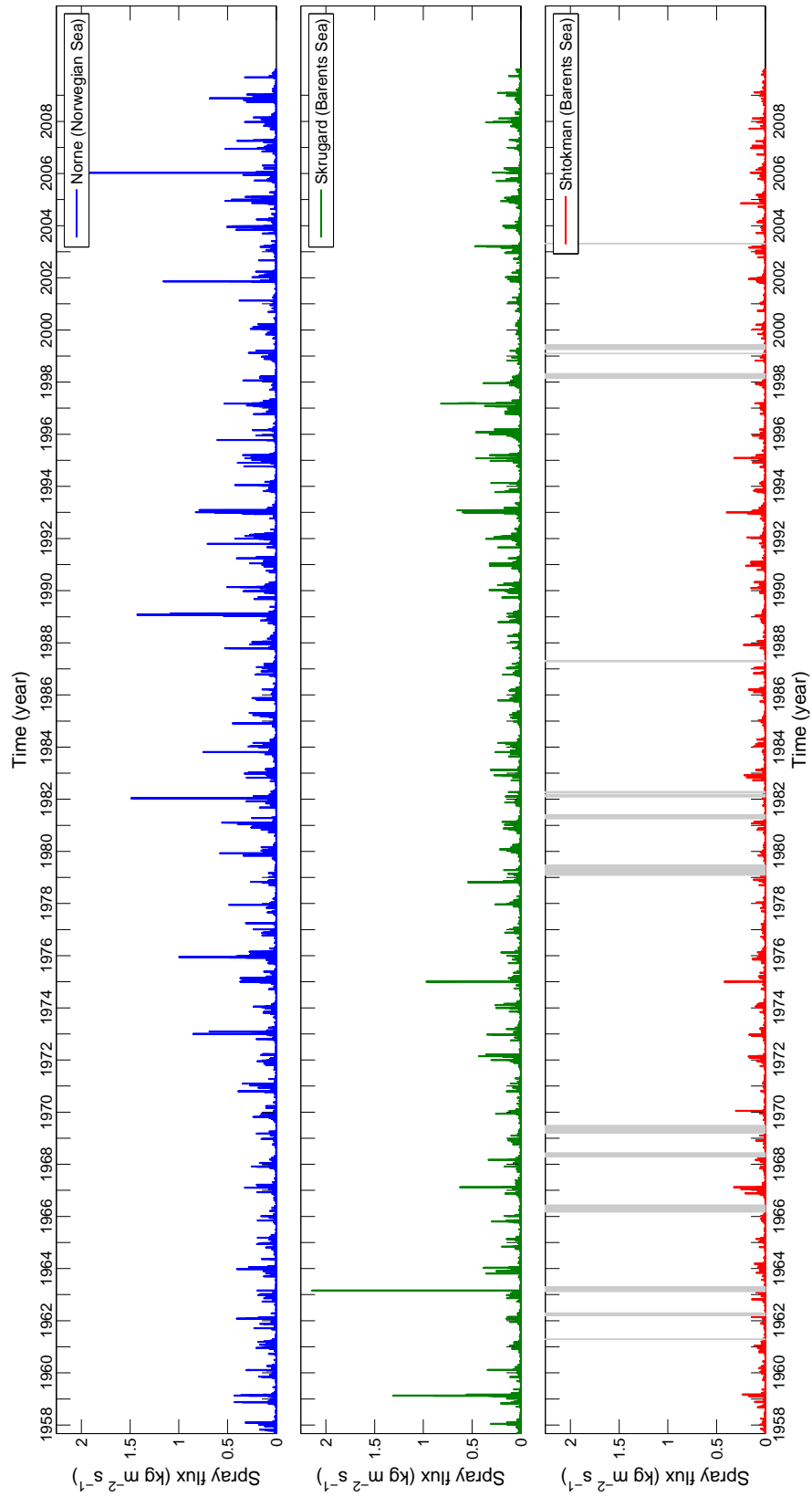


Figure 4.14: Estimated wave spray flux during the spray event on the locations of Norne, Skrugard and Shtokman for an exposed point on a vertical surface 15.7 m above surface level.

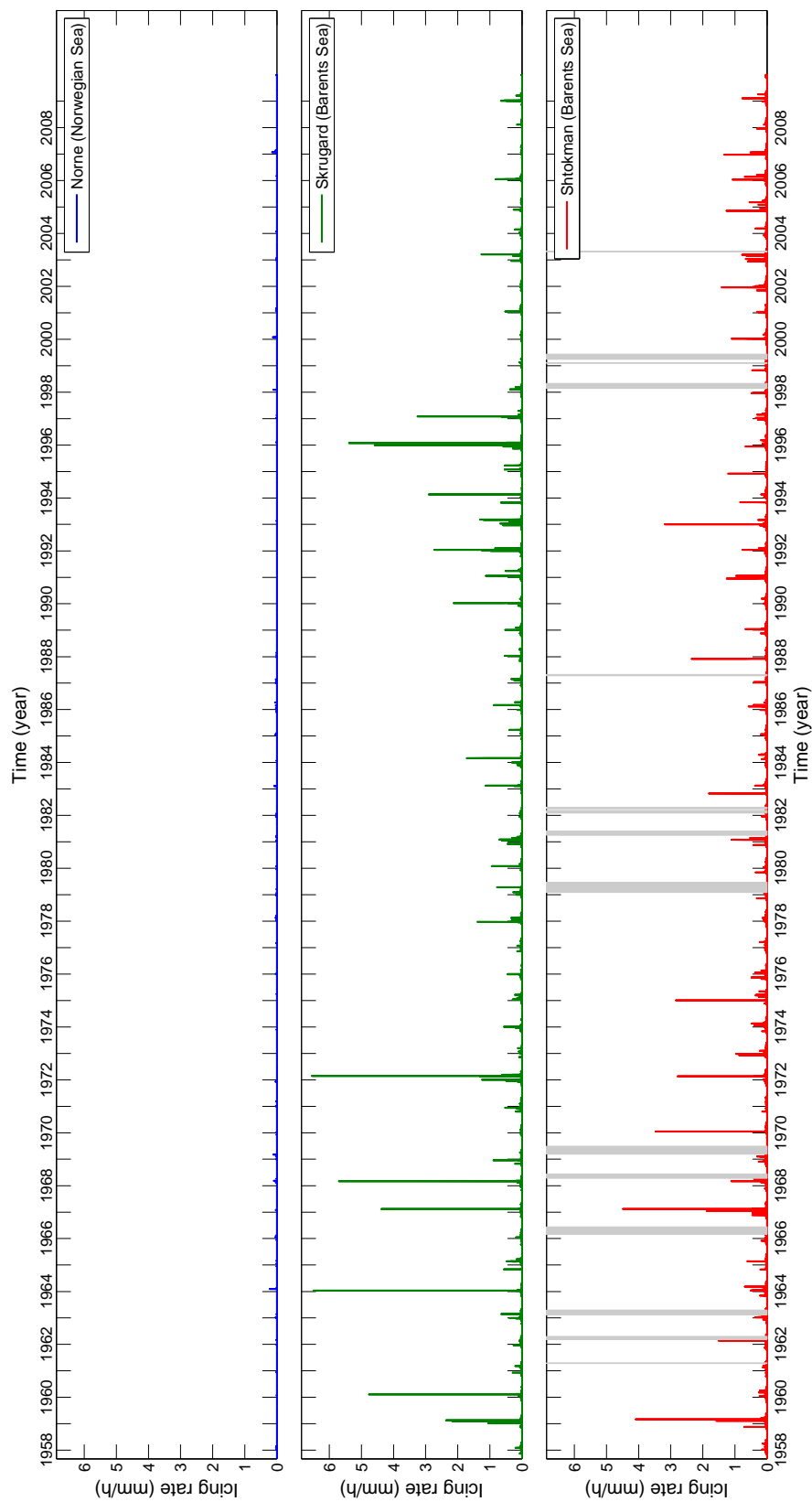


Figure 4.15: Estimated icing rate for the locations of Norne, Skrugard and Shtokman using hindcast Nora10 data for the period 1957-2009, for an exposed point at a vertical surface 15.7 m above surface level. Both wind and wave spray are considered, and the icing is calculated from the thermodynamic icing model. The spray jet is assumed to start at height  $H_s$ .

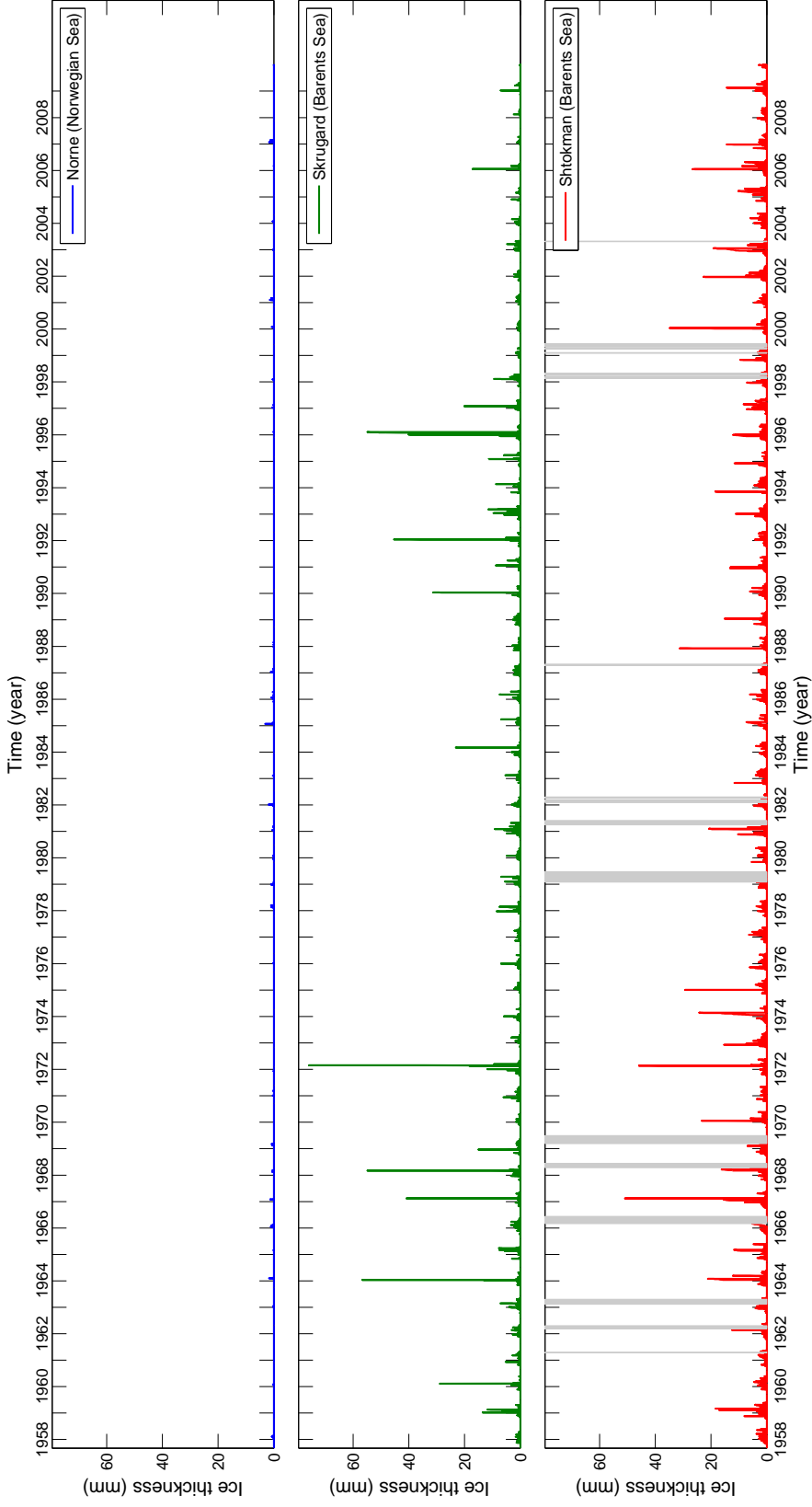


Figure 4.16: Estimated ice thickness on the locations of Norne, Skrugard and Shtokman when icing both due to wave and wind spray is considered, for an exposed point on a vertical surface 15.7 m above surface level. The spray jet is assumed to start at height  $H_s$ . The ice is assumed to completely disappear whenever the air temperature exceeds the freezing point of sea water.

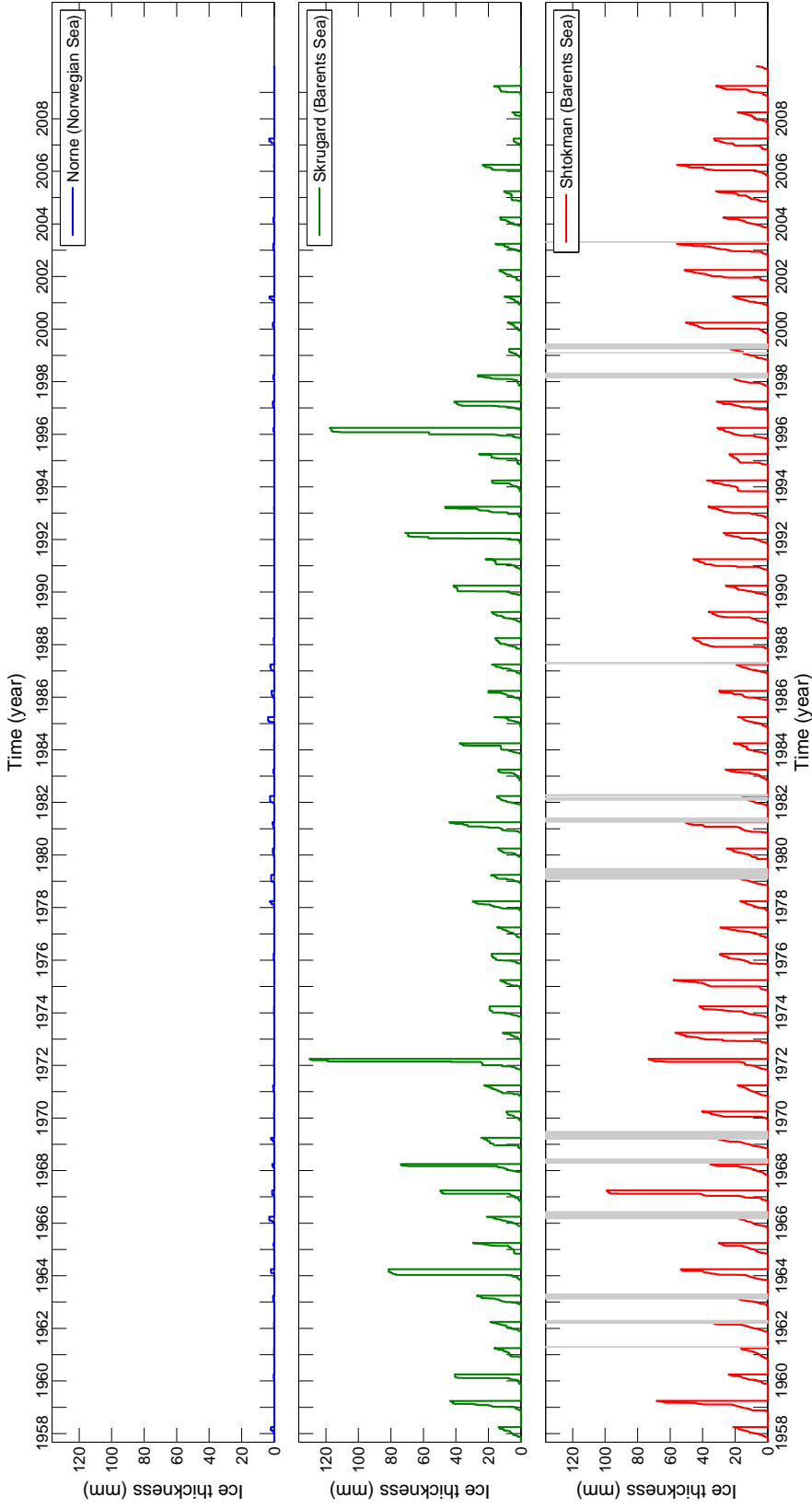


Figure 4.17: Estimated ice thickness on the locations of Norne, Skrugard and Shtokman when icing both due to wave and wind spray is considered, for an exposed point on a vertical surface 15.7 m above surface level. The spray jet is assumed to start at height  $H_s$ . The ice is allowed to accumulate over the entire winter, but no ice will be present between the 1st of April and the 1st of November.

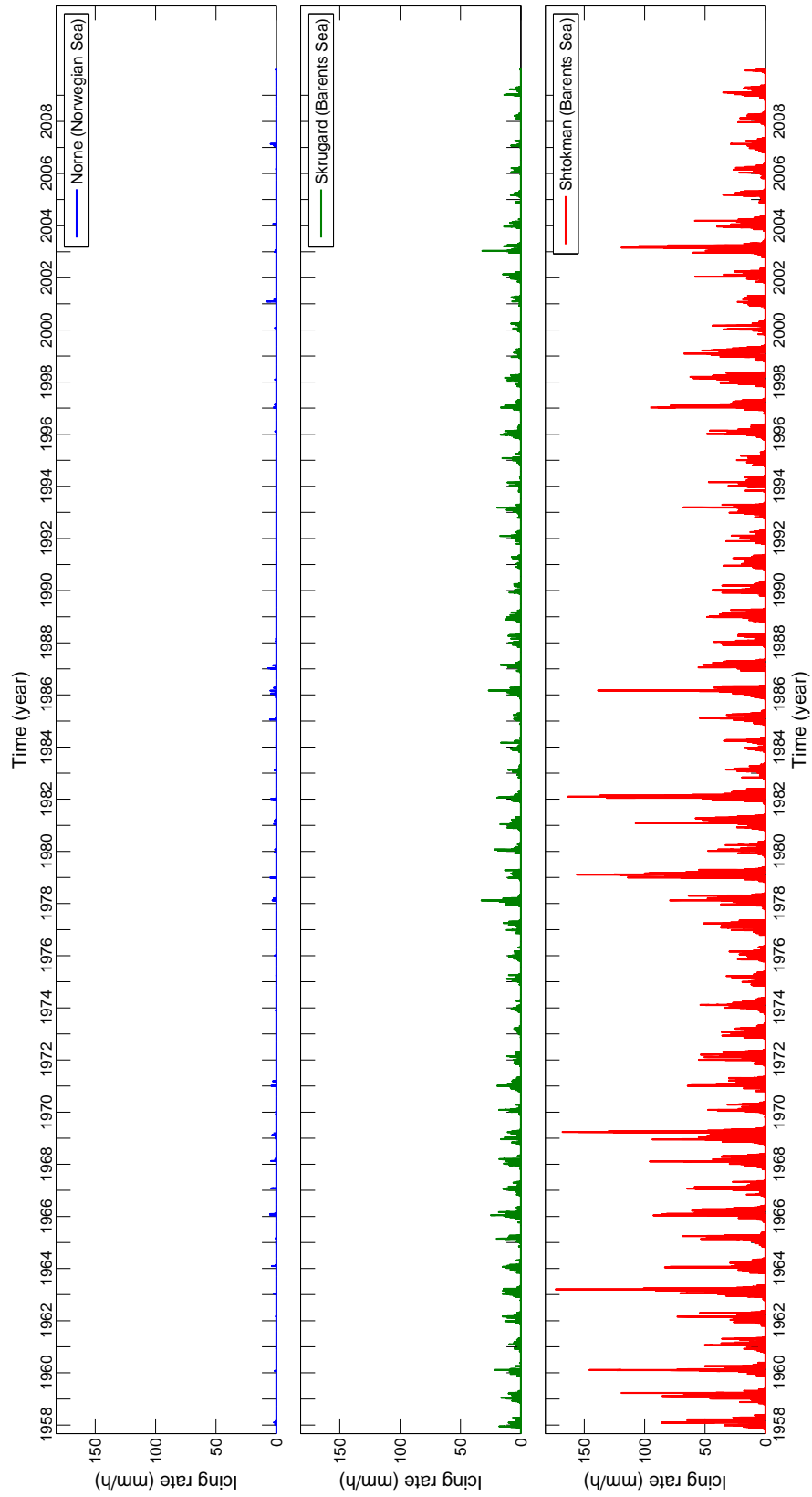


Figure 4.18: Estimated icing rate for the locations of Norne, Skrugard and Shtokman using hindcast Nora10 data for the period 1957-2009, using the algorithm described by Overland (1990) to calculate the icing rates.

### 4.2.3 Estimated annual occurrences of icing events

Based on the icing rates shown in figures 4.6, 4.11 and 4.15, figures 4.19 - 4.21 show the estimated annual occurrence rates for different ranges of icing rate amplitudes. Each calculated icing rate for one set of weather parameters is counted as one occurrence. Since the hindcast data from Nora10 are given at 3 hour intervals, multiplying the occurrence rates with a factor 3 would give a rough estimate for the expected number of hours per year with a particular icing rate.

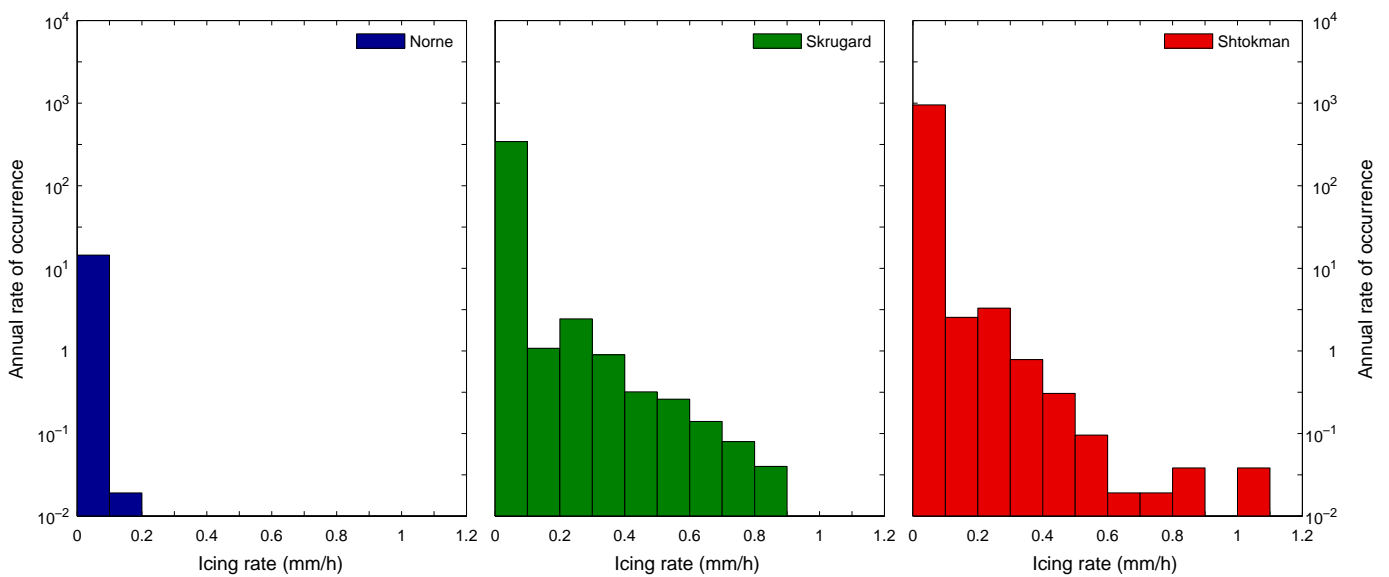


Figure 4.19: Estimated annual occurrence rate of wind icing rates for different ranges of amplitudes, on the locations of Norne, Skrugard and Shtokman, for an exposed point on a vertical surface 15.7 m above surface level.

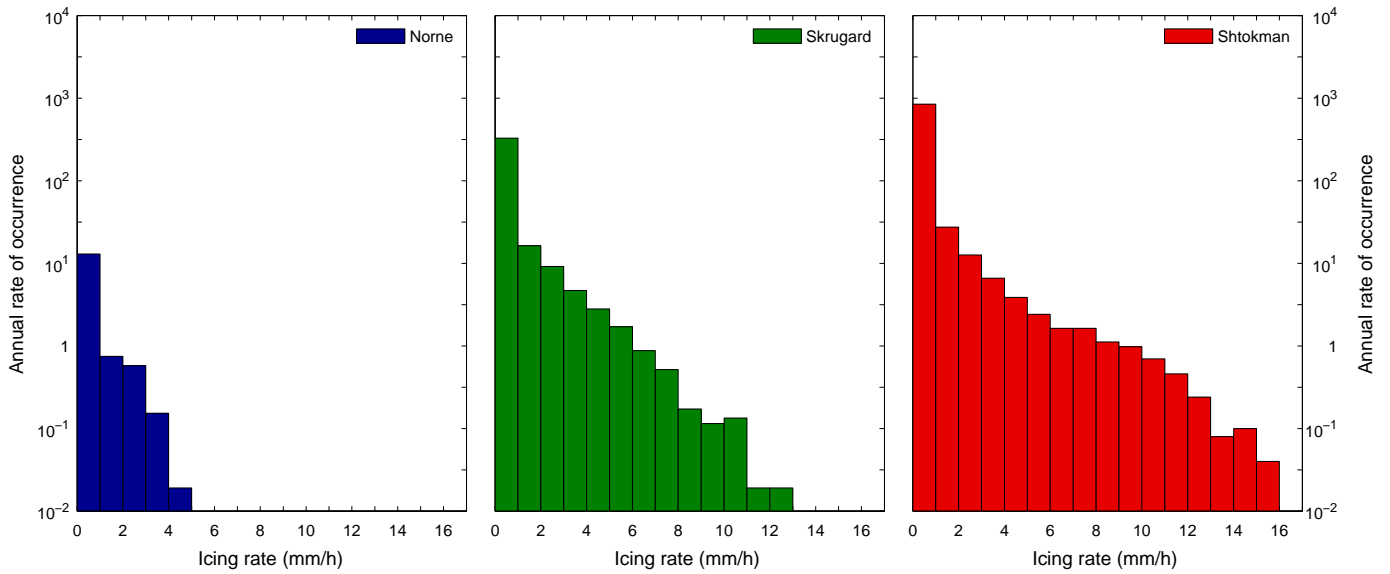


Figure 4.20: Estimated annual occurrence rate of icing rates for different ranges of amplitudes, on the locations of Norne, Skrugard and Shtokman, for an exposed point on a vertical surface 15.7 m above surface level. Both wave and wind spray is considered, and the icing is calculated from the thermodynamic icing model.

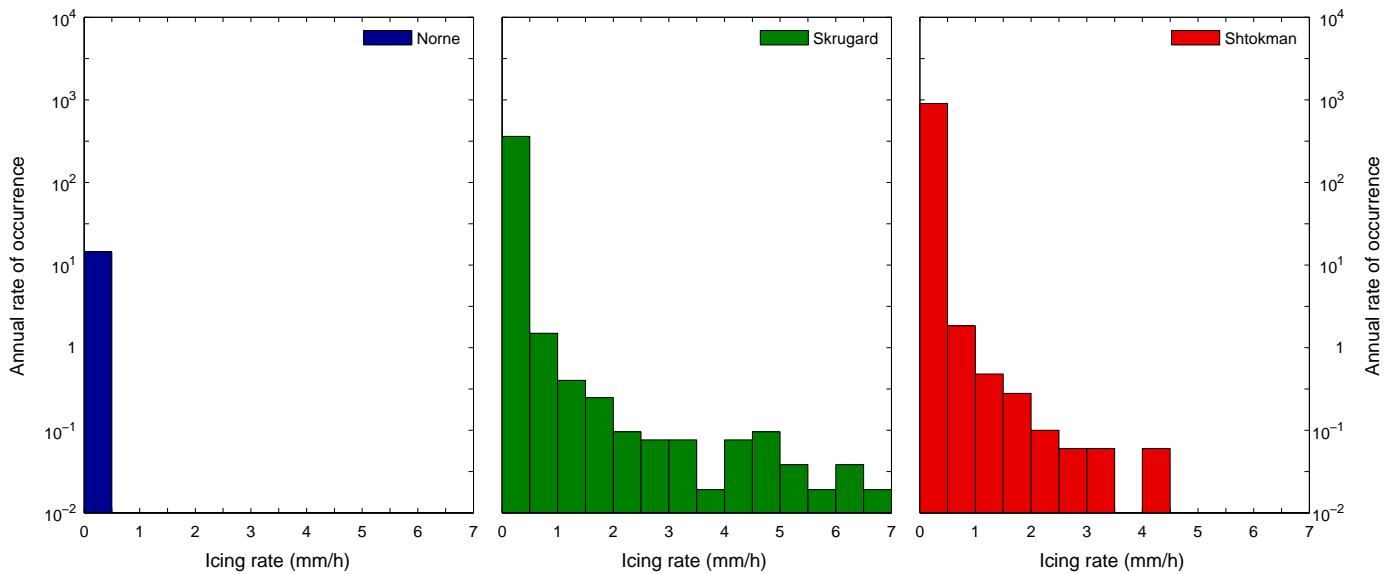


Figure 4.21: Estimated annual occurrence rate of icing rates for different ranges of amplitudes, on the locations of Norne, Skrugard and Shtokman, for an exposed point on a vertical surface 15.7 m above surface level. Both wave and wind spray is considered, and the icing is calculated from the thermodynamic icing model. The spray jet is assumed to start at height  $H_s$ .

### 4.3 Icing rates and comparison to ice thicknesses reported on AMI

For AMI, icing rates have been estimated on two columns on the ship - the first column is on the ship's mast, the second position is in front of the bridge, both columns facing the bow. The positions of each are estimated from a picture of AMI (figure 4.22), together with the length of the vessel, reported to be about 41 meters. Both columns are assumed to start in a height of 4.4 meters above sea level and end 7.4 meters above sea level. The polygon representation is not used - instead, the differential equations for icing are solved for evenly spaced points ( $\Delta z = 0.5$  m) on the column. Figure 4.23 shows the estimated icing rates calculated from the meteorological measurements of AMI for the period 1976-1984. For the icing rates on the mast and bridge, the icing rate 1 meter up on the column (i.e. at a height of 5.4 m) is shown in the figure. In addition, the estimated icing rates using the Overland (1990) algorithm are shown. The model predicts icing rates of up to 15 mm/h on the mast and 8 mm/h on the bridge, whereas the Overland algorithm will predict up to 30 mm/h of icing.

For AMI, some reported icing cases for the period December 1987 - September 1980 are listed in Eide (1983), along with rough estimates for ice thicknesses. In figure 4.24, the estimated ice thicknesses calculated from the icing rates in figure 4.23 are plotted along with the reported ice thicknesses from Eide (1983). Notice that the information about the reported thicknesses is limited - sometimes, there is information about how the ice thickness changes for a single icing case (in the figure, this is plotted as a linear increase/decrease), while other times only a single ice thickness is reported for an icing case. For the latter cases, only the reported thicknesses are shown in the figure. It is assumed all the ice melts whenever the air temperature is greater than the freezing point of sea water. Both the ice thickness on the mast and the ice thickness as predicted from the Overland icing rates will reach levels far beyond reported icing thicknesses, reaching up to 800 mm and almost 2000 mm respectively. The estimated ice thicknesses on the bridge, reaching levels of up to 120 mm, shows the best correspondence with the observed values.

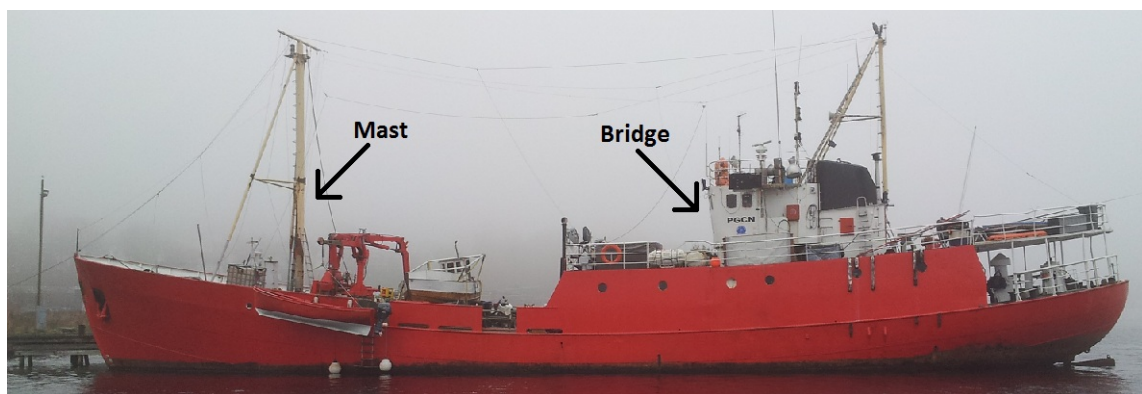


Figure 4.22: Picture of the weather ship AMI, with the locations of the bridge and the mast used in the icing calculations.

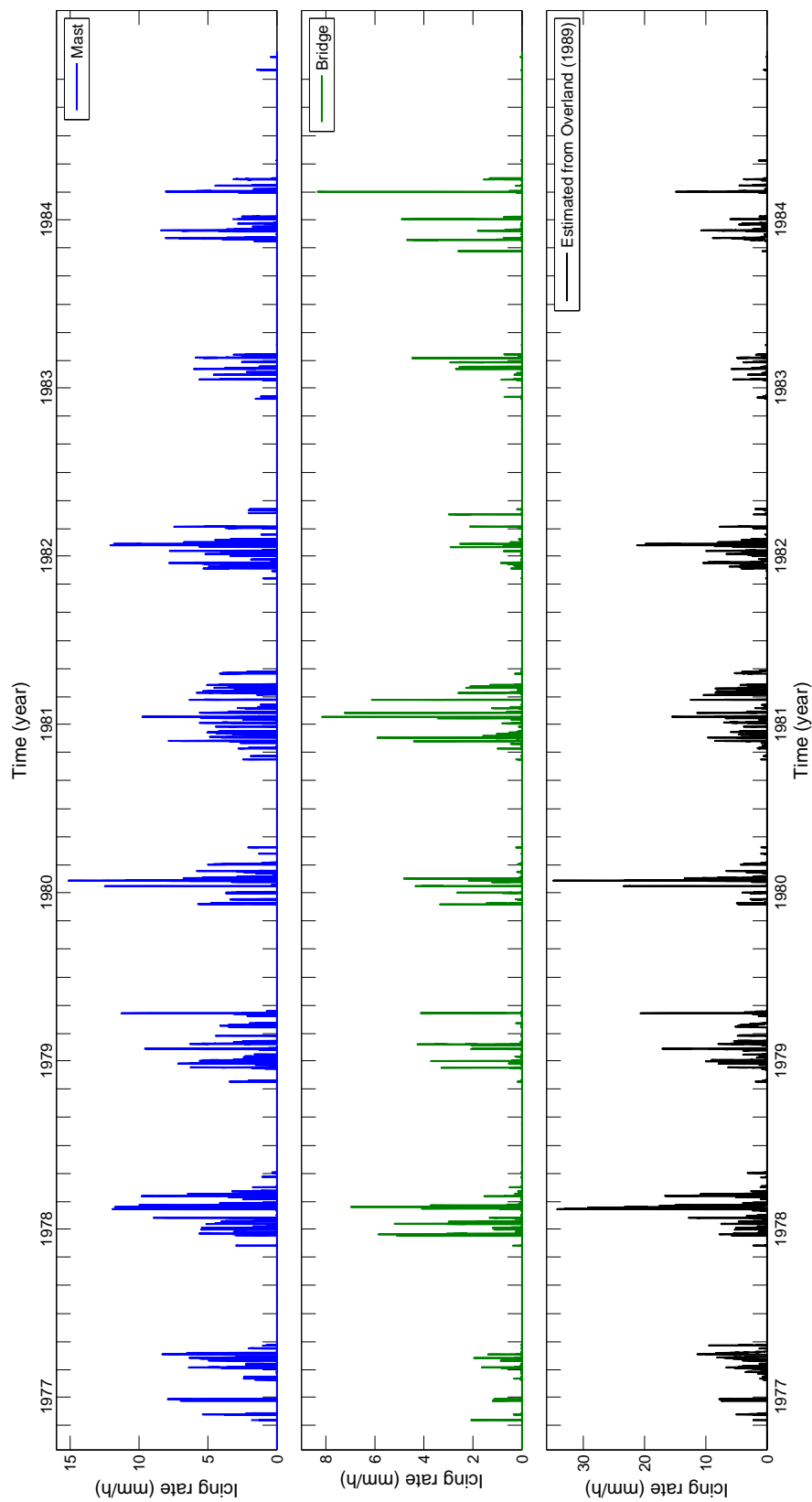


Figure 4.23: Estimated icing rates for AMI for the period 1976-1984. Icing rates are estimated for vertical columns on the mast and on the front of the bridge. The plotted icing rates are for 1 m up on the columns. The bottom graph is the icing rate estimated from the Overland (1990) algorithm.

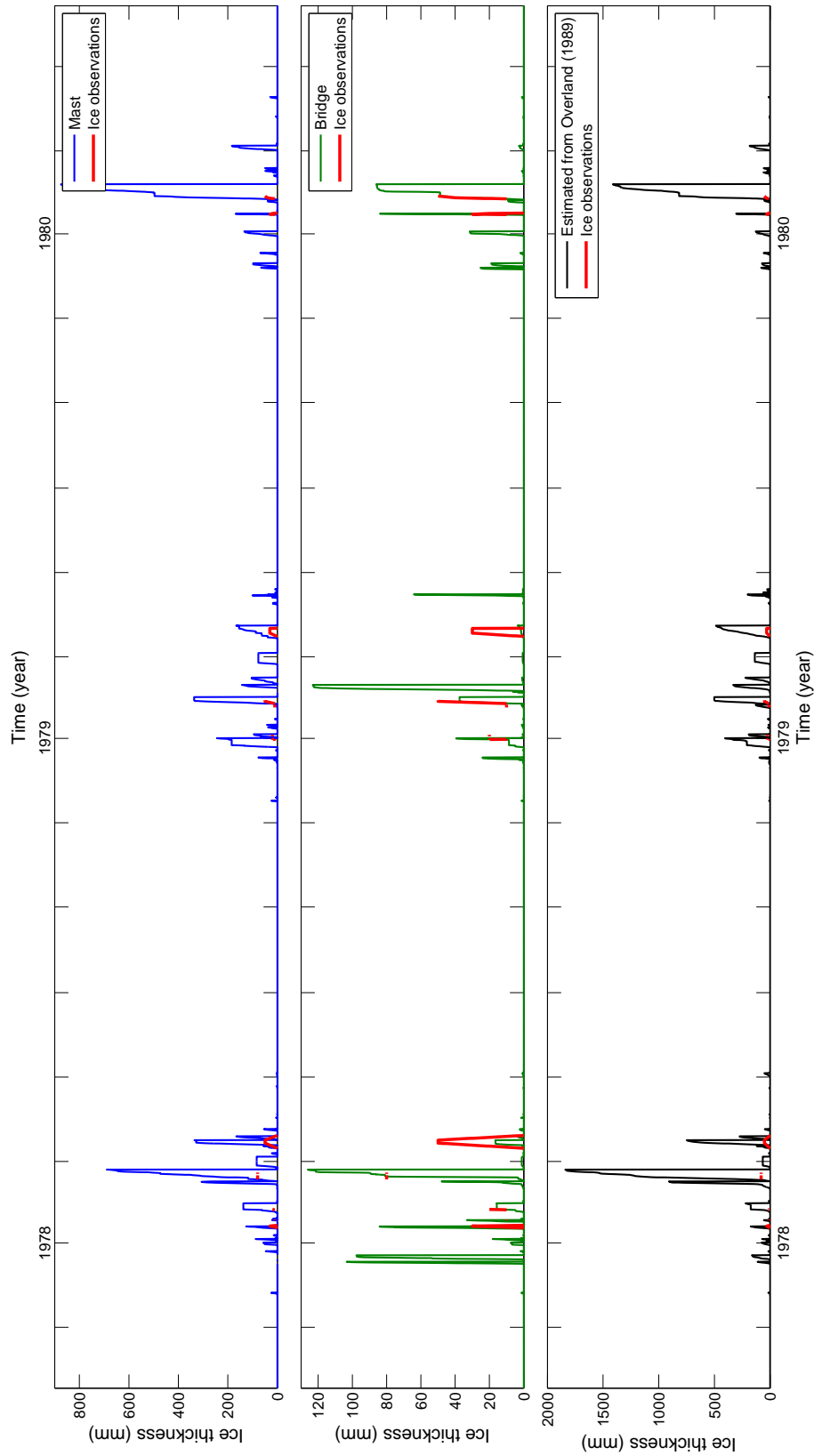


Figure 4.24: Estimated ice thickness for AMI for the period between the autumn of 1977 to the spring of 1980, using the icing rates from figure 4.23. It is assumed all ice melts for air temperatures above the freezing point of sea water. Reported ice thickness levels are plotted in red.

## 4.4 Comparison of icing rates calculated from meteorological observations and hindcast data

Since we rely on hindcast data to calculate the icing rates at the locations of the Skrugard and Shtokman fields, it would be interesting to see if there are consistent differences in icing rates when using hindcast data and when using actual meteorological observations. We have access to two relevant data sets: Observations on Norne for the period 2000-2012, and observations on AMI for the period 1976-1984 (which were used to find the icing rates in figure 4.23). In figure 4.25, the calculated icing rates for Norne when using meteorological observations and when using hindcast data are plotted for the period 2000-2009. As in figure 4.11, the icing rate is calculated for a point 2 m up on a 10 m vertical exposed column (i.e. at 15.7 m above the sea surface), and both wave spray and wind spray are considered. When using meteorological observations, the icing events on Norne are both more severe and much more frequent. Figure 4.26 shows the calculated icing rate on the front of the bridge of AMI both when using meteorological observations and hindcast data. Just like in figure 4.23, the icing rate is plotted for a point 1 m up on the bridge, and both wave spray and wind spray are considered. Here, the icing events are somewhat more severe when using meteorological observations, but not significantly more frequent.

In order to further examine the difference between the meteorological observations and the hindcast data, the frequency of high wind speeds and low temperatures (the two most important weather parameters for icing) are calculated both for Norne for the period 2000-2009 and AMI for 1976-1984. Figure 4.27 shows the calculated expected time (in hours/year) the air temperature will be in certain ranges of sub-zero temperature for both observed and hindcast data. As mentioned in the figure label, the weather observations at Norne are taken 33 m above surface level, and the hindcast data estimates the temperature at 2 m above surface level. Similarly, figure 4.28 shows the calculated expected time (in hours/year) that the wind speed will be in certain ranges of high ( $> 20$  m/s) wind speeds. As mentioned in the figure, the hindcast wind speed is estimated at 10 m above surface level. Figures 4.29 and 4.30 show the same for AMI. The height of the observations on AMI is unknown, although it is certainly lower than for Norne, considering AMI is a much smaller vessel.

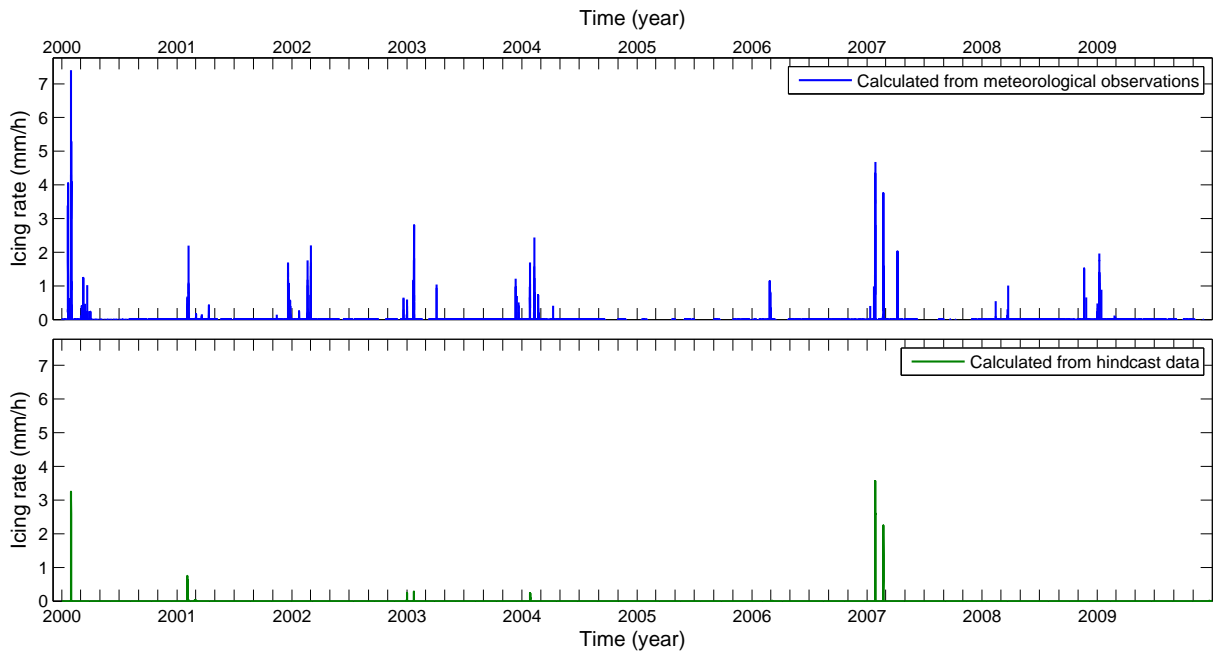


Figure 4.25: Estimated icing rate for Norne at an exposed point on a vertical surface 15.7 m above surface level, when calculated from meteorological observations and hindcast data.

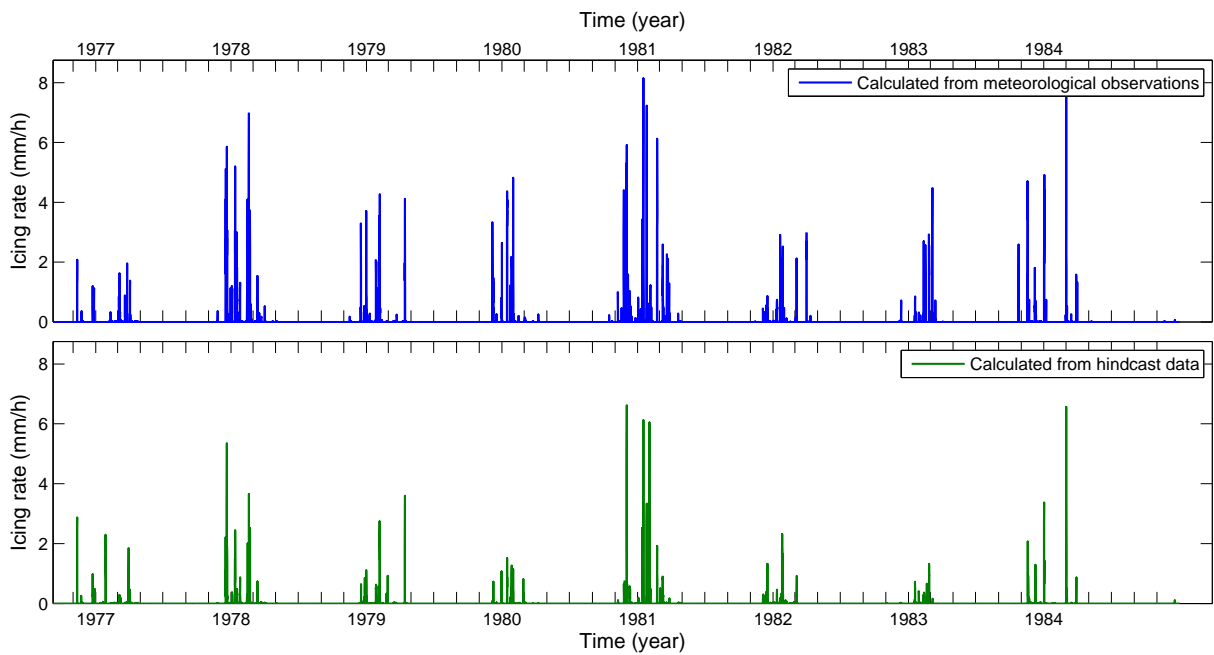


Figure 4.26: Estimated icing rate for AMI at 1 m up on the front of the bridge, when calculated from meteorological observations and hindcast data.

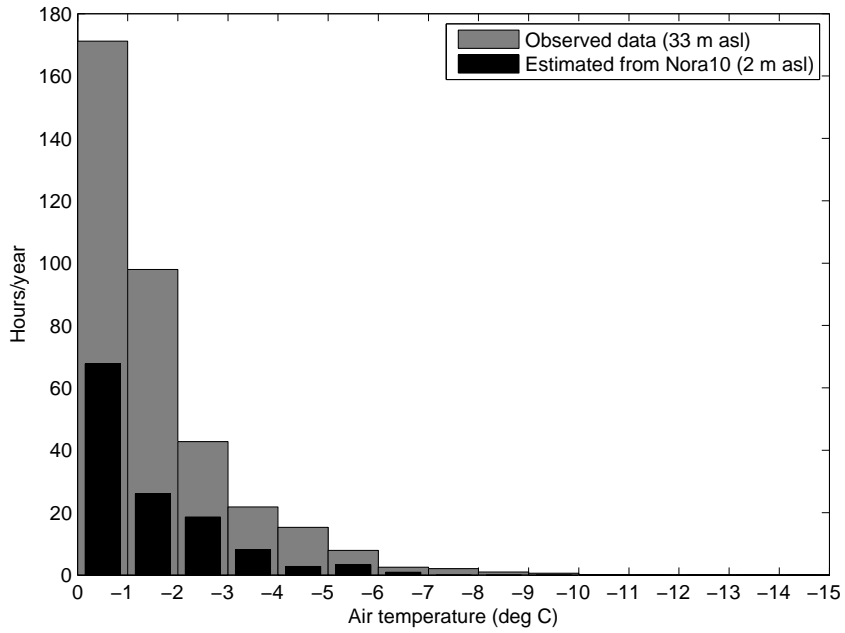


Figure 4.27: Estimated relative time that the air temperature on Norne will be in certain ranges of sub-zero temperature, for both meteorological observations and hindcast data.

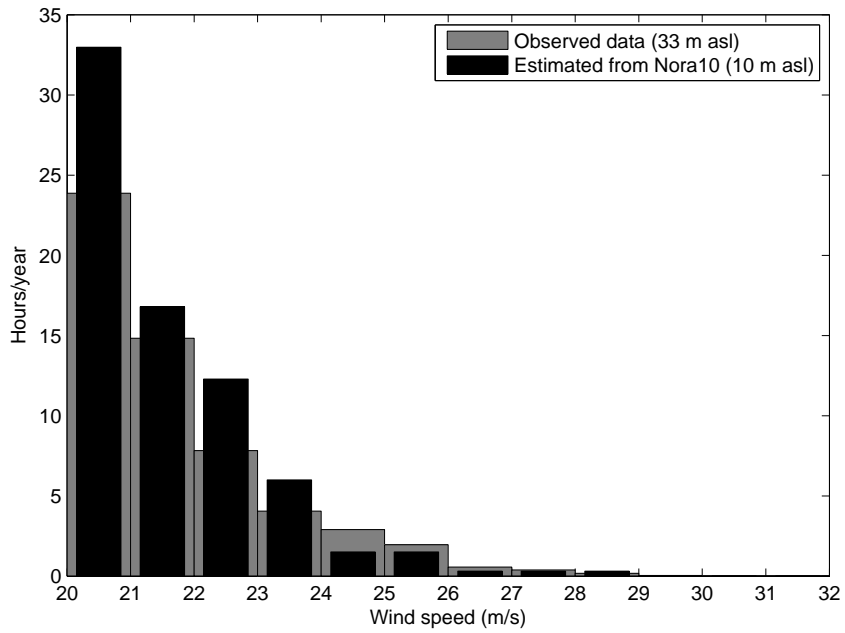


Figure 4.28: Estimated relative time that the wind on Norne will be in certain ranges of high wind speeds, for both meteorological observations and hindcast data.

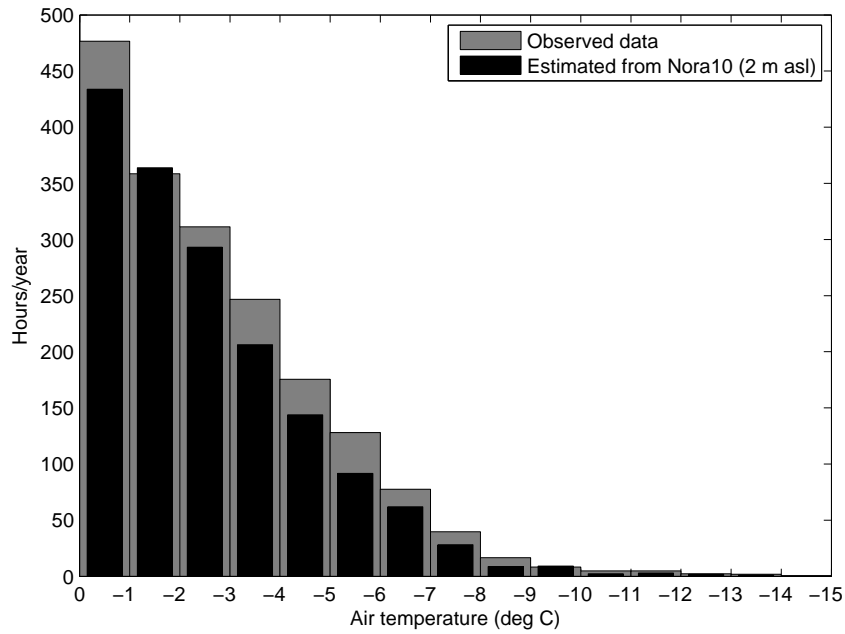


Figure 4.29: Estimated relative time that the air temperature on AMI will be in certain ranges of sub-zero temperature, for both meteorological observations and hindcast data.

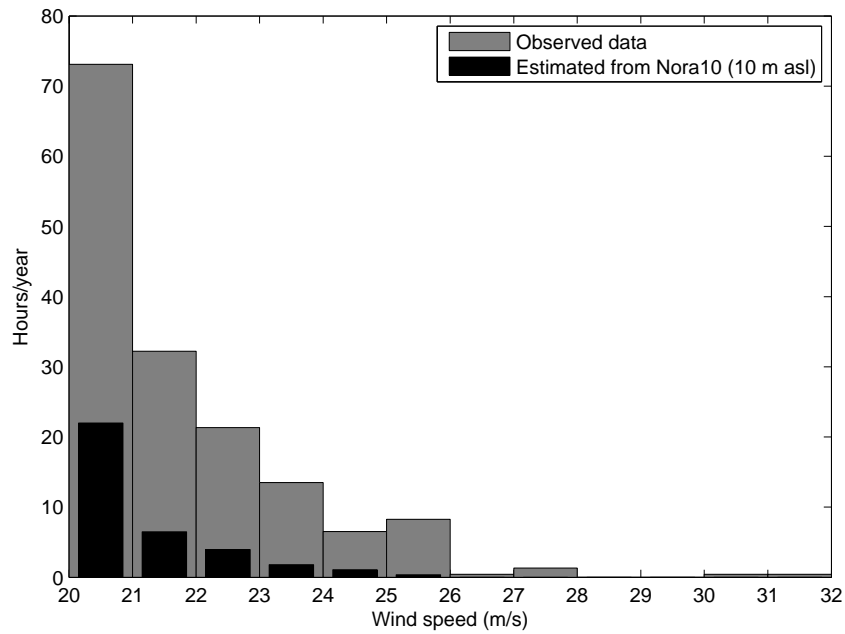


Figure 4.30: Estimated relative time that the wind on AMI will be in certain ranges of high wind speeds, for both meteorological observations and hindcast data.

## 4.5 Total icing on a vessel

Since the model for the icing rate on the entire vessel is far more calculation-intensive than estimating the icing rate for an exposed reference object/column, this has not been done for all the available meteorological data. However, in order to illustrate the type of results one would get from this model, a few examples will be provided in this section. Figure 4.31 shows the estimated icing rate on Geofjord for the case  $U_{10} = 20$  m/s,  $T_s = 4^\circ\text{C}$ ,  $T_a = -5^\circ\text{C}$ ,  $H_s = 5$  m,  $\alpha = 20^\circ$  and  $v_s = 0$  m/s. In the figure, it is easy to see how the wave spray (which is the cause of the strongest icing) starts around the bow and is blown onto the ship at an angle of  $20^\circ$ . Figure 4.32 shows the icing rate for AMI for the same conditions. In both cases, icing rates up to 5-6 mm/h are predicted. Notice that the angle  $\alpha = 20^\circ$  is easy to spot in both figures, since the spray jet (and thus the strongest icing rates) will travel along the wind direction.

Figure 4.33 shows the estimated icing rate on the Norne FPSO, when weather parameters are the same as for the strongest icing case estimated using the hindcast data for Shtokman. Specifically, the strongest estimated icing case was at 28.01.1981 at 3 pm. The weather parameters for this case are  $T_a = -10.9^\circ\text{C}$ ,  $H_s = 7.7$  m,  $\tau_w = 12.3$  s, and  $U_{10} = 21.1$  m/s. The vessel is assumed to have heading directly against the wind ( $\alpha = 0$ ). Only the front of the vessel is shown, since the bridge will mostly shield the remainder of the ship. The maximum icing rate on any polygon is about 20 mm/h. The total ice accumulation rate on the vessel is estimated to be 2.5 kg/s, or 9 tons/hour.

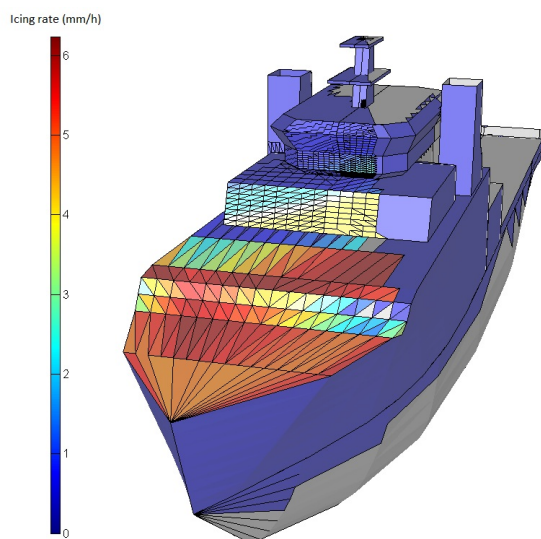


Figure 4.31: Icing rate on the Geofjord vessel for  $U_{10} = 20$  m/s,  $T_s = 4^\circ\text{C}$ ,  $T_a = -5^\circ\text{C}$ ,  $H_s = 5$  m and  $\alpha = 20^\circ$ .

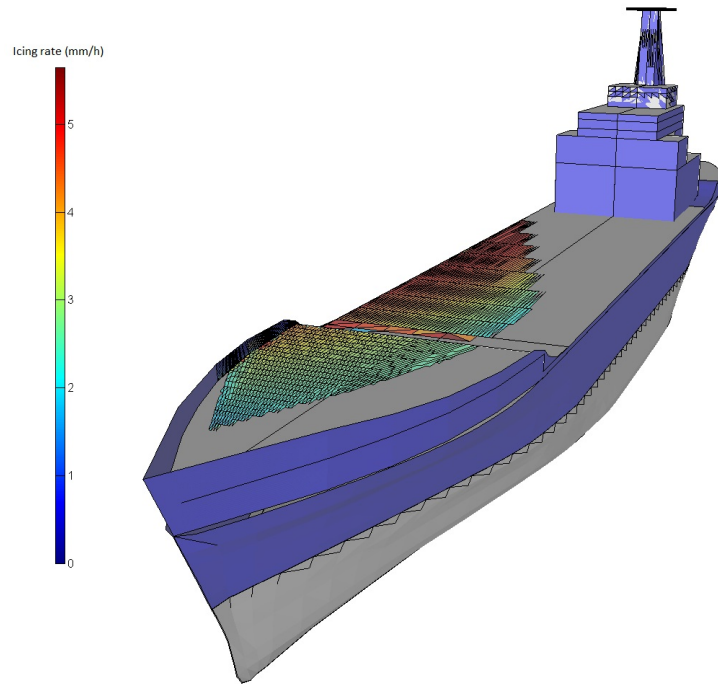


Figure 4.32: Icing rate on the AMI vessel for  $U_{10} = 20$  m/s,  $T_s = 4^\circ\text{C}$ ,  $T_a = -5^\circ\text{C}$ ,  $H_s = 5$  m and  $\alpha = 20^\circ$ .

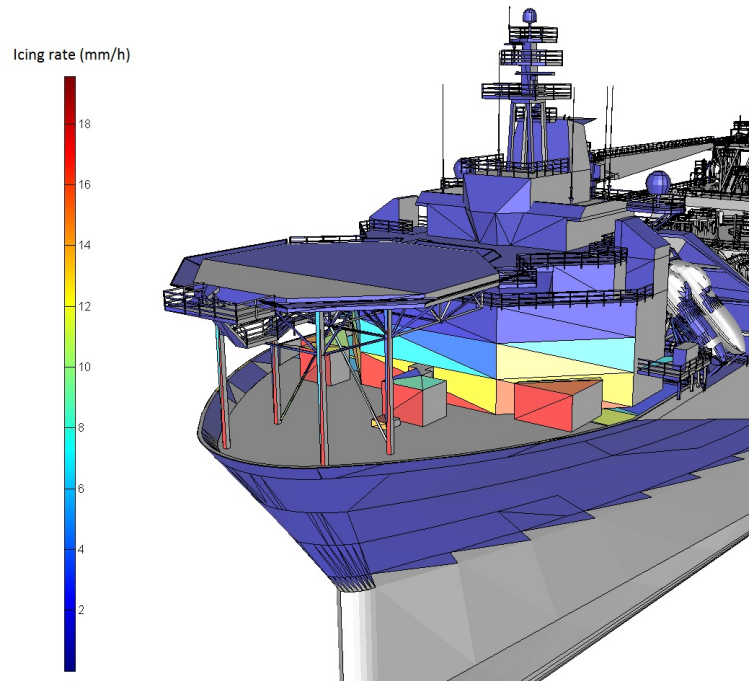


Figure 4.33: Icing rate on Norne for  $T_a = -10.9^\circ\text{C}$ ,  $H_s = 7.7$  m,  $\tau_w = 12.3$  s,  $U_{10} = 21.1$  m/s and  $\alpha = 0$ .

# Chapter 5

## Discussion

### 5.1 Icing at Norne, Skrugard and Shtokman

#### 5.1.1 Melting and accumulation of ice

In chapter 4, the accumulated ice thicknesses are generally plotted for two cases. In the first case, all ice will melt when the air temperature exceeds the freezing point of sea water. In the second case, the ice is allowed to accumulate through the entire winter, only melting at the 1st of April. The reason why these two very simple cases has been used to present ice accumulation is that ice melting has not been investigated in this thesis. The two cases are designed to present an upper and lower bound on the melting rate, and thus give a lower and upper bound on the accumulated ice thicknesses (when melting is the only source of ice removal). If the thicknesses of accumulated ice should be investigated further, a more sophisticated model for ice melting should be included in the model.

Also, no source of ice removal apart from melting has been considered. In reality, the ice may be removed by for example the impact of spray water, or manual removal by the crew. The strain from vessel movements and the ice's own weight will also limit the ice thickness - an ice thickness in the order of meters, as shown in some of the graphs of accumulated ice, is of course unrealistic.

It should also be mentioned that the icing rate in some cases will be negative (the graphs for icing rate will only show the positive values, since these are considered most interesting). Physically, this happens when the spray flux is large and the air temperature is close to the freezing point, so that the total positive heat flux from the wave spray during the spray event exceeds the sum of all negative heat flux for the entire spray period. In other words, a high spray flux may contribute to ice melting. The accumulated ice thickness includes negative icing rates, so this effect is included in the ice thickness results.

#### 5.1.2 Icing purely from wind spray

From figure 4.6, we see that the predicted wind icing for the Skrugard and Shtokman are approximately the same, and both are much greater than for Norne. Interestingly, we see from figure 4.9 that there is generally more wind flux on Norne, meaning that the only reason

why wind icing is predicted to be a larger problem on Skrugard and Shtokman is the higher frequency of air temperatures below the freezing point. Figure 4.9 also shows that there is more wind flux on Skrugard than on Shtokman, yet the icing rates are approximately the same. The reason for this is that frequency of cold days on Shtokman is greater than for Skrugard. It is interesting that (according to the model) the greater wind fluxes on Skrugard causes wind icing to be an equally large concern for Skrugard as for Shtokman, even though conditions at Shtokman are significantly colder.

From figure 4.19, it can be observed that icing events for all ranges of severity will be far more common on Skrugard and Shtokman than on Norne, and that all the severe icing events are reserved for these two locations. The most severe icing events seems to occur on Shtokman.

Figures 4.7 and 4.8 indicate accumulated ice thicknesses of up to an order of 15-30 mm, purely due to wind icing. The large uncertainties in wind spray concentration functions as well as the high sensitivity to wind speed (described in section 5.4) means these numbers are highly uncertain, and the accumulated thicknesses could potentially be much larger.

It should also be noted that the predicted wind icing rates at the three different locations (two of which are in quite cold regions) over a 50 year period only reaches a maximum of around 1 mm/h. This is not even close to the icing rates calculated for Ocean Bounty during a single winter season (up to more than 7 mm/h, see figure 4.1). The reason for this is the extremely high wind speeds measured at Ocean Bounty, reaching almost  $U_{10} = 40$  m/s.

### 5.1.3 Icing from both wind and wave spray

From figure 4.11 and figure 4.20, we see that the model predicts significantly higher icing rates for parts of the vessel that are exposed to wave spray as well as wind spray, reaching maxima of over 15 mm/h. Once again, the model predicts significantly higher icing rates at Shtokman and Skrugard than at Norne. Shtokman appears to have consistently stronger icing rates than Norne, and the difference between the two is greater than for pure wind icing. This is not unexpected - the large wave spray fluxes means that the icing will be thermally limited (i.e. limited by the amount of heat that is transported away from the surface), which means the colder temperatures at Shtokman will give higher icing rates than at Skrugard. Predicted ice thicknesses reach levels of 300-1000 mm for Skrugard and 700-1500 mm for Shtokman (figures 4.12 and 4.13). Of course, there are other factors that will limit the ice thickness, but the results illustrate the point that air temperatures can be below freezing temperature for extended periods of time at the locations of Skrugard and Shtokman, which may give high ice accumulations over time on exposed areas unless ice is actively removed. Also, from figure 4.14, we see Shtokman still has the least spray flux - it appears the locations of Norne and Skrugard are more exposed to wind and high waves, the most important parameters in the flux calculations.

It is mentioned in section 5.5 that certain assumptions in the model for generation of wave spray, especially the assumption that the spray jet starts at the bow level, are probably unrealistic for larger vessels. Therefore, an alternative situation where the spray jet starts in significant wave height is considered, and the resulting icing rates are plotted in figure 4.15. Although even the highest peaks in icing rates are reduced by this, the main effect appears to

be to increase the relative difference between cases with high and low icing. This is because high wind speed and high wave heights are very much correlated. Thus, the cases with high wind speed, where icing is already high, will have correspondingly high wave heights and therefore not be as affected by the change in height level for the spray jet as cases with lower wind speeds/wave heights. Also, as seen in figure 4.21, the most severe icing events now take place at Skrugard - not unexpected, since Skrugard generally has higher waves than Shtokman. Accumulated ice thicknesses reach 70-130 mm for Skrugard and 50-100 mm for Shtokman during the worst periods of icing (figures 4.16 - 4.17).

Figure 4.18 shows the calculated icing rate using the algorithm described in Overland (1990), and it is clear that this algorithm will predict unrealistically high icing rates for Shtokman in particular. The predicted icing rates on Skrugard, although high, at least appear to be limited to 20-30 mm/h.

## 5.2 Icing on AMI

Since AMI is a much smaller vessel than Norne, the assumptions made in the wave spray model should have more validity in this case. Calculated icing rates (figure 4.23) reach up to 8 mm/h at the bridge and 15 mm/h at the mast, which is high compared to the estimated icing rates on Norne, Skrugard and Shtokman. Also notice that the scaling of the icing rates axes are different for the three cases in this figure. In general, one would expect the icing rates to be greater for smaller vessels, since they are closer to the sea surface and therefore experience more spray. Once again, the Overland algorithm will estimate very high icing rates, although not as extreme as for Shtokman (both surface and air temperatures are higher at the location of AMI than at Shtokman).

The predicted accumulated ice thicknesses are plotted in figure 4.24, and ice thickness observations (Eide, 1983) are plotted in the same graphs. Not very much information about the observations is given in the report - this is why the plot of the observed thickness appears very incomplete, since no more information than what was given in the report has been added to the plot. In any case, the ice thickness estimated on the bridge seems to be in the same ballpark as the reported thicknesses. While no information about where the icing thickness was measured is available, it is not unreasonable to expect it to be near the bridge, considering the crew would likely not move about on the deck of the ship during strong icing conditions. The estimated ice thickness on the mast is much higher than the reported thicknesses, although expecting 800 mm thick ice on a mast with diameter of about 0.4 m is rather unrealistic. The estimated ice thicknesses using the icing rates from the Overland algorithm will strongly overestimate the thicknesses.

## 5.3 Total icing on a vessel

The available geometric models are generally unsuitable for icing calculations. For Norne in particular, the geometry has a very fine resolution for objects such as railings and operational equipment, and a very rough resolution for even surfaces. This means the model will have very many polygons (and thus be calculation-intensive), but still have a rough resolution for

the areas where most of the icing will occur. A geometrical model more suitable for icing calculations would have a finer resolution for the large surfaces, and make simplifications for rails and equipment.

In figure 4.33, the result for the strongest icing case at the location of Shtokman is illustrated. The icing rate reaches a maximum of about 20 mm/h, which is fairly consistent with the estimated icing rate of about 15 mm/h at 2 meters up on the exposed column in figure 4.11. It may seem odd that there appears to be no icing on the horizontal deck in front of the bridge. This is actually an artefact of the shielding model. As mentioned in section 3.4.3, the nodes are projected along droplet trajectories onto the spray jet, and the height of the nodes in the shielding plane is given by the height of the intersection point with the spray jet, see equation (3.19). For this geometrical model of Norne, the deck in front of the bridge actually consists of polygons that are thin and long in the  $y$  direction, and where the nodes are very close to the bow on both sides. Therefore, the projections from all three nodes of these polygons will hit the spray jet at a low height, and the algorithm will erroneously position the entire polygon at low height in the spray plane. In this case, this causes the deck polygons on Norne to be completely shielded by the bulwark, even though the middle part of the polygons should remain unshielded. This may cause problems in other cases where single polygons extend far to both the port and starboard side of the vessel, and the shielding algorithm should be changed to accommodate this.

## 5.4 Wind spray

### 5.4.1 Accuracy of wind spray generation function

The droplet concentration functions at the surface described by equations (2.1) and (2.2), on which the wind spray is based, are reported to have large uncertainties. Jones and Andreas (2012) mention an uncertainty to a factor of three for the concentration function at low wind speeds, and the uncertainty for the function at high wind speeds (which is based on an eyeball match to experimental data) should be no less. In addition comes uncertainty associated with the decrease of the concentration function with height (equation (2.3)). With such large uncertainties, it will be impossible to make very accurate predictions of wind spray icing, since the actual results could be at least a factor three higher or lower than estimated. Also, the estimated wind spray flux will be very sensitive to wind speed. The concentration function of water droplets in the air near the surface for high wind speeds (equation (2.2)), increases with the wind speed to the fourth power. In addition, the increased friction velocity and significant wave height associated with higher wind speeds means the concentration function will decrease less rapidly as one moves further from the surface. Since the spray flux to a given object also increases proportionally to the wind speed, this means the wind spray flux will increase with the wind speed to at least the fifth power, i.e. a small difference in wind speed leads to a high difference in wind spray flux. This is especially problematic because wind speed measurements are somewhat ambiguous, and depend on the length of time the wind speed was averaged over. The two standard wind speed measurements appear to be 1-minute average and 10-minute average, but Jones and Andreas (2012) do not specifically state whether the 1-minute or 10-minute averages should be used in the model. According to

Kathleen F. Jones (personal communication), it would be premature to debate whether the 1-minute average or 10-minute average should be used, due to the spray generation function for high wind speeds being based on very few measurements. In the present model, both the hindcast data and the meteorological observations are 10-minute averages for wind speed.

### 5.4.2 Height dependency of spray concentration function

Another part of the concentration function that should be discussed, is the height dependency as described in equation (2.3), where

$$\frac{dC(r, z)}{dr} = \frac{dC(r, h)}{dr} \left(\frac{z}{h}\right)^{\frac{-v_g(r)}{ku^* f_s}}.$$

One might have expected a height dependency that was a function of the height above the generation height, i.e.

$$\frac{dC(r, z)}{dr} = f(z - h),$$

yet the spray profile becomes a function of the height in proportion to the generation height. This has some fairly significant consequences, mainly that the spray profile will be very sensitive to generation height (the upper limit of the source region for the spray droplet generation). The consequence of halving the generation height  $h$ , i.e. from 2 m to 1 m, is the same as doubling the height above sea level  $z$ , i.e. from 10 to 20 meters, or even from 20 to 40 meters. It seems in Jones and Andreas (2012) that the treatment of generation height is rather simplified, assuming a generation height of 1 m for low winds and  $0.5H_s$  for high winds. When the spray profile depends so strongly on generation height, it might be valuable to have a more sophisticated method of finding this height.

### 5.4.3 Motion and temperature assumptions for wind spray

When including wind spray in the icing model for a complete vessel, we make certain assumptions about the wind spray that require some justification. First, we assume the wind spray droplets will have an approximately horizontal trajectory. Since the droplets in the wind spray are small ( $r < 200\mu\text{m}$ ), the drag force from the wind will be much greater than the gravitational force, and so the average movement in vertical direction should generally be insignificant compared to horizontal movement. Second, we assume that the droplets are small enough to be cooled very quickly (since heat exchange depends on surface area, and total heat exchange needed to cool the droplet depends on volume). We assume the droplets will be cooled down to the air temperature, even when the air temperature is far below the freezing point (i.e. the water will be supercooled). This leads to the question of why the droplets do not freeze mid-air in the model. One possible justification for this would be a lack of nucleation sites in the droplets (although they should still contain the salt molecules and other impurities of sea water). Another possibility is that the assumption is not actually justified - that for very cold air temperatures, the wind spray droplets will indeed freeze mid-air, and that very cold temperatures may in fact reduce wind spray icing, since frozen droplets may not attach to the surface.

As mentioned, we assume the drag forces on the droplets are much stronger than the gravitational forces. This unfortunately clashes with the assumption we make about the movement of wind spray in the complete icing model. When calculating which polygons the wind spray will hit, and which polygons are shielded from wind spray, the wind spray is treated like the larger droplets from the wave spray - we make the assumption that the inertia of the droplets is much greater than the drag force from the wind. In other words, when the wind collides with an object (and will therefore travel along the object), we assume all the wind spray collides with the object and none of it travels with the wind around or along the object. Also, we neglect turbulence in the air, which would make the wind spray hit polygons that, in the model, it currently does not. For instance, wind spray in the model can never hit horizontal polygons. This is an inconsistency in the model, where we treat the wind spray as being simultaneously small droplets (where wind drag is much greater than gravity) and large droplets (where inertia is much greater than wind drag). The model would be improved by consistently treating the wind spray as small droplets, and therefore account for turbulence and the droplets following the wind around objects in the model. Unfortunately, there was not time to implement such elements in the model.

## 5.5 Wave spray

The description of wave spray from Lozowski et al. (2000) makes numerous assumptions about the spray, and the spray jet in particular, that should be commented on. Especially the assumption that the spray jet starts at deck level or bow level (see equation (2.35)) has the rather peculiar consequence that the height of the deck has no effect on the amount of wave spray a ship is exposed to. This is counter-intuitive, as one would think vessels where the deck is far above the sea surface would be less affected by wave spray. Equation (2.35) originally comes from Zakrzewski (1987), which deals with wave spray on a medium-sized fishing vessel. The assumption may be reasonable for a medium sized vessel, where the waves may hit the vessel fairly close to the deck height, but it is not likely to be reasonable for a large FPSO. This means one should be very cautious about drawing firm conclusions from the results of the complete icing model for large vessels. For the wave spray to be properly included in calculations of icing for large vessels, the underlying assumptions of the spray jet should be changed to accommodate this.

## 5.6 Icing calculations

In addition to describing the spray flux and temperature of wave collision spray, Lozowski et al. (2000) also describe calculations for the icing rate. The decision to use the method of calculating icing rate as described by Horjen (1990) warrants some justification. The main difference between the two methods of calculating icing rate, is that Lozowski et al. (2000) assumes that the total brine content and the total salt content on each grid cell/polygon will not change for each time step - in other words, all the incoming brine and salt will either freeze, be entrapped in the ice, or flow to another polygon within the next time step. The treatment of heat flux is similar - the total heat flux from a polygon will all be spent

on freezing the surface brine. Unlike Lozowski et al. (2000), Horjen (1990) uses differential equations to describe surface brine, surface salt content and heat flux - in other words, it takes into account the fact that a polygon may accumulate brine, salt and heat, and that the icing and runoff brine will depend on these accumulated values. This is a seemingly more realistic approach to describing the behaviour of surface brine and icing.

Perhaps the most important reason to use the Horjen (1990) formulation is that the treatment of runoff brine in Lozowski et al. (2000) is unrealistic. In that article, it is assumed that all the surface brine on one grid cell will flow down to the grid cell below, within a time step of one second. This means that the speed at which the surface brine will run down a component of the ship is strongly dependent on polygon size (or the length of the  $\Delta z$  steps, if the polygon model is not used). Hence, the icing rate will be strongly dependent on how the vessel is partitioned into polygons, since a slower runoff speed for the surface brine means that the brine has more time to cool down, and the icing rate will increase. The calculations from Horjen (1990) include an expression for surface brine mean velocity (dependent on the brine amount on the polygon), and so the results will be largely unaffected by the polygon partitioning of the vessel.

## 5.7 Meteorological observations and hindcast data

As described in section 2.2, both recordings of meteorological data (from the FPSO Norne in the Norwegian Sea and from the weather ship AMI in the Barents Sea) and reanalysis data (on the locations of the Skrugard/Havis and Shtokman fields) have been used in the model. Since the icing rates are generally very sensitive to parameters like wind speed or air temperature, any systematic differences between hindcast and observed values may strongly influence the icing rates. This is especially true for wind generated spray, which has a very strong dependency on wind speed, as described in section 5.4. Any consistent difference in the frequency of cases with very high wind speeds and sub-zero temperatures between the estimated and measured weather data will therefore give significant differences in the frequency and severity of cases with strong icing.

The calculated icing rates when using observed data and hindcast data is shown in figures 4.25 and 4.26 for Norne and AMI respectively. In addition, histograms over the frequency of high wind speeds and low temperatures are provided in figures 4.27 - 4.30. One may immediately notice that the icing rates are generally lower when using the hindcast data, yet for Norne the hindcast data also gives far fewer icing cases, an effect that does not appear to be the case to the same extent for AMI. The reason for this is strongly suggested in the histograms - for Norne, sub-freezing temperatures appear much more seldom when using the hindcast data, and thus reducing the number of icing cases, while for AMI the frequency of low temperatures seems very close for observed and hindcast data. For the wind speed, the situation is opposite - here, hindcast data gives far fewer occurrences of high wind speeds for AMI, while actually giving somewhat more occurrences for Norne. It should not be unexpected to see consistent differences between observed and hindcast data, simply because the height at which the wind speed and temperatures are measured are not the same as the heights the hindcast variables are estimated for. This is especially true for Norne, where measurements are performed at a height of 33 m, whereas Nora10

estimates the wind speed at 10 m above the surface and the air temperature at 2 m above the surface. Considering this, it is not surprising that temperature observations on Norne are consistently below the hindcast temperatures - it is more surprising, however, that the hindcast wind speeds seem slightly higher than the observed wind speeds, when one would expect them to be lower. For the smaller vessel AMI, the measurements are made closer to the surface (although the exact height where the measurements are made is unknown). Thus, it is not surprising to see more correspondence in observed and hindcast temperatures for AMI. The fact that observed wind speeds are consistently higher than hindcast wind speeds is more peculiar.

Also, it might seem odd that the icing rates for AMI when using hindcast data seem fairly close to the icing rates when using meteorological observations, considering the observations have a much higher rate of high wind speeds. It is possible that, for the small AMI vessel, the spray fluxes are large enough so that the icing rate is mainly limited by the amount of heat transported away from the surface. Since the heat flux is much less sensitive to wind speed than the spray flux, this may be the cause of the apparent low sensitivity to wind speed.

## 5.8 Complete model

### 5.8.1 Inclined and horizontal geometries

Equation (3.25) in section 3.4.5 warrants some justification. The equation assumes that, when transforming the expression for brine velocity for vertical components to be used for inclined components, the acceleration due to gravity may simply be replaced by its component along the polygon surface. This is a strong simplification, especially since the flow of the fluid is also affected by the component of gravity normal to the surface, which increases as  $\theta$  decreases. It is therefore likely that a better expression for the brine velocity on inclined components could be derived, but this is beyond the scope of this text. At the very least, equation (3.25) will decrease towards 0 when  $\theta \rightarrow 0$ , which is expected behaviour.

The lower limit enforced for brine velocity for horizontal or nearly horizontal components in equation (3.26) also warrants explanation, especially since Horjen (1990) provides expressions for brine movement on horizontal plates, based on the force from incoming spray and wind acting on the plate. The reason why these expressions are ignored is two-fold: First of all, if the model should deal with horizontal runoff as well as vertical, this means the algorithm explained in section 3.4.4 would be necessary to run for each new weather case, since it would be dependent on wind direction. If the force from incoming spray and wind also should be applied to inclined polygons, the runoff model would also become vastly more complicated. Second, there is no such thing as a purely horizontal geometry on a vessel, at least not in rough weather conditions where icing is most of a concern. There will always be some movement and some roll/pitch on the vessel, meaning there will always be gravitational runoff even from polygons that would be horizontal in perfectly calm waters. For these reasons, the model will only concern itself with gravitationally driven runoff, and enforce a lower limit on brine velocity even on horizontal polygons. The lower limit of 0.2 for  $\sin \theta$ , which gives a  $\theta \approx 11.5^\circ$ , may be somewhat high, especially for large vessels.

It should also be commented that the ‘excess’ runoff on horizontal or nearly horizontal polygons, i.e. the brine that runs off the polygon due to the enforced lower limit, is not received by any other polygons, and will therefore simply disappear from the system. This is mostly because it would be very difficult to implement this excess runoff in the model (one would either have to include the vessel motions in the equations, or one would have to assume the runoff would spread to all surrounding polygons evenly), but can also be justified by pointing out that some brine will constantly run off the vessel. Making brine disappear off horizontal polygons may not be the best way to model this, but at least one avoids the somewhat unrealistic situation that all brine on the ship will either freeze or stay on the ship.

### **5.8.2 Application of the model on different platform shapes**

The generation of wave spray as described in Lozowski et al. (2000) only applies to ships. It is unknown how spray due to wave collisions can be modelled on other types of structures (e.g. a TLP, SPAR, semi-sub or buoy shaped floating platforms), or if it even contributes significantly to icing. It is possible that the areas of a platform that would be exposed to wave collision spray would have too much incoming spray for any icing to occur. Icing due to wind spray, however, can easily be applied to platforms using the present model - either by calculating the icing on a reference object on the platform, or even using the complete model (including shielding) to calculate wind spray icing on the entire platform, although this would be subject to the weaknesses of wind spray shielding as described in section 5.4.



# Chapter 6

## Conclusion and further work

A computer model for calculating icing on marine vessels and structures has been implemented and tested. The model is based on the description of wind generated sea spray from Jones and Andreas (2012), and the description of sea spray generated by wave-vessel collisions from Lozowski et al. (2000). The icing rates are calculated using equations described in Horjen (1990). The model may calculate icing rates on individual objects or points on the vessel/structure, or it may calculate icing rates on the entire vessel by using a polygon-based geometrical model. For these calculations, methods of including brine runoff as well as spray shielding have been developed and implemented.

The model has been applied to hindcast data for the locations of the Norne, Skrugard and Shtokman fields. The results indicate that icing is both much more frequent and much more severe at Skrugard and Shtokman than at Norne. The icing rates at Skrugard are estimated to be slightly lower than at Shtokman. It is also found that the use of hindcast data may underestimate the icing rates.

In order to improve the model in the future, the description of wave collision spray should be changed in order to be relevant for larger production vessels. If the model should be applied to offshore platforms, a description for wave collision spray relevant for platforms must be formulated. In order to accomplish this, experimental measurements of spray flux will be important. Judging from figure 4.14, where the spray flux is predicted to be greatest at Norne, these measurements may just as well be performed in the Norwegian Sea. For the wind generated spray, effects like turbulence and the spray droplets following the wind around objects should be included in the model. There are also large uncertainties in the wind spray concentration functions, especially for high wind speeds. Hopefully, more experimental measurements for wind spray during high wind speeds will reduce these uncertainties in the future.



# Chapter 7

## Acknowledgements

I would like to thank Statoil for providing a workplace during this time, as well as the data and resources necessary to make this thesis possible. I would especially like to thank my supervisor at Statoil, Sigurd Henrik Teigen, for his help and guidance throughout the entire work on this thesis. I would also like to thank Kenneth Johannessen Eik at Statoil for providing the relevant Nora10 hindcast data. Finally, I would like to thank Kathleen F. Jones at the Cold Regions Research and Engineering Laboratory for being very helpful in answering questions regarding her paper, and PhD student Anton Kulyakhtin at NTNU for providing a warm welcome in an otherwise cold environment at Svalbard and showing me the process of making actual experimental measurements of icing.



# Bibliography

- Andreas, E.L., 1990. Time constants for the evolution of sea spray droplets. *Tellus B*, 42(5): 481–497.
- Andreas, E.L. and Wang, S., 2007. Predicting significant wave height off the northeast coast of the United States. *Ocean Engineering*, 34(8-9):1328 – 1335.
- Andreas, E.L., Persson, P.O.G., and Hare, J.E., 2008. A bulk turbulent air-sea flux algorithm for high-wind, spray conditions. *J. Phys. Oceanogr.*, 38(7):1581–1596.
- Assur, A., 1958. *Composition of sea ice and its tensile strength*. U.S. National Academy of Sciences - National Research Council.
- Beljaars, A.C.M. and Holtslag, A.A.M., 1991. Flux parameterization over land surfaces for atmospheric models. *J. Appl. Meteor.*, 30(3):327–341.
- Blackmore, R., Zakrzewski, W., and Lozowski, E., 1989. Growth of ice on a ship's mast. In *Proc. 10th Int. POAC Conf.*, Lulea, Sweden.
- Buck, A.L., 1981. New equations for computing vapor pressure and enhancement factor. *J. Appl. Meteor.*, 20(12):1527–1532.
- COARE, 2012. Coupled Ocean-Atmosphere Response Experiment - Met Flux Algorithm. [Online; accessed February 2012], [http://coaps.fsu.edu/COARE/flux\\_algor/](http://coaps.fsu.edu/COARE/flux_algor/).
- Eide, L.I., 1983. Environmental conditions in the Barents Sea and near Jan Mayen. Technical report, The Norwegian Meteorological Institute.
- eKlima, 2012. Climate database for all present and past weather stations of the Norwegian Meteorological Institute. [Online; accessed June 2012], <http://www.eklima.met.no/>.
- Engineering Toolbox, 2012. [Online; accessed June 2012], <http://www.engineeringtoolbox.com/>.
- Fairall, C.W., Bradley, E.F., Rogers, D.P., Edson, J.B., and Young, G.S., 1996. Bulk parameterization of air-sea fluxes for tropical ocean-global atmosphere coupled-ocean atmosphere response experiment. *J. Geophys. Res.*, 101(C2):3747–3764.
- Fairall, C.W., Banner, M.L., Peirson, W.L., Asher, W., and Morison, R.P., 2009. Investigation of the physical scaling of sea spray spume droplet production. *J. Geophys. Res.*, 114: C10001.

- Finstad, K.J., Lozowski, E.P., and Gates, E.M., February 1988. A Computational Investigation of Water Droplet Trajectories. *Journal of Atmospheric and Oceanic Technology*, 5: 160–170.
- Gautier, D.L., Bird, K.J., Charpentier, R.R., Grantz, A., Houseknecht, D.W., Klett, T.R., Moore, T.E., Pitman, J.K., Schenk, C.J., Schuenemeyer, J.H., Sørensen, K., Tennyson, M.E., Valin, Z.C., and Wandrey, C.J., 2009. Assessment of undiscovered oil and gas in the Arctic. *Science*, 324(5931):1175–1179.
- Godfrey, J.S. and Beljaars, A.C.M., 1991. On the turbulent fluxes of buoyancy, heat and moisture at the air-sea interface at low wind speeds. *J. Geophys. Res.*, 96(C12):22043–22048.
- Högström, U., 1996. Review of some basic characteristics of the atmospheric surface layer. *Boundary-Layer Meteorology*, 78:215–246.
- Holtslag, A.A.M. and de Bruin, H.A.R., 1988. Applied Modeling of the Nighttime Surface Energy Balance over Land. *J. Appl. Meteor.*, 27:689–704.
- Hölz, S., 2006. Polygon Clipper. [Online; accessed June 2012], <http://www.mathworks.com/matlabcentral/fileexchange/8818-polygon-clipper/>.
- Horjen, I., 1990. Numerical modelling of time-dependent marine icing, anti-icing and de-icing. *Doctoral thesis, Norges Tekniske Høgskole (NTH), Trondheim, Norway*.
- Horjen, I. and Vefsnmo, S., 1987. Time-dependent sea spray icing on ships and drilling rigs - a theoretical analysis. Technical Report MSU-CSE-00-2, Norwegian Hydrotechnical Laboratory.
- Jones, K.F. and Andreas, E.L., 2009. Sea Spray Icing of Drilling and Production Platforms. Technical report, Cold Regions Research and Engineering Laboratory.
- Jones, K.F. and Andreas, E.L., 2012. Sea spray concentrations and the icing of fixed offshore structures. *Quarterly Journal of the Royal Meteorological Society*, 138(662):131–144.
- Langmuir, I. and Blodgett, K., 1946. A mathematical investigation of water droplet trajectories. *Collected works of Irving Langmuir*, 10:348 – 393.
- Lewis, E.R. and Schwartz, S.E., 2004. *Sea salt aerosol production: Mechanisms, methods, measurements and models: A critical review*. American Geophysical Union.
- Liu, W.T., Katsaros, K.B., and Businger, J.A., September 1979. Bulk parameterization of air-sea exchanges of heat and water vapor including the molecular constraints at the interface. *J. Atmos. Sci.*, 36(9):1722–1735.
- Locarnini, R.A., Mishonov, A.V., Antonov, J.I., Boyer, T.P., Garcia, H.E., Baranova, O.K., Zweng, M.M., and Johnson, D.R., 2010. *World Ocean Atlas 2009, Volume 1: Temperature*. S. Levitus, Ed., NOAA Atlas NESDIS 68, U.S. Government Printing Office, Washington, D.C.

- Lozowski, E.P., Szilder, K., and Makkonen, L., 2000. Computer simulation of marine ice accretion. *Royal Society of London Philosophical Transactions Series A*, 358.
- Nauman, J., 1984. Superstructure icing on the semi-submersible *Ocean Bounty* in Lower Cook Inlet, Alaska. In *Proc. 2nd. Int. Workshop on Atmospheric Icing of Structures*, Trondheim, Norway.
- Overland, J.E., 1990. Prediction of vessel icing for near-freezing sea temperatures. *Wea. Forecasting*, 5:62–77.
- Paulson, C.A., 1970. The mathematical representation of wind speed and temperature profiles in the unstable atmospheric surface layer. *J. Appl. Meteor.*, 9(6):857–861.
- Reistad, M., Breivik, Ø., Haakenstad, H., Aarnes, O.J., Furevik, B.R., and Bidlot, J.R., 2010. A high-resolution hindcast of wind and waves for the North Sea, the Norwegian Sea, and the Barents Sea. *J. Geophys. Res.*, 116, C05019.
- Ryerson, C.C., 2011. Ice protection of offshore platforms. *Cold Regions Science and Technology*, 65(1):97 – 110.
- Zakrzewski, W., 1987. Splashing a ship with collision-generated spray. *Cold Regions Science and Technology*, 14(1):65 – 83.